THE EFFECT OF COPPER ON THE DEFECT STRUCTURE OF CADMIUM

TELLURIDE THIN-FILM SOLAR CELLS

by

CHARLES WILLIAM WARREN

A DISSERTATION

Presented to the Department of Physics
and the Graduate School of the University of Oregon
in partial fulfillment of the requirements
for the degree of
Doctor of Philosophy

December 2015

DISSERTATION APPROVAL PAGE

Student: Charles William Warren

Title: The Effect of Copper on the Defect Structure of Cadmium Telluride Thin-Film Solar Cells

This dissertation has been accepted and approved in partial fulfillment of the requirements for the Doctor of Philosophy degree in the Department of Physics by:

Benjamín J. Alemán	Chair
Mark C. Lonergan	Advisor
Benjamin J. McMorran	Core Member
Hailin Wang	Core Member
Shannon W. Boettcher	Institutional Representative

and

Scott L. Pratt	Dean of the Graduate School

Original approval signatures are on file with the University of Oregon Graduate School.

Degree awarded December 2015

DISSERTATION ABSTRACT

Charles William Warren

Doctor of Philosophy

Department of Physics

December 2015

Title: The Effect of Copper on the Defect Structure of Cadmium Telluride Thin-Film Solar Cells

Transient photocapacitance (TPC) and transient photocurrent (TPI) spectroscopy have been used to examine the defect structure in the upper-half of the bandgap of CdTe solar cells, with an emphasis on understanding the effect of copper. TPC spectra reveal two defects in the CdTe devices at optical energies of $E_V + 1.2\,\text{eV}$ and $E_V + 0.9\,\text{eV}$. The origin of the $1.2\,\text{eV}$ defect could not be associated with a particular element, although copper and zinc were ruled out as sources. TPI spectra were used to observe that the density of the $1.2\,\text{eV}$ defect was dramatically reduced by thermally annealing the devices, suggesting that the defect itself is annealed during the treatment.

The set of CdTe samples examined used a rapid thermal processing treatment to control the amount of copper that diffused into the CdTe layer from the Cu:ZnTe interfacial layer at the back of the device. Comparison of devices with varying amounts of copper in the CdTe layer revealed that the $0.9\,\text{eV}$ defect seen in TPC was associated with the presence of copper in the absorber layer. TPI spectra confirmed the association of the $0.9\,\text{eV}$ with copper and showed that the magnitude of the

0.9 eV defect signal increased as more copper was diffused into the CdTe layer. A proportional link between the density of the 0.9 eV defect observed in TPI spectra and the amount of copper in the absorber layer observed via ToF-SIMS further established that copper is responsible for the existence of the defect. Numerical modeling of the CdTe devices was used to confirm that the spatial distribution of copper observed in ToF-SIMS was consistent with the relative variation of defect magnitudes observed in TPI.

The fact that the copper-associated 0.9 eV defect lies close to mid-gap suggests that it will act as an efficient recombination center in CdTe. Therefore, it is suggested that this work has detected the deep defect that is responsible for the decreased minority carrier lifetime that has been previously associated with the amount of copper in the CdTe layer.

CURRICULUM VITAE

NAME OF AUTHOR: Charles William Warren

GRADUATE AND UNDERGRADUATE SCHOOLS ATTENDED:
    University of Oregon, Eugene, OR
    University of Pittsburgh, Pittsburgh, PA

DEGREES AWARDED:
    Doctor of Philosophy, Physics, 2015, University of Oregon
    Bachelor of Science, Physics and Astronomy, 2009, University of Pittsburgh

AREAS OF SPECIAL INTEREST:
    Solid State Physics
    Semiconductor Device Physics
    Photovoltaics

PROFESSIONAL EXPERIENCE:

    Research and Teaching Assistant, Department of Physics, University of Oregon, Eugene, OR, 2009-2015

    Research Assistant, Department of Physics and Astronomy, University of Pittsburgh, Pittsburgh, PA, 2006-2009

GRANTS, AWARDS AND HONORS:

    Bachelor of Science *Summa Cum Laude*, University of Pittsburgh, 2009

    Halliday Award for Excellence in Undergraduate Research, University of Pittsburgh, 2007

    Sigma Pi Sigma Physics Honorary Society, University of Pittsburgh, 2007

PUBLICATIONS:

    C. W. Warren, J. Li, C. A. Wolden, D. Meysing, T. M. Barnes, D. W. Miller, J. T. Heath, and M. C. Lonergan, "The effect of copper on the sub-bandgap density of states of CdTe solar cells," *Applied Physics Letters*, vol. 106, pp. 203903, 2015.

J. Li, D. R. Diercks, T. R. Ohno, C. W. Warren, M. C. Lonergan, J. D. Beach, and C. A. Wolden, "Controlled activation of ZnTe:Cu contacted CdTe solar cells using rapid thermal processing," *Solar Energy Materials and Solar Cells*, vol. 133, pp. 208-215, 2015.

J. W. Boucher, D. W. Miller, C. W. Warren, J. D. Cohen, B. E. McCandless, J. T. Heath, M. C. Lonergan, and S. W. Boettcher, "Optical response of deep defects as revealed by transient photocapacitance and photocurrent spectroscopy in CdTe/CdS solar cells," *Solar Energy Materials and Solar Cells*, vol. 129, pp. 57-63, 2014.

C. W. Warren, D. W. Miller, F. Yasin, and J. T. Heath, "Characterization of bulk defect response in $Cu(In, Ga)Se_2$ thin-film solar cell using DLTS," in *Proceedings of the 39th IEEE Photovoltaic Specialists Conference*, pp. 0170-0173, 2013.

D. W. Miller, C. W. Warren, O. Gunawan, T. Gokmen, D. B. Mitzi, and J. D. Cohen, "Electronically active defects in the $Cu_2ZnSn(Se, S)_4$ alloys as revealed by transient photocapacitance spectroscopy," *Applied Physics Letters*, vol. 101, no. 14, p. 142106, 2012.

O. Gunawan, T. Gokmen, C. W. Warren, J. D. Cohen, T. K. Todorov, D. A. R. Barkhouse, S. Bag, J. Tang, B. Shin, and D. B. Mitzi, "Electronic properties of the $Cu_2ZnSn(Se, S)_4$ absorber layer in solar cells as revealed by admittance spectroscopy and related methods," *Applied Physics Letters*, vol. 100, no. 25, p. 253905, 2012.

ACKNOWLEDGEMENTS

Dedicated to my family.

In memory of Dr. Cohen.

TABLE OF CONTENTS

LIST OF FIGURES

Figure | Page

LIST OF TABLES

CHAPTER I

INTRODUCTION

A material exhibits the photovoltaic effect if exposure to light creates a voltage (or current) within it. Thus, photovoltaic devices, or solar cells, use light to generate a voltage (or drive a current, equivalently). The photovoltaic effect itself has a long history, with the first observation of the effect in a solid state device by W. Adams and R. Day dating back to 1876 [1]. However, it was not until 1954, when Chapin, Fuller and Pearson introduced the first silicon solar cell [2], that a significant advance was made toward utilizing the photovoltaic effect as a practical source of energy. At present, the ultimate goal of the field of photovoltaics is to realize what Chapin, Fuller and Pearson initiated—using solar cells as a practical source of energy. To this end, much research has been devoted to understanding device and materials physics as they relate to solar cells, and it is the goal of this work to make a contribution to this effort.

At this point it is best to take a step back and understand some of the basic properties of solar cells. In the absence of light, an ideal solar cell is simply a diode. Thus, it obeys the ideal diode equation (derived in Appendix E)

$$J_{\mathrm{dark}}(V) = J_s \left(\exp\left[\frac{qV}{k_B T} \right] - 1 \right), \tag{1.1}$$

where $J_{\mathrm{dark}}(V)$ is the current density as a function of applied voltage (V) in the dark, J_s is the saturation current, q is the fundamental charge, k_B is Boltzmann's constant, and T is the absolute temperature. When the solar cell is exposed to light, absorbed photons create electron-hole pairs in the device. The electrochemical

potential difference across the device separates the electrons from the holes, and drives them out of the device into the external circuit. The photogenerated electrons and holes leaving the device result in a photocurrent (J_{SC}) that flows in the opposite direction of the dark current (when $V > 0$, i.e., in forward bias). Therefore, an ideal solar cell under illumination will behave such that

$$J_{\text{light}}(V) = J_{\text{dark}}(V) - J_{SC} = J_s \left(\exp\left[\frac{qV}{k_B T} \right] - 1 \right) - J_{SC}. \tag{1.2}$$

Eqs. 1.1 and 1.2 are plotted in Figure 1. Under illumination, there are several quantities that are convenient to define. They are: the short-circuit current (J_{SC}), which is the current when $V = 0$; the open-circuit voltage (V_{OC}), which is the voltage when $J = 0$; and the maximum power point (J_m, V_m), which is the point at which the power $P = JV$ is maximized. From these quantities, one can define the fill factor

$$FF \equiv \frac{J_m V_m}{J_{SC} V_{OC}}, \tag{1.3}$$

and the power conversion efficiency

$$\eta \equiv \frac{P_{\text{out}}}{P_{\text{in}}} = \frac{J_m V_m}{P_{\text{in}}} = \frac{J_{SC} V_{OC} FF}{P_{\text{in}}}, \tag{1.4}$$

where P_{out} is the power generated by the solar cell, and P_{in} is the power put into the solar cell (via illumination). Typically, P_{in} is $1000\,\text{W/m}^2$ with the Air Mass 1.5 (AM1.5) spectrum.[1] More than any other parameter, the power conversion efficiency (often referred to as the 'PCE' or just the 'efficiency') determines whether or not a

---

[1]AM1.5 is the solar spectrum after it has passed through 1.5 atmospheric thicknesses.
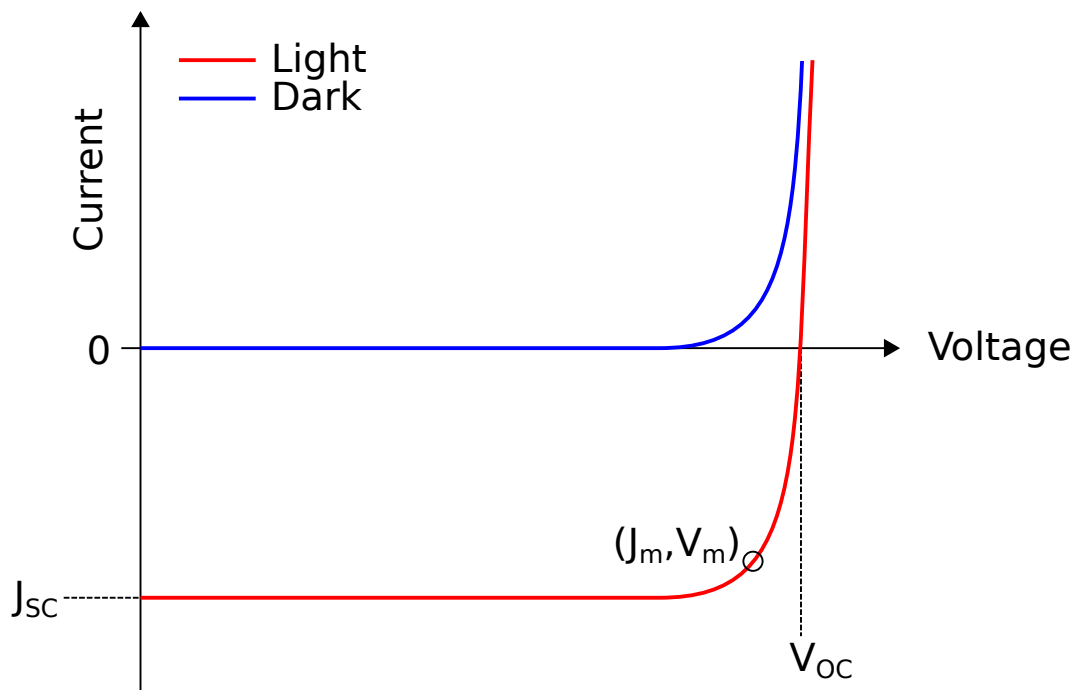
FIGURE 1. The current-voltage characteristics of an ideal solar cell in the dark (blue) and under illumination (red). Also shown is the short-circuit current (J_{SC}, the current when $V = 0$), and the open-circuit voltage (V_{OC}, the voltage when $J = 0$), and the maximum power point ((J_m, V_m), the point at which the power $P = JV$ is maximized.

given solar cell will be useful a energy generation device, and the goal of studying and understanding photovoltaic devices is often to increase this number.

One basic type of solar cell design is shown in Figure 2. Because the glass layer is on the top of the device (the side light enters), is it said to be in the 'superstrate' configuration.[2] To be absorbed in the absorber layer, light first passes through the glass, the transparent conductor, and the window layer. The absorbed light generates electron-hole pairs in the absorber layer, which are then separated by the electrochemical potential difference between the window layer and the absorber layer. Majority carriers[3] are driven to the back of the device, where they are collected by the back contact (which has a much higher conductivity than the absorber layer, often simply a metal) and transported to the external circuit. Minority carriers are driven to the front of the device, where they enter the window layer. Often, the window layer that interfaces favorably with the absorber layer is not a good conductor. In these cases, a high conductivity transparent conductor layer is needed to transport the minority carrier laterally to the external circuit.[4]

At present, the dominant material used in solar cells for power generation is multi-crystalline silicon, accounting for more than half of the yearly global production [3]. However, one drawback of silicon is that it has an indirect bandgap. A bandgap is said to be 'indirect' if the excitation of a charge carrier across it requires a change in momentum. Since photons near the bandgap energy of semiconductors carry essentially zero momentum, the absorption of a *phonon* must be involved

---

[2]If the glass were on the bottom it would be in the 'substrate' configuration.

[3]Charge carriers that are in excess in the absorber material.

[4]Carriers need to travel roughly $100\,\mathrm{nm}$ vertically to escape the window layer, while reaching the external circuit often requires they travel many millimeters or centimeters. Thus, a low conductivity window layer can be tolerated if it is sufficiently thin, while the conductivity requirements of the transparent conductor are much more stringent.
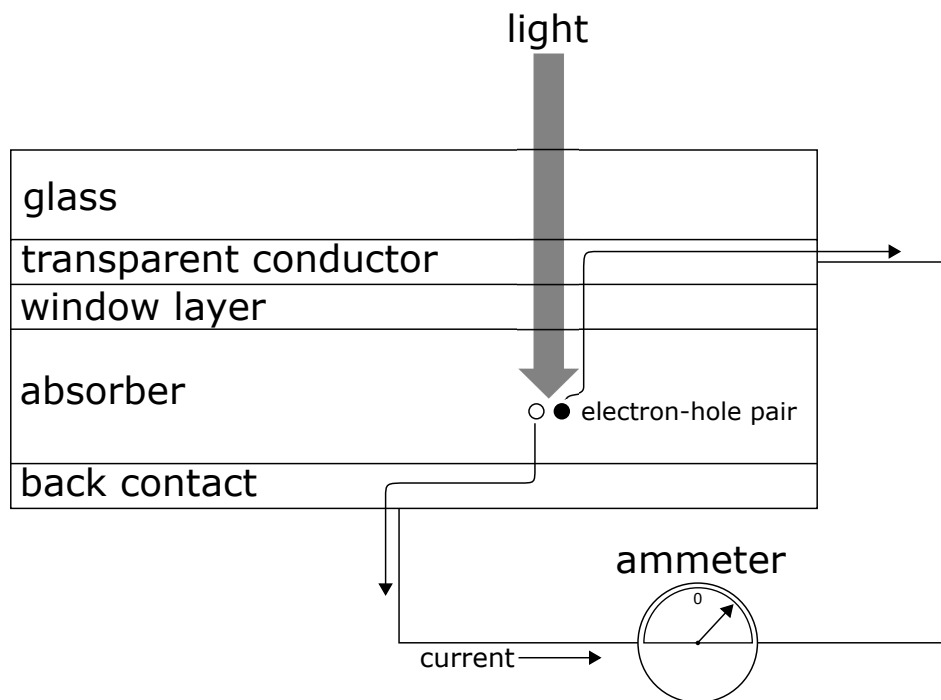
FIGURE 2. Basic solar cell design illustrating how charge carriers are generated in the absorber layer and collected into the external circuit.

whenever a *photon* is absorbed by an indirect bandgap material.[5] For a direct bandgap material, the absorption of a photon conserves momentum, which means no phonon interactions are required for it to take place. As a result, direct bandgap materials tend to have much larger absorption coefficients than indirect bandgap materials. For silicon, the absorption coefficient is $10^4\,\mathrm{cm}^{-1}$ at $500\,\mathrm{nm}$. As a consequence, the absorber layer in silicon solar cells needs to be roughly $100-200\,\mu\mathrm{m}$ thick for a high percentage of incident photons to be absorbed. So called 'thin-film' solar cell

---

[5]Recall that the momentum carried by a photon is the energy divided by the speed of light. Silicon has a bandgap of $1.12\,\mathrm{eV}$ at $300\,\mathrm{K}$, therefore a photon at the bandgap energy carries a momentum $p = (1.12\,\mathrm{eV})(1.602 \times 10^{-19}\,\mathrm{J/eV})/(2.998 \times 10^8\,\mathrm{m/s}) = 6 \times 10^{-28}\,\mathrm{kg\,m/s}$. An electron at the conduction band minimum of silicon will have a wave vector k on the order of π/a, where a is the lattice constant ($5.43 \times 10^{-10}\,\mathrm{m}$ for silicon). Thus, the momentum of an electron at the conduction band minimum will be $p = \hbar k \approx (1.055 \times 10^{-34}\,\mathrm{J\,s})(\pi/5.43 \times 10^{-10}\,\mathrm{m}) = 6 \times 10^{-25}\,\mathrm{kg\,m/s}$—about 3 orders of magnitude larger than the momentum supplied by the photon. So, about 99.9% of the momentum required for an indirect gap transition in silicon needs to comes from an interation with a phonon.

technologies utilize direct bandgap materials, whose high absorption coefficient allow for the absorber layer to be much thinner (typically $1-10\,\mu$m). Having a thinner absorber layer is advantageous because it reduces the materials cost, and the weight.[6] One such direct bandgap material is CdTe, which has an absorption coefficient greater than $10^5\,\text{cm}^{-1}$ at $500\,$nm—allowing for typical absorber thicknesses of only $2-4\,\mu$m [4].

Starting in the mid-1960s CdS/CdTe heterojunctions (the focus of this work, hereafter referred to as CdTe) were studied in the context of their application as thin-film diodes and photodetectors [5–7]. By the early 1970s, the work of Bonnet et al. [8], Fahrenbruch et al. [9], and Yamaguchi et al. [10] toward their application as solar cells for power generation had resulted in devices with single digit power conversion efficiencies. It was not until 1993 that advances in the CdTe fabrication techniques (most notably the post-deposition treatment of the CdTe film with $CdCl_2$) resulted in the first CdTe solar cell with an efficiency greater than 15% [11].

Over the following decades, the manufacturing of CdTe solar cells grew into a multibillion-dollar industry—as of October 2015, CdTe is the most manufactured thin-film solar cell technology in the world with nearly $2000\,$MW (at peak output) produced annually [3]. The current world record efficiency for CdTe (held by First Solar) is 21.5% for a single solar cell [12], which compares favorably to the world record efficiency of 20.4% [3] for a single multi-crystalline silicon solar cell. The current world record is 18.6% for a CdTe module [13] (also held by First Solar).

Despite the advancements that have been made in the understanding and production of CdTe solar cells, further efficiency improvements remain limited by recombination in the CdTe layer [14]. Since recombination in solar cells is mediated by defect states residing in the bandgap, understanding what defects are present in

---

[6]The weight is an important factor for solar panels that are installed on rooftops.

the sub-bandgap density of states of CdTe is important if improvements are to be made. In particular, an understanding of what elements are responsible defect states is needed to guide and inform future progress. With these broad goals in mind, this work is focused on the role of copper in the defect structure of CdTe solar cells.

In order to understand why copper is worth focusing on, one must understand the back contact of CdTe. One of the difficulties presented by CdTe is that making an ohmic back contact is challenging [4]. This is because forming an ohmic contact to CdTe requires a metal with a work function >5.7 eV [15]. Even platinum, which has the highest work function amongst the metallic elements (5.65 eV [16]), does not satisfy this requirement. One common method to get around this is is to create a tellurium-rich surface at the back contact, which is often achieved by a wet chemical etch of the back surface using a Br_2/methanol mixture [17]. The etch is followed by the deposition a copper-containing material on the tellurium-rich surface. Copper reacts with the tellurium to form a heavily p-doped region, which can then be contacted directly with a metal to form a tunnel junction or with an interfacial layer [4]. One common interfacial layer is copper-doped ZnTe (denoted Cu:ZnTe), which has favorable valance band alignment with CdTe, and can itself be heavily doped to form a tunnel junction with a metal (e.g. gold) [18, 19].

Nearly all the methods to form a back contact to CdTe have one factor in common—the use of copper. Indeed, despite research into copper-free contacting schemes (see, e.g., [20]), copper-containing back contacts are currently the most effective method for forming a reasonably ohmic, low-resistance contact [4]. Futhermore, as discussed in Chapter V, copper is a common impurity in tellurium feedstock [21] and therefore may *unintentionally* appear in CdTe devices regardless of
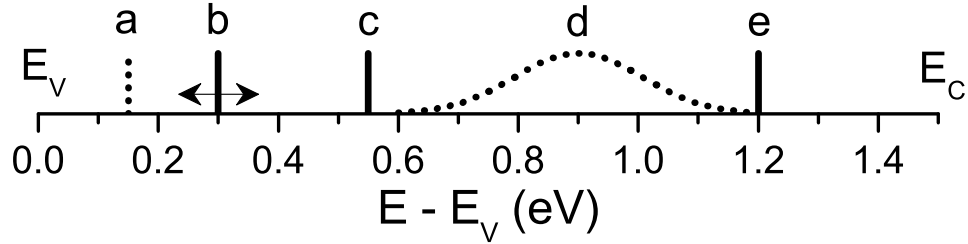
FIGURE 3. Illustration of the defect levels in CdTe that have been associated with copper. Thermal (solid) and optical (dotted) energies of traps associated with the presence of copper in CdTe. This includes: (a) an acceptor state at $E_V + 0.15\,\text{eV}$ seen in photoluminesence [27], (b) various states at roughly $E_V + 0.3\,\text{eV}$ detected with various techniques such as photo-induced current transient spectroscopy [27], (c) a deep state at $E_V + 0.55\,\text{eV}$ seen in admittance spectroscopy [28], (d) a deep state at $E_V + 0.9\,\text{eV}$ discussed in this work, and (e) a state at $E_C - 0.28\,\text{eV}$ seen in optical deep level transient spectroscopy [26]. Traps denoted with vertical lines had no determination of the energetic width. State "d" is drawn as a Gaussian, reflecting the results of this work.

the contacting scheme used. Thus, a detailed understanding of the role copper plays in CdTe solar cells is needed to understand how the devices work as a whole.

The role of copper in CdTe is not limited to forming an reasonably ohmic back contact, as it is has been associated with other beneficial and detrimental effects. For example, in addition to forming a back contact, CdTe absorbers benefit from copper because it is p-type dopant [4]. Unfortunately, copper is also associated with reduced minority carrier lifetime—suggesting that copper is also responsible for the introduction of recombination centers in CdTe [22–24]. Indeed, Cu has been associated with various defects levels in CdTe (summarized in Figure 3). This includes previous studies of CdTe that have associated copper with thermal transitions using methods such as deep level transient spectroscopy (DLTS) [25, 26], photo-induced current transient spectroscopy (PICTS) [27], and admittance spectroscopy (AS) [28]. Optical transitions have been observed with photoluminescence (PL)[27] as well as in this work. Owing to their thermal nature, the bulk of these measurements that

can detect deep states are sensitive to those lower than the mid-gap energy. This means that deep states, which are the most efficient recombination centers [29], in the upper-half of the gap are largely unexplored. In order to further improve the efficiencies of CdTe solar cells, and balance the beneficial and detrimental aspects of copper inclusion, the effect of copper on mid-gap states must be better understood. Such an understanding will lead to improved material and device models. Fortunately, transient photocapacitance (TPC) and transient photocurrent (TPI) spectroscopy are well suited for measuring optical transitions in the upper half of the bandgap, within absorber layers of working devices [30].

These techniques (presented in Chapter III) are used to detect two broad transitions in CdTe solar cells (the sample set is described in Chapter IV). As described in Chapter V, these defects are centered at $0.9\,\mathrm{eV}$ and $1.2\,\mathrm{eV}$ above the valence band. The $0.9\,\mathrm{eV}$ transition is shown to be associated with the presence of copper, and implicated as the recombination center responsible for the reduced carrier lifetime that has been associated with copper previously. The $1.2\,\mathrm{eV}$ transition is shown to not be associated with copper (or zinc), and may be an intrinsic defect. In Chapter II and the Appendices, the background necessary to the understand the results of this work is provided, including a detailed introduction into the physics of $p-n$ junctions, junction capacitance, and the numerical modeling of $p-n$ junctions.

CHAPTER II

BACKGROUND

The $p - n$ **Junction**

A $p - n$ junction (see Figure 4) is formed by joining a p-type and an n-type semiconductor. When the junction is formed, excess holes on the p-side of the junction will diffuse to the n-side, while excess electrons on the n-side will diffuse to the p-side. The diffusion of holes to the n-side of the juction leaves the p-side near the interface depleted of free carriers. This results in an overall negative charge in the region near the interface due the fixed, ionized acceptor sites that are left behind by the holes. Likewise, the diffusion of electrons to the p-side of the juction leaves the n-side near the interface depleted of free carriers. This results in an overall positive charge for this depletion region due the fixed, ionized donor sites that are left behind by the electrons. The charged regions on either side of the interface give rise to an electric field, $\mathcal{E}$, which acts against diffusion.

The electrons and holes at the $p - n$ interface will drift and diffuse until they reach thermal equilibrium. At equilibrium the net hole and electron currents are exactly zero, i.e.,

$$J_n^{\text{drift}} + J_n^{\text{diffusion}} = J_p^{\text{drift}} + J_p^{\text{diffusion}} = 0. \tag{2.1}$$

Here, J_n^{drift} is the electron current due to the electric field, $J_n^{\text{diffusion}}$ is the electron current due to diffusion, J_p^{drift} is the hole current due to the electric field, and $J_p^{\text{diffusion}}$ is the hole current due to diffusion. This equilibrium condition can be re-expressed in terms of the junction Fermi level. To see how, recall that the drift current for

10
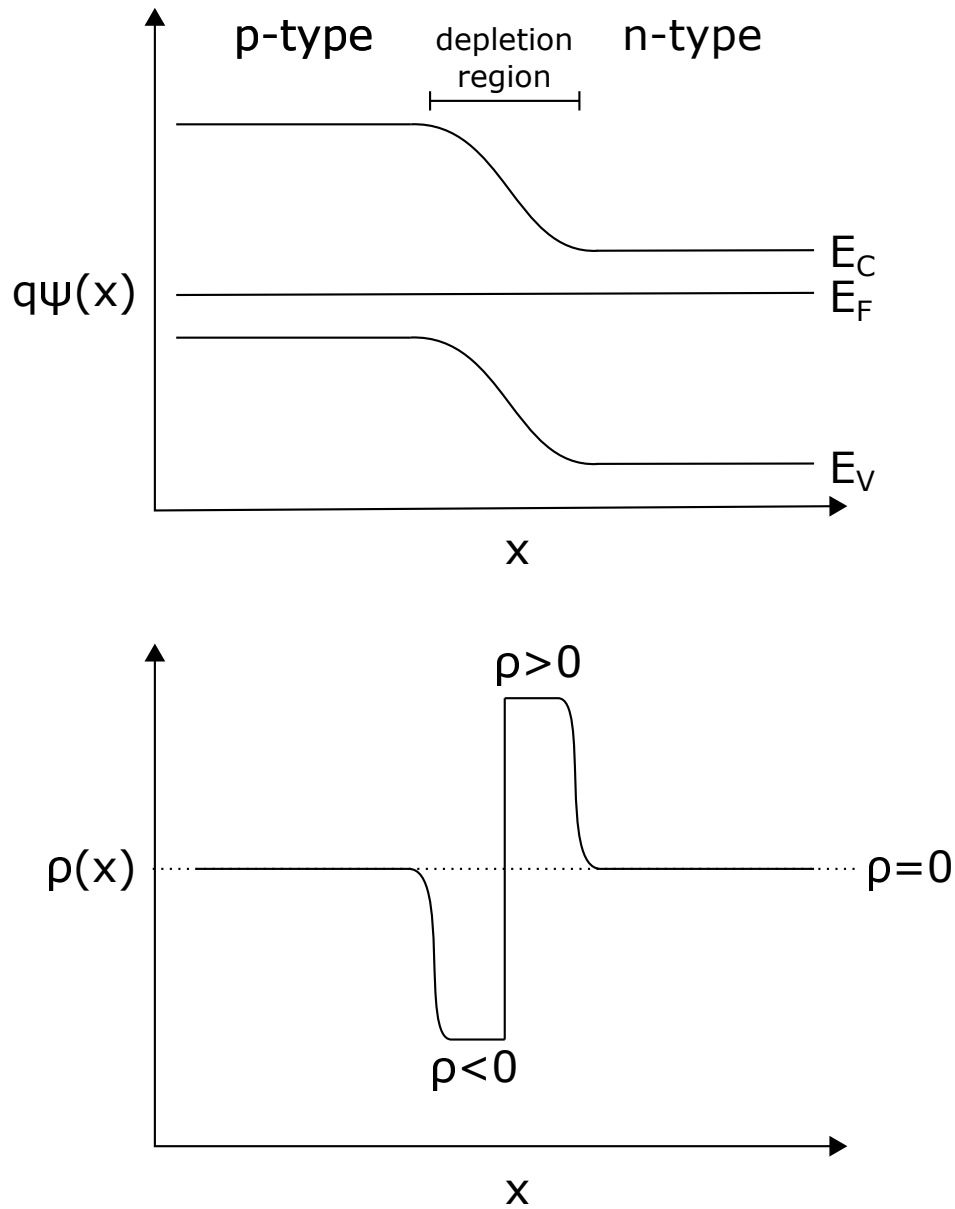
FIGURE 4. Band diagram and charge density profile of a $p-n$ junction. There are no free carriers in the depletion region (to a good approximation), and the overall charge is due to the fixed ionized donor or acceptor sites that the charges left behind. Outside the depletion region the total charge is zero because the density of free carriers exactly matches the density of ionized lattice sites.

electrons due to $\mathcal{E}$ (see Appendix A) is

$$J_n^{\text{drift}} = q\mu_n n \mathcal{E}, \tag{2.2}$$

where q is the magnitude of the charge of an electron, μ_n is the electron mobility, and n is the density of electrons in the conduction band (i.e., free electrons). As shown in Appendix B (Eq. B.5), the diffusion current for electrons due to an electron concentration gradient, dn/dx, is given by

$$J_n^{\text{diffusion}} = qD_n \frac{dn}{dx}, \tag{2.3}$$

where D_n is the diffusivity. Considering only electrons[1], substituting Eqs. 2.2 and 2.3 into the equilibrium condition (Eq. 2.1) gives

$$q\mu_n n \mathcal{E} + qD_n \frac{dn}{dx} = 0. \tag{2.4}$$

Using Eq. C.22 and the Einstein relation (Eq. B.11), this becomes

$$\mu_n n \frac{dE_C}{dx} + k_B T \mu_n \frac{dn}{dx} = 0. \tag{2.5}$$

From Eq. C.15

$$\frac{dn}{dx} = \frac{n}{k_B T} \left[-\frac{dE_C}{dx} + \frac{dE_F}{dx} \right], \tag{2.6}$$

which allows us to rewrite Eq. 2.5 as

$$\mu_n \frac{dE_C}{dx} + \mu_n \left[-\frac{dE_C}{dx} + \frac{dE_F}{dx} \right] = 0. \tag{2.7}$$

_____

[1]The derivation for holes is independent and identical.

From which it is apparent that

$$\frac{dE_F}{dx} = 0 \tag{2.8}$$

at equilibrium throughout the $p - n$ junction. Thus, the equilibrium condition for current (Eq. 2.1) requires that the Fermi level be flat throughout the junction (as shown in Figure 4).

A $p - n$ junction is 'one-sided' if one side of a $p - n$ junction is much more heavily doped than the other (denoted $p^+ - n$ or $p - n^+$, with the '+' indicated the heavily doped side). In this case (see Figure 6), charge neutrality requires that the depletion region resides almost entirely with the lightly doped side of the junction. For example, if the doping on the n^+-side is 1000 times greater than on the p-side, then the depletion region on the n^+-side will be 1000 times smaller than the depletion region on the p-side.

In one dimension[2], the potential profile (i.e., the band bending) and charge profile in a $p - n$ junction are determined by Poisson's equation

$$\frac{d^2\psi}{dx^2} = \frac{\rho(x)}{\epsilon}. \tag{2.9}$$

Here, ψ is the *electron* potential (which is why the right-hand side of Eq. 2.9 is positive), ρ is the charge density, and ϵ is the permittivity.[3] For a $p - n$ junction in thermal equilibrium the charge density is given by an integral over the density of states, $g(E, x)$,

$$\rho(x) = q \int \left[f(E', E_F^0, T) - f(E', E_F^0 - \psi(x), T) \right] g(E', x) dE', \tag{2.10}$$

---

[2]It is assumed the $p - n$ junction is uniform laterally.

[3]Throughout, ψ is defined such that $\psi = 0$ in the neutral region far away from the junction interface.

where

$$f(E, E_F, T) = \frac{1}{1 + e^{(E-E_F)/k_B T}} \tag{2.11}$$

is the Fermi-Dirac distribution, and E_F^0 is the Fermi level in the neutral bulk [31]. In Eq. 2.10, the expression inside the square brackets connects the charge density at position x to the amount of band bending, $\psi(x)$, at that location. That is, the net charge density in the depletion region originates from the portion of the density of states that has been pulled above the Fermi level due to the band bending (as illustrated in Figure 5). In the low-temperature limit, the Fermi-Dirac distribution becomes a step function, which allows one to simplify Eq. 2.10 to

$$\rho(x) = q \int_{E_F^0 - \psi(x)}^{E_F^0} g(E', x) dE'. \tag{2.12}$$

Using Poisson's equation and Eq. 2.12 to solve for ψ and ρ can be done numerically (see Appendix D), and can even be done analytically in special cases.

Junction Capacitance

The results of the previous sections can be extended to derive the capacitance associated with a $p-n$ junction, i.e., the junction capacitance. To see how, consider a one-sided $p-n^+$ junction (see Figure 6) with the junction interface at $x = 0$. Take

$$\psi(\infty) = 0, \tag{2.13}$$

for simplicity, and

$$\left.\frac{d\psi}{dx}\right|_\infty = 0 \tag{2.14}$$

14
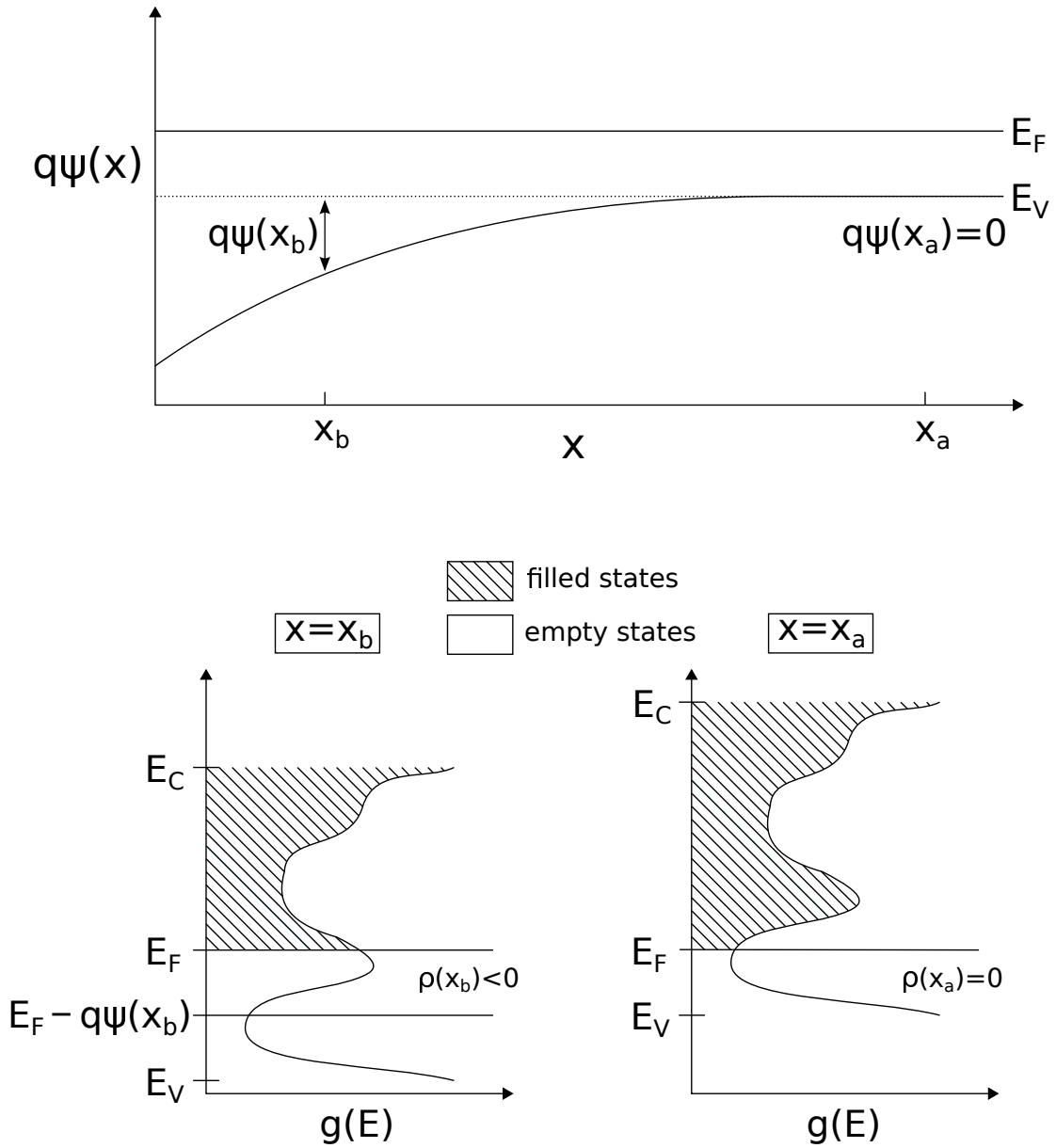
FIGURE 5. Illustration of how band bending in a $n^+ - p$ junction is related to the charge density via integration of the density of states, as in Eq. 2.12. Hatched regions of the density of states are filled with holes. At $x = x_a$, there is no band bending and the net charge density is zero. At $x = x_b$, the band bending is $\psi(x_b)$, and the net charge is proportional to the area of the density of states that has been pulled below the Fermi level (as in Eq. 2.12).

15
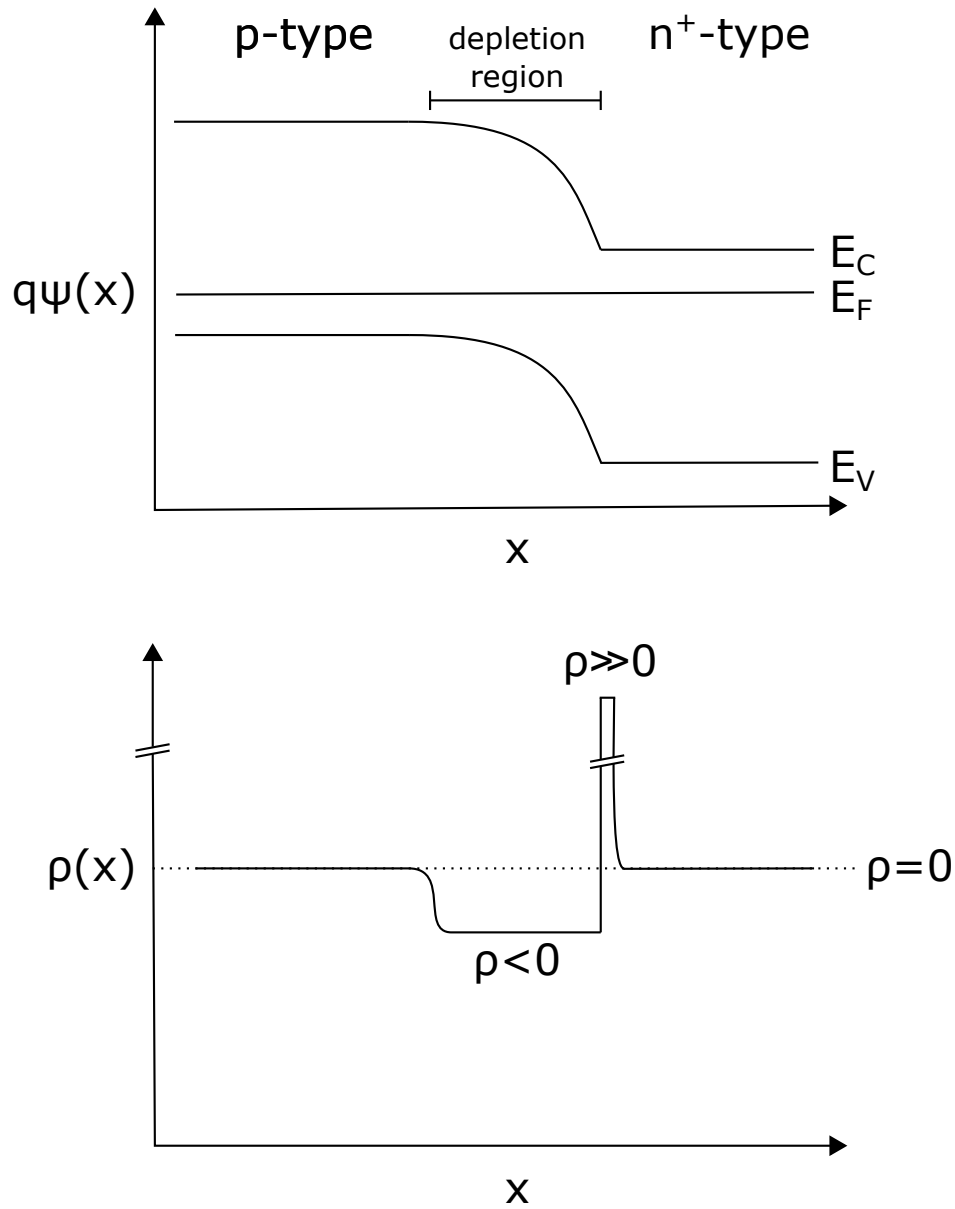
FIGURE 6. Band diagram and charge density profile of one-sided $p - n^+$ junction. Charge neutrality requires that the depletion region is almost entirely within the lightly doped p-side of the junction.

16

to enforce charge neutrality deep in the bulk. Using the chain rule, Poisson's equation for the *electron* potential

$$\frac{d^2\psi}{dx^2} = \frac{\rho(x)}{\epsilon} \qquad (2.15)$$

can be rewritten as

$$\frac{d}{dx}\left(x\frac{d\psi}{dx}\right) - \frac{d\psi}{dx} = \frac{x\rho(x)}{\epsilon}. \qquad (2.16)$$

Integrating Eq 2.16 gives

$$\left[x\frac{d\psi}{dx}\right]_0^\infty - [\psi(x)]_0^\infty = \int_0^\infty \frac{x\rho(x)}{\epsilon}dx. \qquad (2.17)$$

The boundary conditions (Eqs. 2.13 and 2.14) simplify the left-hand side of Eq. 2.17 yielding

$$\psi(0) = \int_0^\infty \frac{x\rho(x)}{\epsilon}dx. \qquad (2.18)$$

Thus, a change in the charge distribution $\delta\rho(x)$ is related to a change in the electron potential δV by

$$\delta V = \int_0^\infty \frac{x\delta\rho(x)}{\epsilon}dx, \qquad (2.19)$$

and the change in the total charge of a junction with area A will be

$$\delta Q = A\int_0^\infty \delta\rho(x)dx. \qquad (2.20)$$

Combining Eqs. 2.19 and 2.20 defines the junction capacitance[4]

$$C \equiv \frac{\delta Q}{\delta V} = \frac{\epsilon A\int_0^\infty \delta\rho(x)dx}{\int_0^\infty x\delta\rho(x)dx} \equiv \frac{\epsilon A}{\langle x \rangle} \qquad (2.21)$$

---

[4]Note that the electron potential ψ that appears in Poisson's equation has units of volts. The same is true for the applied voltage δV that appears in the definition of capacitance. Thus, the change in electron potential and the change in applied voltage are identical.

where

$$\langle x \rangle \equiv \frac{\int_0^\infty x \delta\rho(x)dx}{\int_0^\infty \delta\rho(x)dx} \tag{2.22}$$

is the first moment of the charge response.

In a uniform, one-sided device with no electronically active defect levels, $\delta\rho(x)$ can be approximated by a delta function in the low temperature limit

$$\delta\rho(x) \approx \delta\rho \, \delta x \, \delta(x - W), \tag{2.23}$$

where W is the width of the depletion region. Substituting Eq. 2.23 into Eq. 2.22 gives

$$\langle x \rangle = W, \tag{2.24}$$

which reduces the junction capacitance from Eq. 2.21 to the standard parallel-plate cacpacitor result

$$C = \frac{\epsilon A}{W}. \tag{2.25}$$

Characterization of $p - n$ junctions using junction capacitance provides several unique advantages. First, as seen in Eq. 2.21, the junction capacitance depends exclusively on the charge response within the the depletion region of the $p-n$ junction. Solar cells are typically $n^+ - p$ junctions (see Figure 6), with the lightly doped p-side being the absorber layer. Thus, the junction capacitance is sensitive to the charge response in *only* the absorber layer, which is often the layer of interest.[5] Second, extremely sensitive measurements of the junction capacitance are readily performed using a lock-in amplifier because the measurement already requires the use of a small AC probe voltage. Third, the width the of the depletion region can be adjusted by

---

[5]Assuming, that there are no other significant junctions elsewhere in the device.

applying a DC bias to the $p - n$ junction, which allows one to control the spatial sensitivity of the junction capacitance measurement.

Capacitance Transients in $p - n$ Junctions

Consider a $n^+ - p$ junction held under a quiescent reverse bias, with a deep defect level at energy E_D (measured with respect to the valence band). As shown in the leftmost section of Figure 7g, assume that the junction has reached steady-state, and therefore that the capacitance does not vary with time. The band diagram and charge profile for this case are illustrated in Figure 7a and Figure 7b, respectively.

Now imagine that the junction is subject to a forward bias voltage pulse. As illustrated in Figure 7c, this will collapse the depletion region and push much of the deep defect above the Fermi level. The collaspe of the depletion region causes the capacitance to increase dramatically, as shown in the middle section of Figure 7g. Previously empty defect states that are pushed above the Fermi level capture holes from the valence band at rate (c_p) such that

$$c_p = p \, \sigma_p \langle v_p \rangle, \tag{2.26}$$

where, p is the density of free holes, σ_p is the hole capture cross section of the defect state, and $\langle v_p \rangle$ is the thermal velocity of holes. Typically, this capture process is very fast compared to the time scale of the measurement, with a characteristic time of $10 \mu s$ for $p = 10^{14} \, \mathrm{cm}^{-3}$, $\sigma_p = 10^{-16} \, \mathrm{cm}^2$, $\langle v_p \rangle = 10^7 \, \mathrm{s}^{-1}$, and $T = 300 \, \mathrm{K}$ [32]. Thus, the transient capacitance associated with capture is usually not observed. This forward bias pulse is typically referred to as a "filling" pulse, because it fills previously unoccupied defect states with carriers by moving them across the Fermi level.

Next imagine that the junction is returned to the original quiescent reverse bias. As illustrated in Figure 7e, defect states that were filled by the filling pulse are now pushed back below the Fermi level, where it is statistically favorable for them to empty. This emptying occurs via thermal emission of holes into the valence band. Unlike the capture process occurring during the filling pulse, this requires that thermal energy be supplied to the holes residing in the defect state in order for them to escape. Thus, the thermal emission rate for holes (e_p) will be

$$e_p = N_V \sigma_p \langle v_p \rangle \exp\left[-\frac{E_D - E_V}{k_B T}\right], \tag{2.27}$$

where N_V is the effective density of states in the valence band (see Eq. C.18), k_B is the Boltzmann constant, and T is the absolute temperature. The exponential factor in Eq. 2.27 (known as a Boltzmann factor) causes the thermal emission rate to be very slow compared to the capture rate, i.e., $e_p \ll c_p$, with a characteristic time of $2\,\mathrm{ms}$ for $p = 10^{14}\,\mathrm{cm^{-3}}$, $\sigma_p = 10^{-16}\,\mathrm{cm^2}$, $\langle v_p \rangle = 10^7\,\mathrm{s^{-1}}$, $E_D = 0.45\,\mathrm{eV}$, and $T = 300\,\mathrm{K}$ [32]. As illustrated in Figure 7f, when the junction is initially returned to quiescent bias the depletion edge expands past the steady-state quiescent value because the carriers trapped above the Fermi level have yet to be thermally emitted. Thus, as shown in the rightmost section of Figure 7g, the capacitance is initially lower than the steady-state quiescent capacitance. As carriers are thermally emitted from the defect state, the depletion region will recede to the steady-state value, and the capacitance will increase to the steady-state quiescent value. This process of the capacitance returning to the steady-state value via thermal emission of carriers from defect states is known as a capacitance transient. Capacitance transients of this type occur on a characteristic time scale, $\tau = 1/e_p$, and contain information regarding the

energy (via the time scale of the transient) and density (via the magnitude of the capacitance transient) of the defect state responsible for their occurrence.

Spatial Sensitivity of Capacitance Transients

The form of Eq. 2.21 suggests that the junction capacitance will not have a uniform spatial sensitivity to charge in the depletion region. Indeed, following Lang [33], the non-uniform sensitivity of capacitance transients can be derived by considering an abrupt one-sided $p - n$ junction with a depletion width, W. The potential dropped across this device is simply

$$\psi(0) = \int_0^W \frac{x'\rho(x')}{\epsilon}dx'.$$ (2.28)

If one introduces a small charge of magnitude $\delta\rho$, with a width δx at a position x, then the potential across the device must be

$$\psi'(0) = \int_0^{W+\delta W} \frac{x'\rho(x')}{\epsilon}dx' - \int_0^W \frac{x'\delta\rho\,\delta x\,\delta(x)}{\epsilon}dx',$$ (2.29)

where δW is the shift in the edge of the depletion region due to the introduction of $\delta\rho$, and $\delta(x)$ is a Dirac delta function centered at x.[6] Subtracting Eqs. 2.28 and 2.29 gives the change in potential due to the introduction of $\delta\rho$

$$\delta\psi = \psi'(0) - \psi(0) = \int_W^{W+\delta W} \frac{x'\rho(x')}{\epsilon}dx' - \frac{x\delta\rho\,\delta x}{\epsilon},$$ (2.30)

---

[6]Note that the sign of δW and of the rightmost term in Eq. 2.29 implies that $\delta\rho$ has the opposite sign of $\rho(x)$, i.e., $\delta\rho$ corresponds to the trapping of majority carriers. Trapping minority carriers will result in Eq. 2.35 with the right-hand side positive.
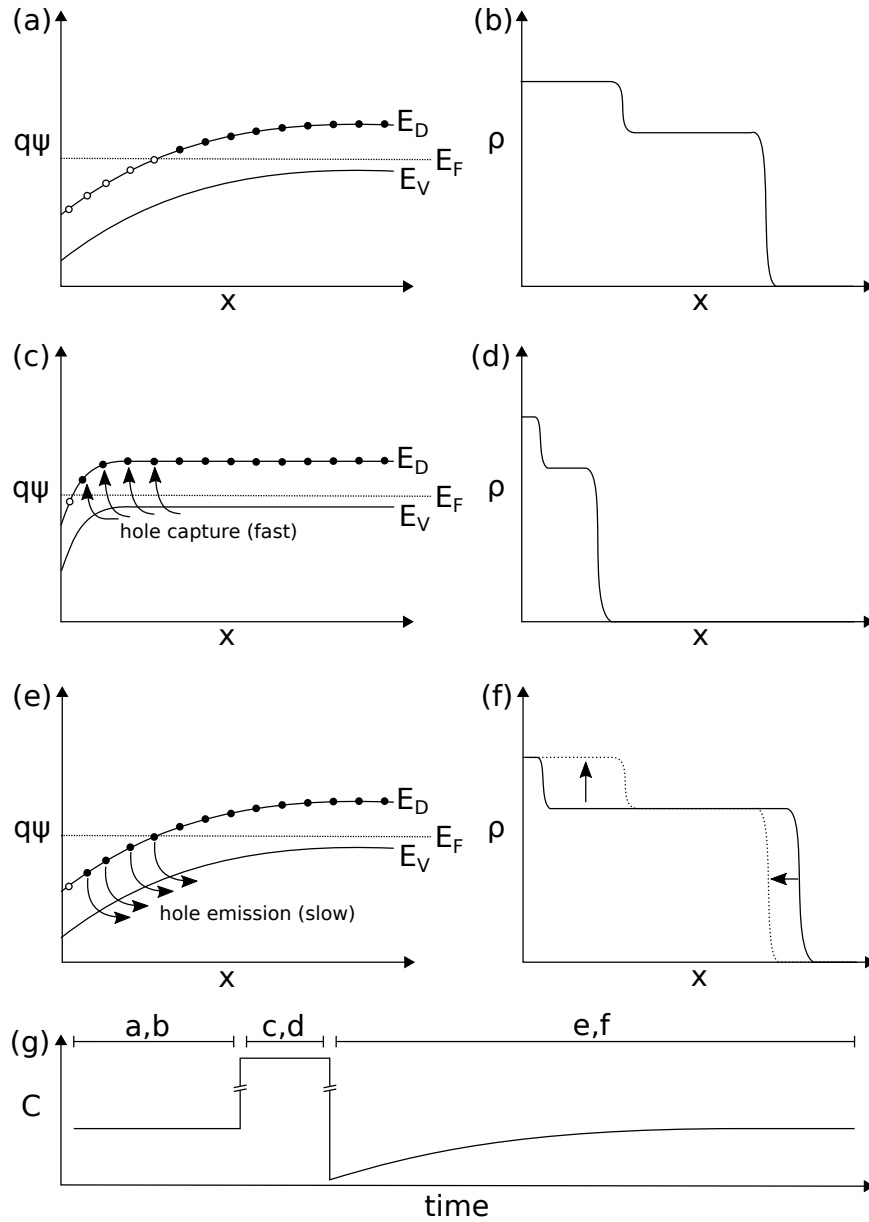
FIGURE 7. Illustration of how the charge density, potential and capacitance of a one-sided $p-n$ junction change in response to a voltage pulse. Figures (a) and (b) depict the potential and charge density profiles at equilibrium under reverse bias. Figures (c) and (d) depict the potential and charge density profiles at equilibrium during the forward bias filling pulse. Figures (e) and (f) depict the potential and charge density profiles while the sample is equilibrating (via thermal emission) after being returned to reverse bias. Figure (g) depicts the capacitance as a function of time as the device goes through the phases depicted in Figures (a)-(f).

22

or

$$\delta\psi = \frac{\rho(W)W\,\delta W}{\epsilon} - \frac{\delta\rho\,x\,\delta x}{\epsilon}. \tag{2.31}$$

Under typical measurement conditions, the DC bias is held constant when measuring the capacitance transient, thus the left-hand side of Eq. 2.31 is zero, and

$$\frac{\delta W}{W} = \frac{\delta\rho\,x\,\delta x}{W^2\rho(W)}. \tag{2.32}$$

From Eq. 2.25 one can derive the differential relation

$$-\frac{dC}{C^2} = \frac{dW}{\epsilon}, \tag{2.33}$$

or

$$-\frac{dC}{C} = \frac{dW}{W}, \tag{2.34}$$

which allows (assuming $\delta C \ll C$) one to rewrite Eq. 2.32 as

$$\frac{\delta C}{C} = -\frac{x\,\delta x\delta\rho}{W^2\rho(W)}. \tag{2.35}$$

It should be noted that using Eq. 2.34 implies that there is a small AC perturbation applied to the junction at a frequency such that only shallow dopants can respond (this does not affect the condition that the change in DC bias be zero). Eq. 2.35 makes it clear that changes to the junction capacitance depend linearly on the position of charge in the depletion region. Furthermore, it is evident that changes to the charge density at the junction interface ($x=0$) will produce *zero* change in the junction capacitance, while changes to the charge density at the depletion edge ($x=W$) will produce the largest change in the capacitance. Thus, capacitance transients are most

sensitive to changes in charge density near the depletion edge, and least sensitive to changes occurring at the interface.

Note that Eq. 2.32 also allows one to determine the spatial sensitivity of *current* transients as follows: The total change in charge, dQ, described above is simply

$$\delta Q = A\,\delta\rho\,\delta x. \tag{2.36}$$

If $\delta\rho$ are trapped majority carriers, then some portion of them do not leave the depletion region because charge is needed to shrink the depletion region.[7] The amount of charge required to do this will be

$$\delta Q' = A\rho(W)\delta W. \tag{2.37}$$

Thus, the total charge leaving the depletion region will be

$$\delta Q_{out} = \delta Q - \delta Q' = A\,\delta\rho\,\delta x - A\rho(W)\delta W. \tag{2.38}$$

Using Eq. 2.32 this can be rewritten as

$$
\begin{aligned}
\delta Q_{out} &= A\,\delta\rho\,\delta x \left(1 - \frac{\rho(W)\delta W}{\delta\rho\,\delta x}\right) \\
&= A\delta\rho\,\delta x \left(1 - \frac{x}{W}\right).
\end{aligned}
\tag{2.39}
$$

It is clear from Eq. 2.39 that majority carrier charge leaving the depletion region during the transient (i.e. the majority carrier current transient) has the opposite spatial sensitivity of capacitance.

---

[7]That is, some portion of the majority carrier charge goes to the edge of the depletion region to neutralize the space charge there—thus shrinking the depletion region.

24

Measuring Junction Capacitance

Recall that the definition of capacitance $C \equiv \delta Q / \delta V$, where δQ is the change in charge produced in response to a change in voltage δV. In the case in which δQ and δV are small, the capacitance can be expressed in terms of a derivative

$$C = \frac{dQ}{dV}. \tag{2.40}$$

Ideally, one would like to measure the capacitance by applying δV to a given device and measuring the δQ that is produced. Unfortunately, it is usually not feasible to measure δQ directly. The more practical route is to apply an AC voltage with amplitude V and angular frequency ω

$$V(t) = V \sin(\omega t), \tag{2.41}$$

and monitor the current, $I(t)$. This is because the capacitance is proportional to the magnitude of the AC current, as can be seen by calculating the AC current from Eqs. 2.40 and 2.41, yielding

$$I(t) \equiv \frac{dQ}{dt} = C\frac{dV}{dt} = \omega C V \cos(\omega t). \tag{2.42}$$

Sadly, the above relations only apply when measuring a pure capacitor. In general, a photovoltaic device will also have a resistive components both in parallel (R_P) and in series (R_S) with the junction capacitance one wishes to measure. The equivalent circuit for this scenario is shown in Figure 8.
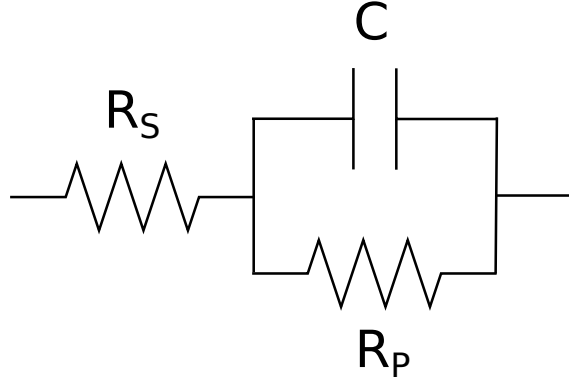
FIGURE 8. The equivalent circuit for a typical photovoltaic device. The circuit consists of a junction capacitance C, a series resistance R_S and a parallel resistance R_P.

In this case, the complex impedance of the circuit is

$$Z = R_S + \frac{1}{\frac{1}{R_P} + i\omega C}, \qquad (2.43)$$

which means the complex current will be

$$I(t) = \frac{V(t)}{Z} = V e^{i\omega t} \left[\frac{1}{R_S + \frac{1}{\frac{1}{R_P} + i\omega C}} \right], \qquad (2.44)$$

which, after separating the real and imaginary parts, becomes

$$I(t) = V e^{i\omega t} \left[\frac{\frac{1}{R_P} + \omega^2 C^2 R_S}{\left(1 + \frac{R_S}{R_P}\right)^2 + \omega^2 C^2 R_S^2} + \frac{i\omega C \left(1 + \frac{R_S}{R_P}\right)}{\left(1 + \frac{R_S}{R_P}\right)^2 + \omega^2 C^2 R_S^2} \right]. \qquad (2.45)$$

If R_S is small such that $R_S/R_P \ll 1$ and $\omega C R_S \ll 1$, then Eq. 2.45 simplifies to

$$I(t) = V e^{i\omega t} \left[\frac{1}{R_P} + i\omega C \right]. \qquad (2.46)$$

From Eq. 2.46 it is clear that the capacitance is proportional to the imaginary part of the complex impedance, and that information about the parallel resistance is contained in the real part (which is 90° out of phase). Thus, measuring the capacitance is equivalent[8] to measuring the complex phase of the AC current—a measurement for which a lock-in amplifier is particularly well-suited. In practice, measuring capacitance with a lock-in amplifier also requires that the circuit response be calibrated using a pure capacitor with an impedance similar to the device of interest.

The basic experimental setup for such capacitance measurements is shown in Figure 9. A small, 'reference' AC voltage generated by the lock-in amplifier is applied to the device under test. The resulting AC current response of the device is terminated at a current pre-amplifier, which outputs voltage that is proportional to the AC current (greatly amplified). This voltage is then routed back to the lock-in amplifier, where the real and imaginary phases of the current are separated. The imaginary part of the current (which is proportional to the capacitance) can then be read directly from the lock-in amplifier. If desired, the entire measurement can be controlled by a computer that is interfaced with the lock-in amplifier (via, e.g., a GPIB port).

---

[8]Provided, again, that R_S is small.
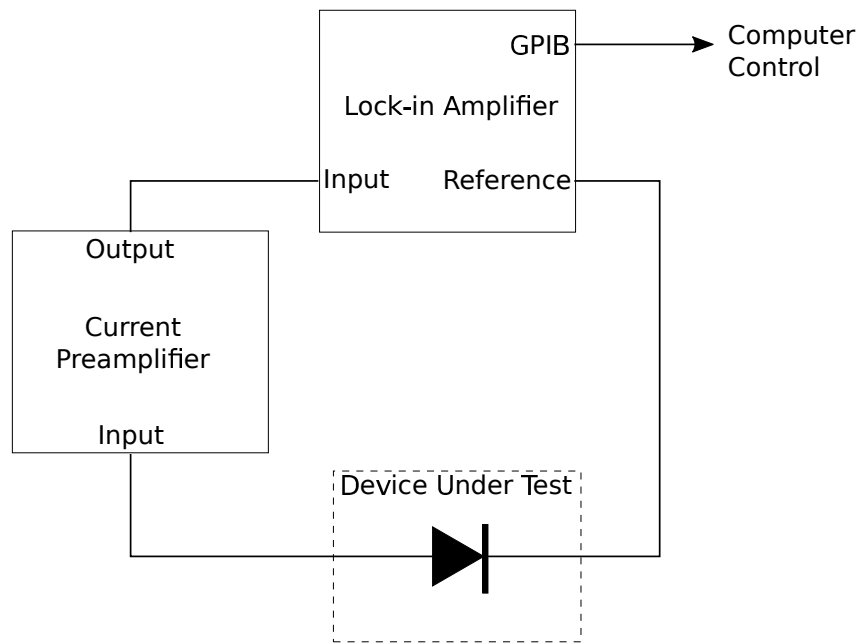
FIGURE 9. The basic experimental setup for measuring capacitance using a lock-in amplifier and a current pre-amplifier.

CHAPTER III

METHODS

Transient Photocapacitance Spectroscopy

Transient photocapacitance (TPC) spectroscopy utilizes junction capacitance and sub-bandgap monochromatic illumination to detect defect transitions in semiconductor devices. It produces spectra that are similar to standard optical absorption measurements, but with some important differences:

– Because it is based on junction capacitance, TPC spectra are only sensitive to the transitions occurring in the depletion region of the device. Solar cells are typically one-sided devices with a lightly doped absorber material, therefore the depletion region is entirely[1] within the absorber layer. Thus, TPC spectra naturally isolate the defect transitions occurring in the absorber layer from those in the other layers of the device. Since the defect transitions in the absorber layer are often the most important in terms of device performance, the ability of TPC to isolate them is advantageous.

– Because junction capacitance is sensitive to the net charge of the depletion region, and thus the type of carrier leaving the depletion region, the sign of TPC spectra indicates whether the observed transition is releasing a majority or minority carrier from the depletion region.

– Because junction capacitance can be measured very sensitively with a lock-in amplifier, TPC spectra can detect sub-bandgap transitions that are extremely weak compared to band-to-band transitions.

_____

[1]to a very good approximation

TPC was pioneered to facilitate the study of gap states in amorphous Silicon (a-Si) by J. D. Cohen, A. V. Gelatos (University of Oregon) and J. P. Harbison (Bell Labs) [30, 34–44], as well as by D. K. Biegelsen and N. M. Johnson (Xerox) [45]. The Oregon group went on to apply the technique to the study of gap states in SiGe [39, 40, 46–49], $CuIn_{1-x}Ga_xSe_2$ [50–53], Zinc Tin Oxide [54], nanocrystalline Silicon [55, 56], $Cu_2ZnSn(S, Se)_4$ [57] and CdTe [58, 59].

The general sequence of events for a TPC measurement is illustrated in Figure 10. The device of interest is held under a quiescent bias V_Q (typically reverse bias or no bias), and a resultant capacitance C_Q is exhibited. A forward bias pulse V_P is then applied to the device, causing the capacitance to increase dramatically to C_P. The device is then returned to quiescent bias, and the resulting capacitance transient $C^{light}(t)$ is observed under monochromatic illumination. Next, the monochromatic illumination is removed, a second forward bias pulse is applied, and the resultant capacitance transient $C^{dark}(t)$ is observed in the dark. The TPC signal is defined to be the normalized integrated difference between the light and dark transients

$$S^{TPC}(E) \equiv \frac{1}{\Phi(E)} \int C^{light}(E, t) - C^{dark}(t) dt, \qquad (3.1)$$

where $\Phi(E)$ is the photon flux at monochromatic energy E. During $C^{dark}(t)$ the device is equilibrating entirely through thermal processes, while during $C^{light}(t)$ optical processes are occurring in additional to the thermal ones. Thus, $C^{light}(E, t) - C^{dark}(t)$ isolates the optical contribution to $C^{light}(E, t)$ by canceling off the thermal contribution to the transient. Varying the monochromatic illumination energy E, produces a TPC *spectrum*.

In principal, the limits of the integral in Eq. 3.1 are over the entire length on the transient. In practice, the lock-in amplifier used to measure the capacitance takes on

the order of 10 cycles to properly lock on to the capacitance signal after the voltage pulse is removed. Thus, the integration window is typically adjusted to cut off the part of the transient that is influence by the recovery of the lock-in amplifier.

Notice that in Figure 10 there are two behaviors that will produce a non-zero capacitance signal. The first behavior is a vertical offset between the light and dark transients such that $C^{\mathrm{light}}(t) = C^{\mathrm{dark}}(t)+$constant (the *shape* of the both transients are identical). This occurs when a state is far enough from the Fermi level that the voltage pulse does not cause it to change it's occupation. In this case, the illumination will produce a steady-state change in the occupancy of the state—resulting in a constant shift in $C^{\mathrm{light}}(t)$ with respect to $C^{\mathrm{dark}}(t)$. The second behavior is one in which the light transient plateaus faster (or slower) than dark transient, but both transients plateau to the same capacitance value. In this case, the light is assisting (or inhibiting) the thermal emission of trapped carriers from a state (as described in Chapter II). One benefit of this type of behavior is that it allows the competition between optical and thermal processes to be observed, but it also requires that the time scale of the TPC measurement be tuned to a range that allows the thermal transient to be seen. In general, both types of behavior will be present during a TPC measurement.

The optical contribution to $C^{\mathrm{light}}(E,t)$ is proportional to the integrated density of states accessible at the monochromatic illumination energy. To understand how, consider that the rate $R(E)$ at which photons induce carrier transitions in a semiconductor is proportional to the integral

$$R(E) \propto \int |\langle i|ex|f\rangle|^2 g_{unocc}(E')g_{occ}(E' - E)dE', \tag{3.2}$$

where E is the energy of the photon, and $|\langle i|ex|f\rangle|^2$ is the optical matrix element associated with the relevant transition from unoccupied states with density g_{unocc} to
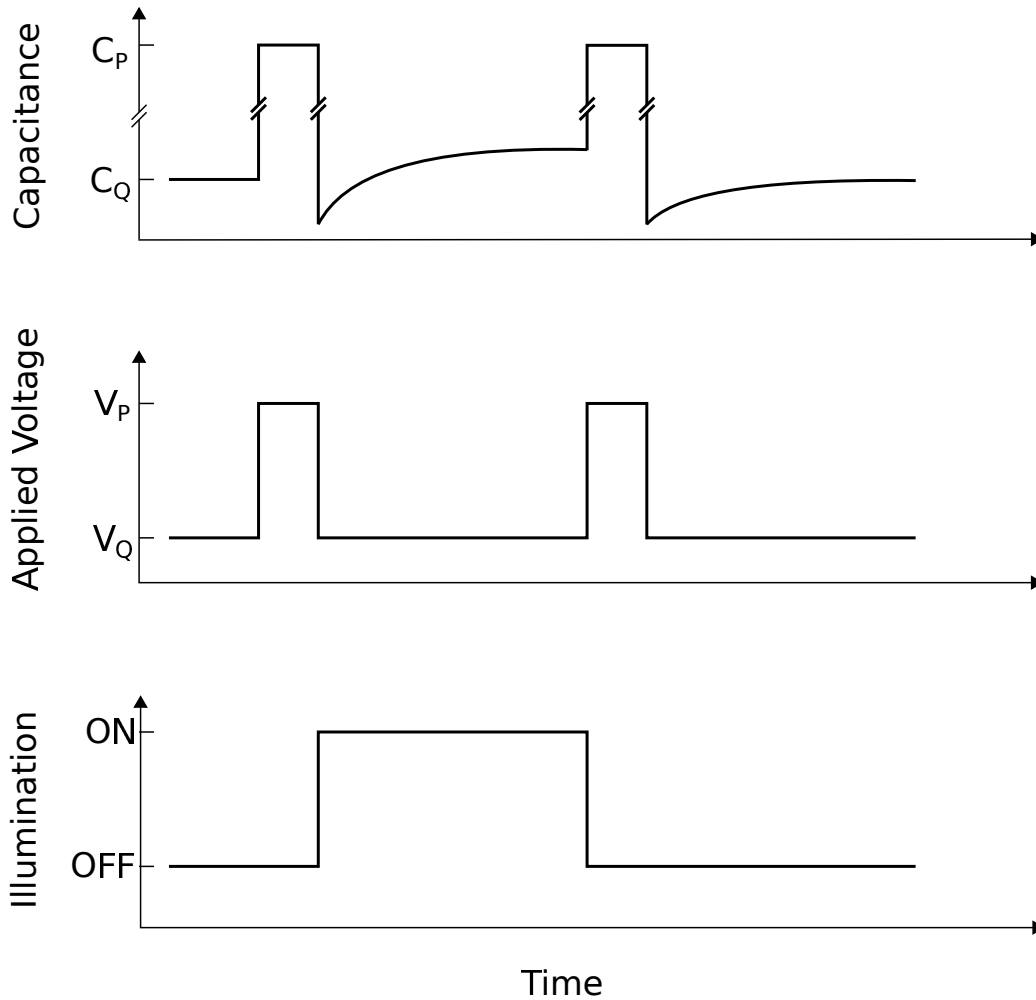
FIGURE 10. Schematic of a TPC measurement. Initially, the device is held under a quiescent bias V_Q, and exhibits a capacitance C_Q. Next, a forward bias pulse V_P is then applied to the device, causing the capacitance to increase dramatically to C_P. Then, the device is returned to quiescent bias, and the resulting capacitance transient is observed under monochromatic illumination. The monochromatic illumination is then removed, and a second forward bias pulse is applied. After returning the device to quiescent bias again, the resultant capacitance transient is observed in the dark. The TPC signal is the normalized integrated difference between the light and dark transients.

occupied states with density g_{occ}. In the case of a semiconductor being illuminated with sub-bandgap light, there are two relevant transitions to consider: those from the valence band to unoccupied gap states

$$R_V(E) \propto \int_{E_F}^{E_V+E} |\langle i|ex|f \rangle|^2 g(E') g_V(E' - E) dE',$$ (3.3)

and those from an occupied gap states to the conduction band

$$R_C(E) \propto \int_{E_C-E}^{E_F} |\langle i|ex|f \rangle|^2 g(E') g_C(E' + E) dE'.$$ (3.4)

Note that Eq. 3.3 only applies when $E_V + E > E_F$ and Eq. 3.4 only applies when $E_C - E < E_F$; they are zero otherwise.[2] For TPC, only transitions that produce a change in the net charge of the depletion region will contribute.[3] For example, promoting a electron from a defect state to the conduction band will only contribute to the TPC signal if the hole that is left behind does not escape to the valence band via thermal emission (on the time scale of the TPC measurement). In general, charge left behind by an optical transition will escape thermally if it is within a thermal energy depth

$$E_e = k_B T \log(\nu\tau)$$ (3.5)

of the relevant band. Here, ν is the thermal emission prefactor for the relevant gap state, and τ is the time scale of the TPC measurement. Thus, one can modify Eqs. 3.3 and 3.4 to make them appropriate for TPC by adjusted the integration limits such

---

[2]This nicely separates the occupied and unoccupied parts of $g(E)$ into the proper integrals as well.

[3]This is because the TPC signal is proportional to the junction capacitance, which depends on the *net* charge of the depletion region.

that

$$R_V^{\text{TPC}}(E) \propto \int_{E_V+E_e}^{E_V+E} |\langle i|ex|f\rangle|^2 g(E')g_V(E'-E)dE', \tag{3.6}$$

and

$$R_C^{\text{TPC}}(E) \propto \int_{E_C-E}^{E_C-E_e} |\langle i|ex|f\rangle|^2 g(E')g_C(E'+E)dE'. \tag{3.7}$$

Fortunately for the semiconductor physics community, it turns out that the optical matrix element and the density of states in the conduction band (or valence band) both vary slowly in energy space with respect to $g(E)$ (see, e.g., [60] and [61]). This allows one to approximate these quantities as constants, leading to the much simpler and more useful expressions

$$R_V^{\text{TPC}}(E) \propto \int_{E_V+E_e}^{E_V+E} g(E')dE', \tag{3.8}$$

and

$$R_C^{\text{TPC}}(E) \propto \int_{E_C-E}^{E_C-E_e} g(E')dE'. \tag{3.9}$$

Considering that the TPC signal is defined by isolating the optical contribution to the capacitance transient, it is apparent that

$$S^{\text{TPC}}(E) \propto R^{\text{TPC}}(E) \propto \int g(E')dE', \tag{3.10}$$

and therefore that $S^{\text{TPC}}(E)$ as defined in Eq. 3.1 is proportional to the integrated density of states. In the case of a p-type semiconductor, this relation is more precisely

formulated as

$$
\begin{aligned}
S^{\mathrm{TPC}}(E) &= K(T,\tau,\omega)\left[S_V^{\mathrm{TPC}}(E) - S_C^{\mathrm{TPC}}(E)\right] \\
&= K(T,\tau,\omega)\left[\int_{E_V+E_e}^{E_V+E} g(E')dE' - \int_{E_C-E}^{E_C-E_e} g(E')dE'\right],
\end{aligned}
\tag{3.11}
$$

where $K(T,\tau,\omega)$ is a constant that does not depend on E. Note that S_V^{TPC} represents the release of a majority carrier (a hole) from the depletion region and S_C^{TPC} represents the release of a minority carrier (an electron). The release of a majority carrier will shrink the depletion region[4] (increasing capacitance), while the release of a minority carriers from the depletion region will cause the depletion region to expand (decreasing capacitance). Thus, S_V^{TPC} and S_C^{TPC} must enter Eq. 3.11 with opposite signs, and the sign of $S^{\mathrm{TPC}}(E)$ will indicate whether a minority or majority carrier transition is occurring. This is crucial for determining whether the energy of a transition is with respect to the valence band or conduction band.

Shown in Figure 11 are examples of the types of transitions that can contribute to a typical TPC spectrum. These include: (a) band-to-band transitions, which will dominate when illuminating the device with above-gap light. If there is perfect carrier collection from the depletion region, then the band-to-band contribution to the TPC signal will be zero because the net charge of the depletion region will not change. Typically, minority carriers are not collected perfectly and the band-to-band transitions result in a large, positive TPC signal; (b) bandtail transitions, which will dominate when illuminating with light that is just below the bandgap. Bandtail states exist in all amorphous materials, and the width of the bandtails is generally associated

---

[4]A released majority carrier leaves behind a charge that has the same sign as the space charge in the depletion region. Thus, releasing a majority carrier *increases* the charge density in the depletion region, which means the depletion region must *shrink* in order the drop the same voltage across the device (the device is being held at a fixed bias.
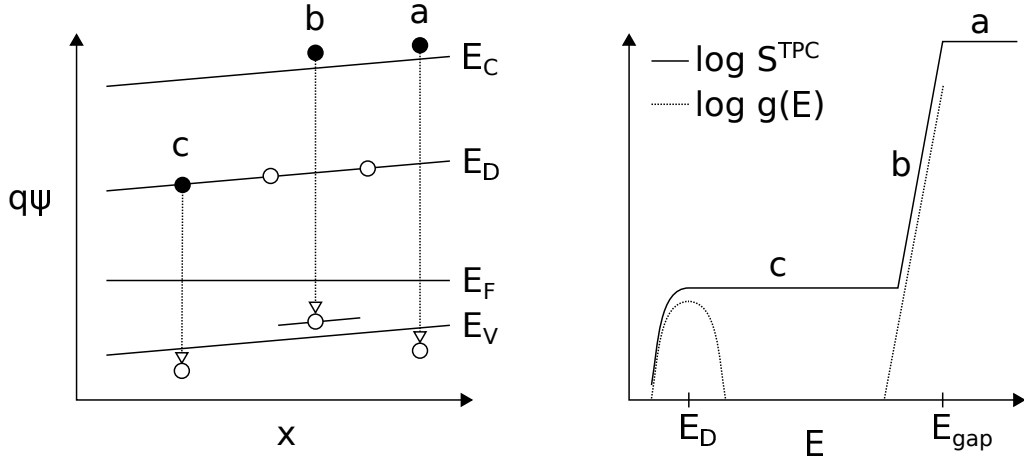
FIGURE 11. Illustration of the types of transitions that contribute to TPC. The transitions labeled on the left are responsible for the region of the TPC spectrum with the same label. These include: (a) band-to-band transitions, (b) bandtail transitions, and (c) defect transitions (in this case, the defect has an energy E_D measured with respect to the valence band).

with a more disordered material [62]. Bandtails are also referred to as an Urbach edge, characterized by the Urbach energy E_U, defined such that $g(E) \propto \exp[E/E_U]$ in the bandtail region [63]; (c) defect transitions, which will dominate for sub-bandgap light with sufficiently low energy[5]. Typically, the defect states observed have a Gaussian distribution in energy space with the center of the distribution at the 'energy' of the defect.

An example of a TPC spectrum of CdTe thin film solar cell is shown in Figure 12. As shown in the figure, typical analysis of a TPC spectrum involves fitting the data with an integrated density of states (involving an Urbach edge and one or more Gaussian defect states). Also shown is the density of states corresponding to the fit, which is simply found by differentiating the integrated density of states with respect to energy.

---

[5]Provided there are defects present in the device at observable densities
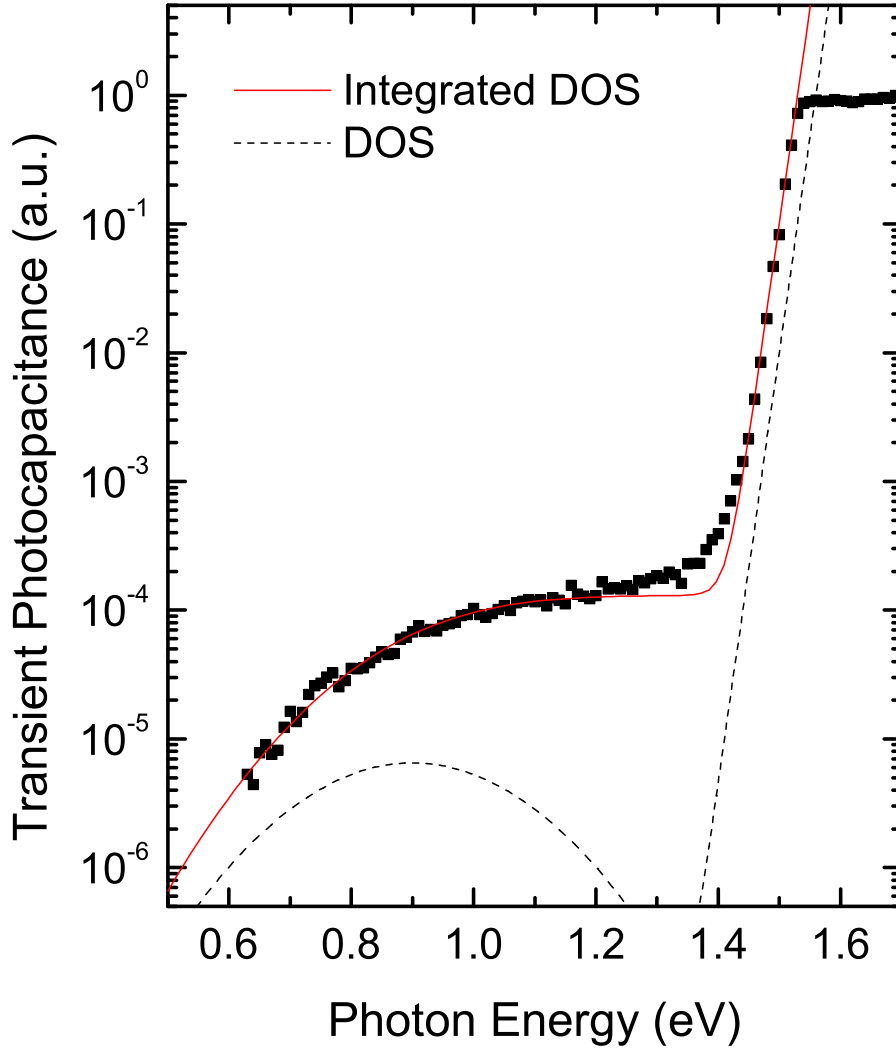
FIGURE 12. The TPC spectrum of a CdTe thin film solar cell. The solid red line indicates the integrated density of states (DOS) that best fit the data. The dashed black line indicates the underlying DOS corresponding to the best fit. The spectrum exhibits an Urbach energy of 13 meV and single Gaussian defect level centered at 0.9 eV (measured with respect to the valence band).

A schematic of the instrumentation used to collect TPC spectra is shown in Figure 13. For the TPC spectra presented in this work, monochromatic light was generated by a McPherson 205WR monochromator with a 550W quartz-tungsten halogen lamp in combination with long-pass filters to attenuate high energy stray light.[6] Overall intensity of the light was further attenuated using neutral density filters, ensuring the linear response of the device under test.[7] Voltage pulses generated using a Tektronix AFG3022B function generator were combined with a $30\,mV$, $10\,kHz$ AC probe voltage generated by the Stanford Research Systems SR850 lock-in amplifier, and sent to the device. The response of the device, which was mounted in a Linkam LTS350 liquid nitrogen temperature control stage[8], was sent to a Stanford Research Systems SR570 current preamplifier. The amplified signal was then fed to the SR850 lock-in amplifier, which passed the capacitive phase to a Tektronix TDS3014C oscilloscope, which recorded the device response data. The TPC signal itself was calculated in software from the oscilloscope data.

Transient Photocurrent Spectroscopy

Complementary to TPC is transient photocurrent spectroscopy (TPI). A TPI measurement is carried out in exactly the same manner as TPC, except the current is monitored instead of the capacitance. Experimentally, this is achieved by bypassing the lock-in amplifier in Figure 13. Because the lock-in amplifier is no longer used, TPI spectra are generally less sensitive than TPC.

---

[6]Because the density of sub-bandgap states is much less than the density of states in the bands, even a very small amount of high energy stray light can produce a signal that totally overwhelms the signal due to sub-bandgap transitions.

[7]This also ensures that there is negligible quasi-Fermi level splitting, and reduces any sort of light-induced metastabilities.

[8]Sample temperature ranged from $160\,K$ to $200\,K$ depending on the device.

In the context of this work, the important difference between TPC and TPI is that the TPI spectra of different devices are more readily compared. Ideally, one would like to be able to align the above-gap portion of TPC spectra from different samples in order to compare the magnitude of sub-bandgap defect states that are observed. Unfortunately, the magnitude of the above-gap TPC signal depends sensitively on the relative collection of minority and majority carriers. If minority and majority carriers are both collected perfectly, band-to-band transitions will have *zero* contribution to the above-gap TPC signal because the *net* change in charge will be zero. If minority carriers are *never* collected, then the net change in charge will be maximized, and band-to-band transitions will dominate the above-gap TPC signal. Because current depends on the *total* charge leaving the depletion region, TPI does not suffer in this way, and the above bandgap signal simply depends on the total number of free carriers contributing to the current. Therefore, TPI spectra can be scaled such that they align at the bandgap energy, allowing the relative magnitude of defect states to be compared between samples.[9]

As discussed in Chapter II, current and capacitance transients have opposite spatial sensitivity, thus TPI is more sensitive to junction interface region of the device, while TPC is more sensitive to the region near the depletion edge. This is an important consideration to keep in mind when comparing the TPC and TPI spectra of non-uniform devices.

---

[9]Notice that any mechanisms that affect the total current (e.g., series resistance) will affect all parts of a TPI spectrum *equally* in the low injection limit—e.g., once photo-excited electrons have entered the conduction band their behavior does not depend on whether they were excited from a defect state or from a valence band state.

Time-of-Flight Secondary Ion Mass Spectrometry

Time-of-flight secondary ion mass spectrometry (ToF-SIMS) is a technique capable of determining elemental composition of films as a function of depth [64]. In ToF-SIMS, the elemental composition of a given surface is determined by bombarding it with energetic 'primary' ions and performing time-of-flight mass spectrometry on the 'secondary' ions that are emitted as a result (see Figure 14). In order to increase the signal-to-noise ratio, the primary ion beam is typically rastered across a surface area of roughly $100\,\mu\text{m} \times 100\,\mu\text{m}$.

The basic principle of time-of-flight spectrometry is that secondary ions are extracted from the surface region of the sample and accelerated to a known potential energy via and extraction potential V. The time t it takes for a secondary ion with mass-to-charge ratio m/z to reach a particle detector at a distance L will be

$$t = L \left(\frac{m}{2zV} \right)^{1/2}. \tag{3.12}$$

Thus, the mass-to-charge ratio of the secondary ions can be calculated from their arrival time at the detector. In practice, accurate timing requires that the primary ions be delivered over a very short duration pulse (typically nanoseconds). Further, the secondary ions are not all emitted with identical energies, therefore a precisely calibrated ion mirror is required to offset the energy distribution of the secondary ions [64]. The ion mirror reflects ions using a retarding field that increases in strength as ions move into the mirror. This results in more energetic ions penetrating further into the mirror, which increases their time-of-flight and compensates for their increased initial energy.

Depth profiles are obtained by using a sputter beam to create a sputter crater on the analysis area of the film (see Figure 15a). The sputter beam is interlaced with the primary ion analysis beam, ensuring the analysis beam is bombarding the bottom of a successively deeper sputter crater as the measurement proceeds (see Figure 15b). In this way, elemental abundances can be determined as a function of depth for several microns into the film.

It is important to keep in mind that the ion yield under bombardment varies over several orders of magnitude for different elements, materials, and primary ions. Thus, the elemental abundances determined by ToF-SIMS are not quantitative, unless a film of known composition is used to calibrate the ion yields. Furthermore, since the sputter rate is heavily dependent on the film composition and the type of sputter ion used, the depth axis of ToF-SIMS data needs to be calibrated by the determining the relevant film thicknesses through some other means (e.g., from scanning electron microscopy images).

The ToF-SIMS depth profile data presented in this work, were collected with an ION-TOF Model IV operated by Dr. Stephen Golledge of the Center for Advanced Materials Characterization in Oregon (CAMCOR) Surface Analytical Facility. In all cases, a $25\,\mathrm{keV}$ Bi_3^+ primary ion beam with a current of $0.3\,\mathrm{pA}$ was used to analyze a $100\,\mu\mathrm{m} \times 100\,\mu\mathrm{m}$ area. A $2\,\mathrm{keV}$ beam of O_2 ions (at a current of $300\,\mathrm{pA}$) was used to sputter a $300\,\mu\mathrm{m} \times 300\,\mu\mathrm{m}$ crater for the depth profiles. Copper profiles were normalized with respect to tellurium in all cases.
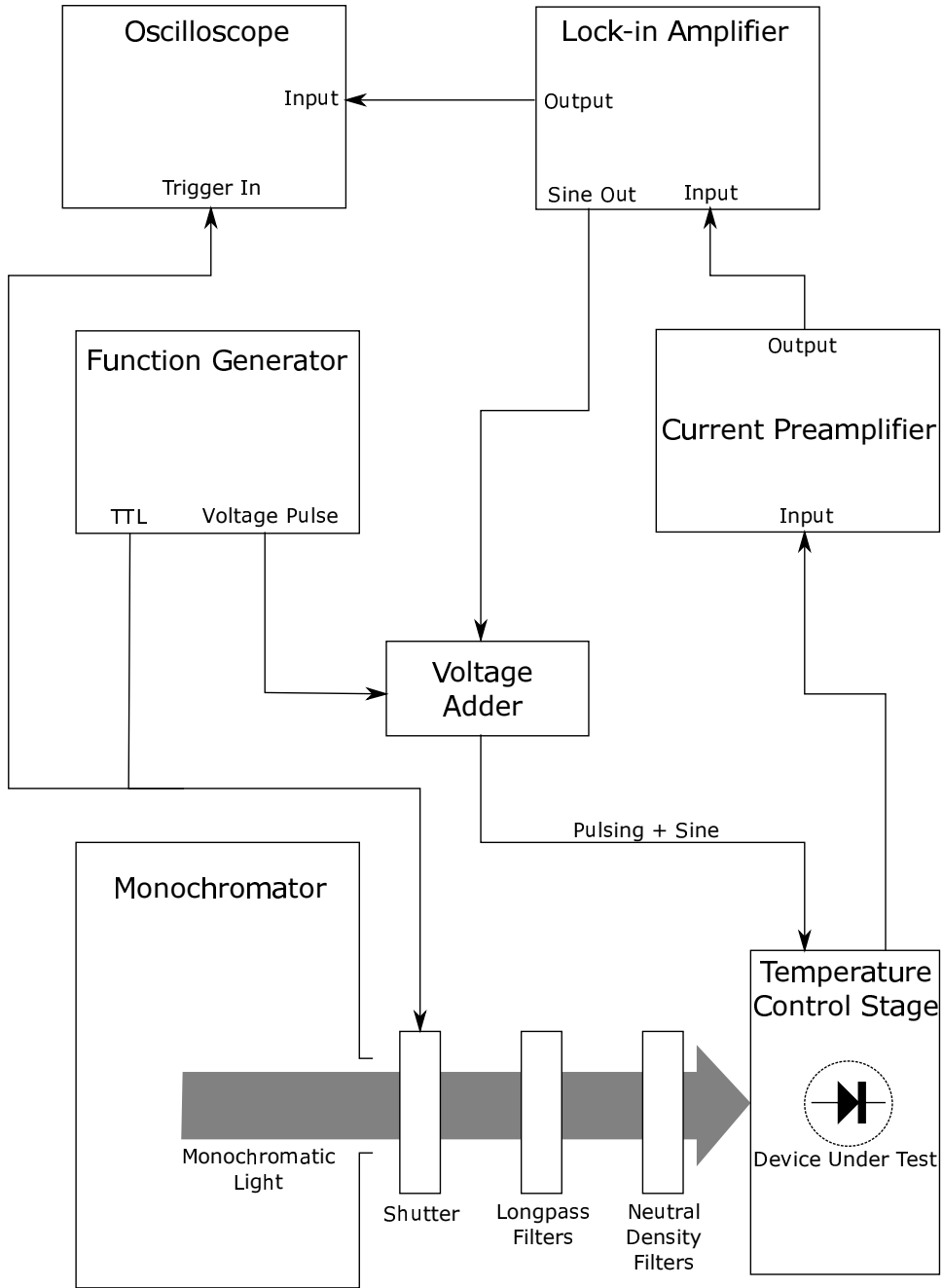
FIGURE 13. Schematic of a TPC experiment.
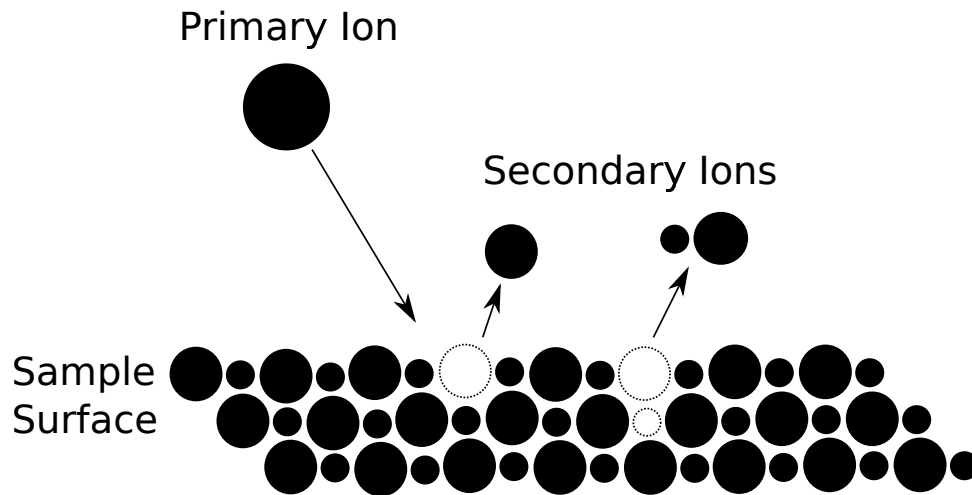
FIGURE 14. Schematic of the ToF-SIMS bombardment process.
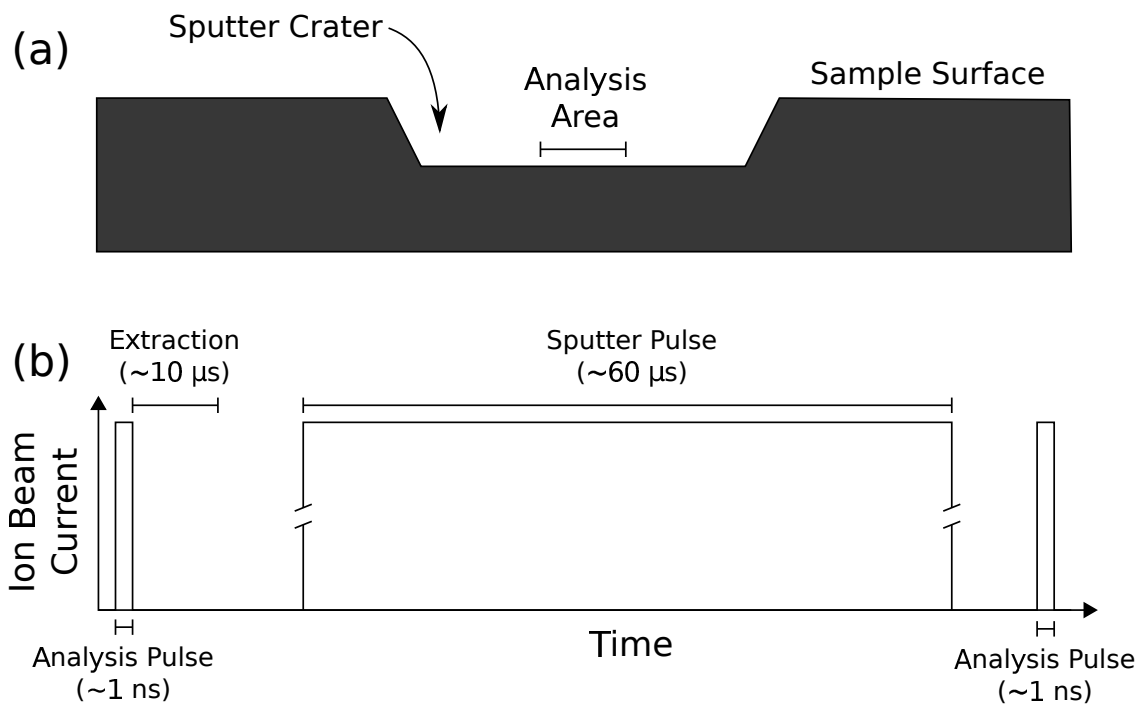
FIGURE 15. Illustration of (a) the sputter crater created during a depth profile and (b) how the analysis and sputter beams are interlaced during a depth profile.

CHAPTER IV

SAMPLES

In order to ensure that the results of this work were not a by-product of the deposition technique, the superstrate CdTe solar cells studied were fabricated using two separate techniques: vapor transport deposition (VTD) and close space sublimation (CSS). The VTD devices were deposited at $400\,^{\circ}$C, while the CSS devices were deposited at $600\,^{\circ}$C. The structure of the VTD devices, which were fabricated by Jiaojiao Li and Dr. Colin Wolden at the Colorado School of Mines (CSM) is shown in Figure 17a. For CSS devices (structure shown in Figure 17b), the FTO to CdTe layers were deposited by Daniel Meysing (CSM) and Dr. Teresa Barnes at the National Renewable Energy Laboratory (NREL), while the deposition of the ZnTe:Cu/Au back contact and subsequent thermal processing was performed at CSM by J. Li and C. Wolden. All devices received a $CdCl_2$ treatment at $400\,^{\circ}$C, as is typical for high-performance CdTe solar cells [4]. The processing methods, performance parameters, and back contact types of the samples studied are summarized in Table 1 and plotted in Figure 16.

The thin-film CdTe devices studied in this work were prepared in such a way as to control copper content and minimize copper contamination. Typically, CdTe/ZnTe:Cu devices have the ZnTe:Cu layer deposited at relatively high temperatures (on the order of $300\,^{\circ}$C) for relatively extended periods of time (on the order of $2\,$hr). These fabrication conditions deposit the ZnTe:Cu whilst simultaneously diffusing copper into the CdTe layer [24]. In contrast, the devices fabricated for this work decouple the ZnTe:Cu deposition from the diffusion of copper into the CdTe layer, thus enabling a careful study of role of copper. This was done by

44

TABLE 1. Processing methods, typical cell performance parameters and back contact type for the classes of devices studied.

Sample	Processing	Eff. (%)	FF (%)	V_{OC} (mV)	J_{SC} (mA/cm^2)	Back Contact
Optimal	VTD	13.2	67	810	24.3	ZnTe:Cu
Overannealed	VTD	8.9	56	792	20.0	ZnTe:Cu
Undoped	VTD	5.4	53	561	18.1	ZnTe
As-deposited	VTD	6.7	48	595	23.5	ZnTe:Cu
Optimal	CSS	14.9	68	828	26.5	ZnTe:Cu
Overannealed	CSS	7.8	48	671	24.1	ZnTe:Cu
Underannealed	CSS	3.7	41	691	13.2	ZnTe:Cu
As-deposited	CSS	0.3	35	359	2.5	ZnTe:Cu
Comparison[58]	CSS	14.1	72	840	23.5	Cu$_x$Te
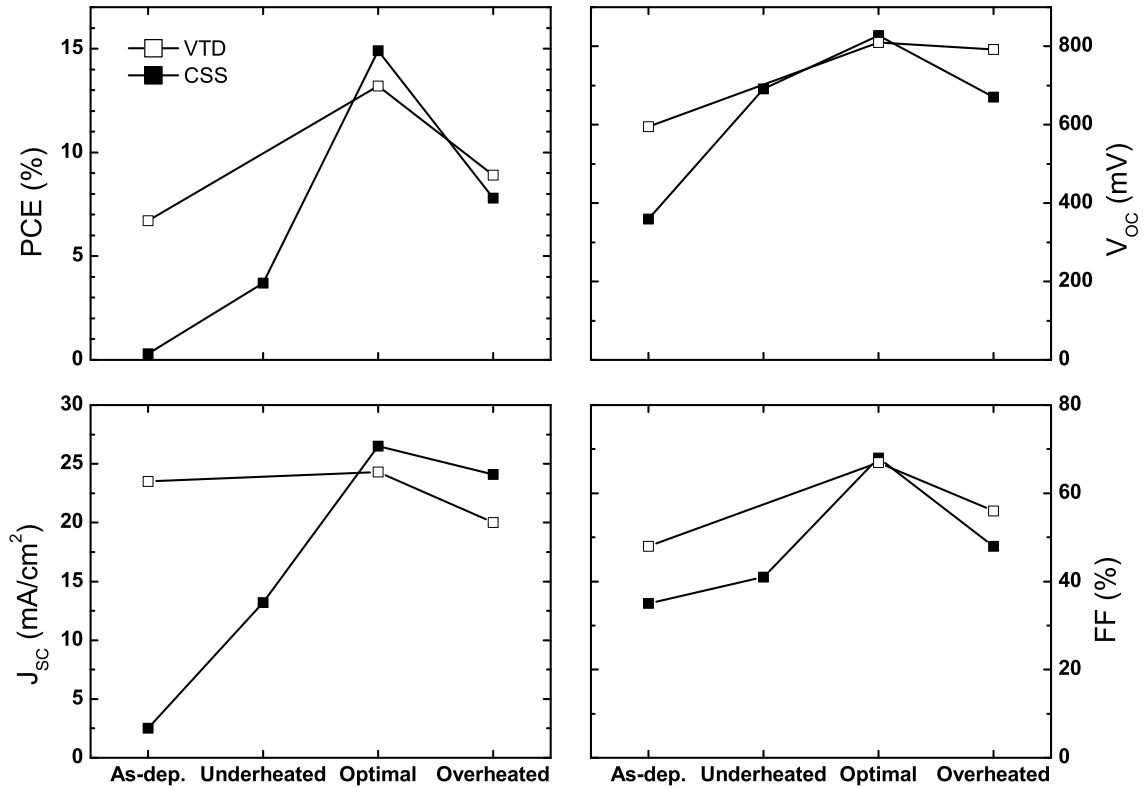
FIGURE 16. Power conversion efficiency (PCE), open-circuit voltage (V_{OC}), short-circuit current density (J_{SC}), and fill factor (FF) for the classes of devices studied.
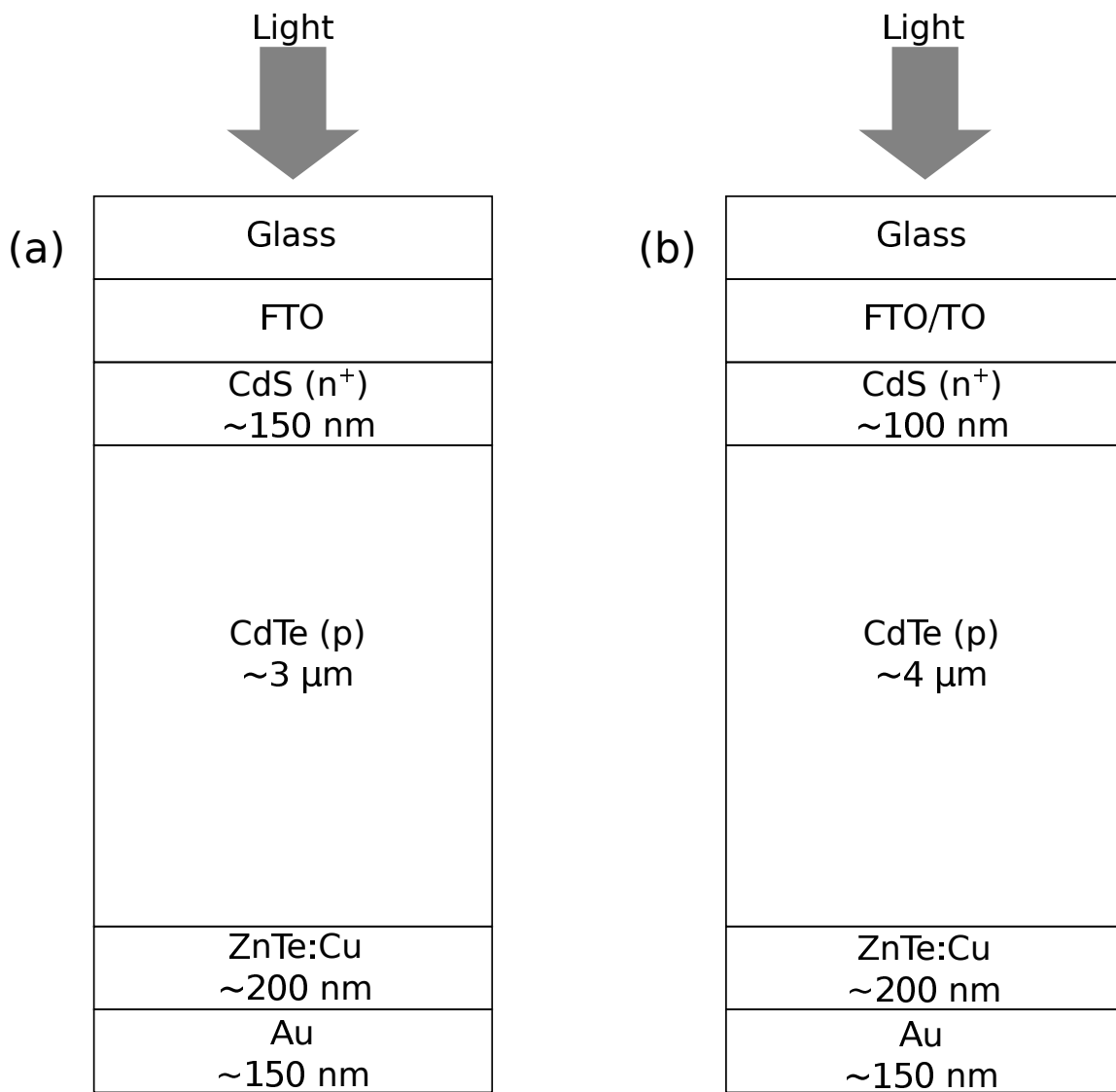
FIGURE 17. Structure of (a) the VTD devices, and (b) the CSS devices.

depositing ZnTe:Cu using thermal evaporation at a low enough temperature (roughly $100\,^{\circ}$C) such that little or no copper diffusion occured during the deposition. The low temperature deposition was followed by a $30\,$s rapid thermal processing (RTP) step[1], which diffused copper into the CdTe layer. Adjusting the parameters of the RTP step enabled the extent to copper diffusion into the CdTe layer to be precisely controlled. For further information regarding the RTP process and the fabrication of the VTD devices, refer to Li et. al [17]. For further information regarding the fabrication of the CSS device see Meysing et. al [65].

In all, five classes of devices were fabricated for the purposes of this work. They include:

- (1) 'Optimal' devices. These devices represented the RTP conditions which produced the optimal devices in terms of power conversion efficiency (PCE). They had an intermediate amount of copper in the CdTe layer compared to the other classes of devices.

- (2) 'Overannealed' devices. These devices were exposed to either an additional RTP step relative to the optimal devices or a single RTP step at temperature higher than that of the optimal processing. As a result, they had increased Cu content in the CdTe layer compared to the optimal devices, as well as a reduced PCE.

- (3) 'Underannealed' devices. These devices were exposed to a lower temperature RTP step relative to the optimal devices. This resulted in a less copper in the CdTe layer compared to the optimal devices, and and a reduced PCE.

---

[1]The RTP temperature was roughly $300\,^{\circ}$C.

- (4) 'Undoped' devices. These devices were given the optimal RTP treatment, but lacked intentional Cu doping in the ZnTe layer (i.e., the back contact layer was ZnTe instead of ZnTe:Cu). Since elements other than copper diffuse into the CdTe layer during the RTP step (most notably zinc), these devices were necessary to ensure that the effects seen in other devices could truly be attributed to copper. The undoped devices had very low PCE, and showed no evidence of copper in the CdTe layer.

- (5) 'As-deposited' devices. These devices served as a control, and were identical to the optimal devices, except they lacked the RTP treatment altogether.[2] They also had very low PCE, and also showed evidence of copper diffusion into the CdTe layer.

Typical current-voltage curves for these classes of devices are shown in Figures 18 and 19.

In addition to the devices fabricated specifically for this study, this work will also refer to a 'Comparison' device from Boucher et al. [58], which had conventional processing conditions and the commonly used Cu_xTe back contact. This device allowed the conclusions drawn from the CdTe/ZnTe:Cu devices to be generalized beyond the specific back contact scheme employed.

---

[2]They still recieved the $CdCl_2$ treatment, which occured before the deposition of the back contact layer.
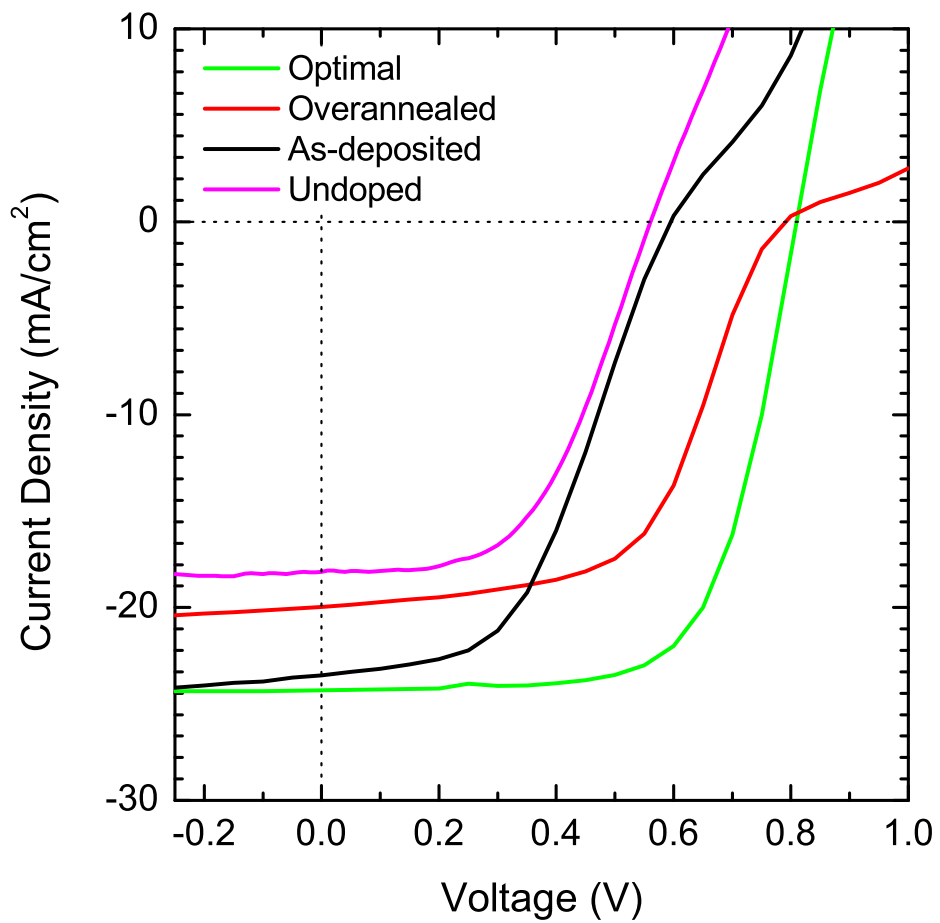
FIGURE 18.   Typical current-voltage characteristics for the VTD devices under AM1.5 illumination.
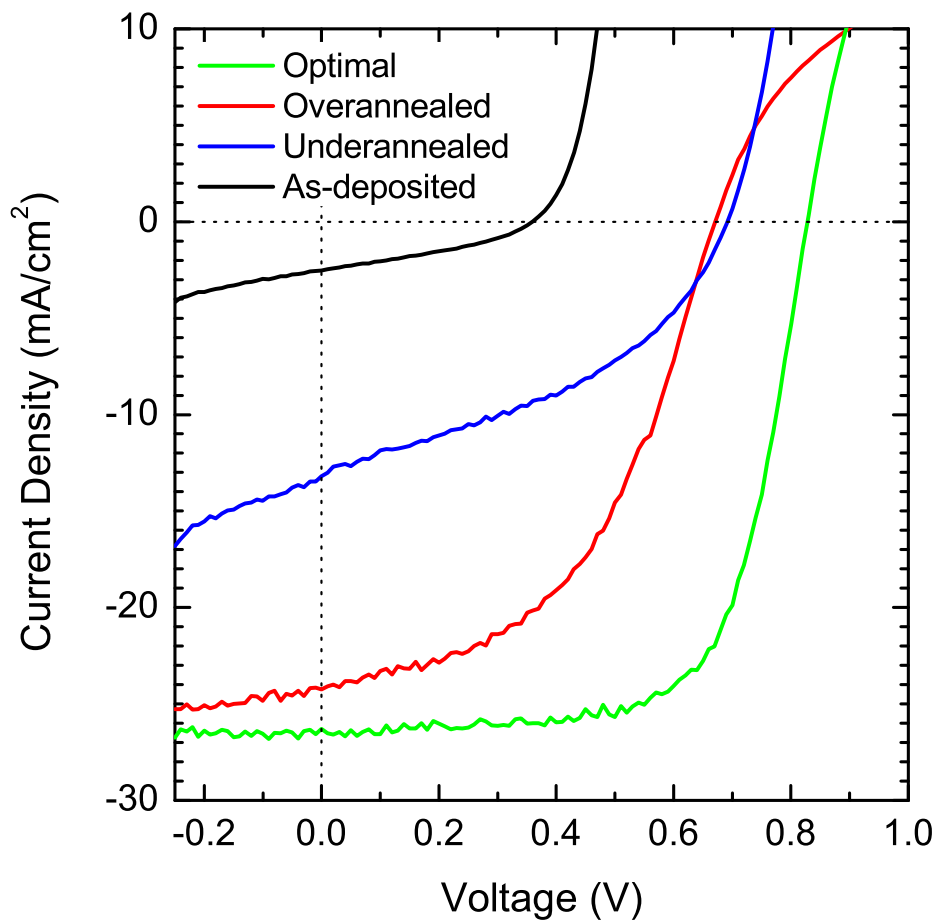
FIGURE 19. Typical current-voltage characteristics for the CSS devices under AM1.5 illumination.

RESULTS

Transient Photocapacitance Spectroscopy and Time-of-Flight Secondary Ion Mass Spectrometry

TPC spectra of the VTD and CSS devices are shown in Figures 20 and 21, respectively. All devices studied exhibit a bandgap $E_g \approx 1.5\,\text{eV}$ (as would be expected for CdTe), an Urbach edge with E_U ranging $15\,\text{meV}$ to $25\,\text{meV}$, and a defect at $E_V + 1.2\,\text{eV}$. The Urbach energies and defect energies were determined by numerically fitting the spectra using the least squares method. Devices in which copper has been intentionally diffused into the CdTe layer (the optimal and overannealed devices) show an increased TPC signal at low optical energies as compared to devices without intentional copper doping (the undoped and as-deposited devices). This suggests the presence of an additional defect in the CdTe layers which contain copper. Indeed, numerical fitting of the TPC spectra for the copper containing devices used a Gaussian defect centered at $E_V + 1.2\,\text{eV}$ and an additional Gaussian defect centered at $E_V + 0.9\,\text{eV}$ for the best fit. Thus, the $0.9\,\text{eV}$ defect is associated with copper because it only appears when copper is present in the CdTe layer. The parameters of the best fit for each device are given in Table 2.

The absence of copper in the CdTe layer of the as-deposited devices, as well as the presence of copper in the CdTe layers of the optimal and overannealed devices, was confirmed via ToF-SIMS depth profiles (shown in Figures 22 and 23 for the VTD and CSS devices, respectively). In Figures 22 and 23 it is evident that there is little to no copper diffusion in the as-deposited device, and increasing diffusion of copper
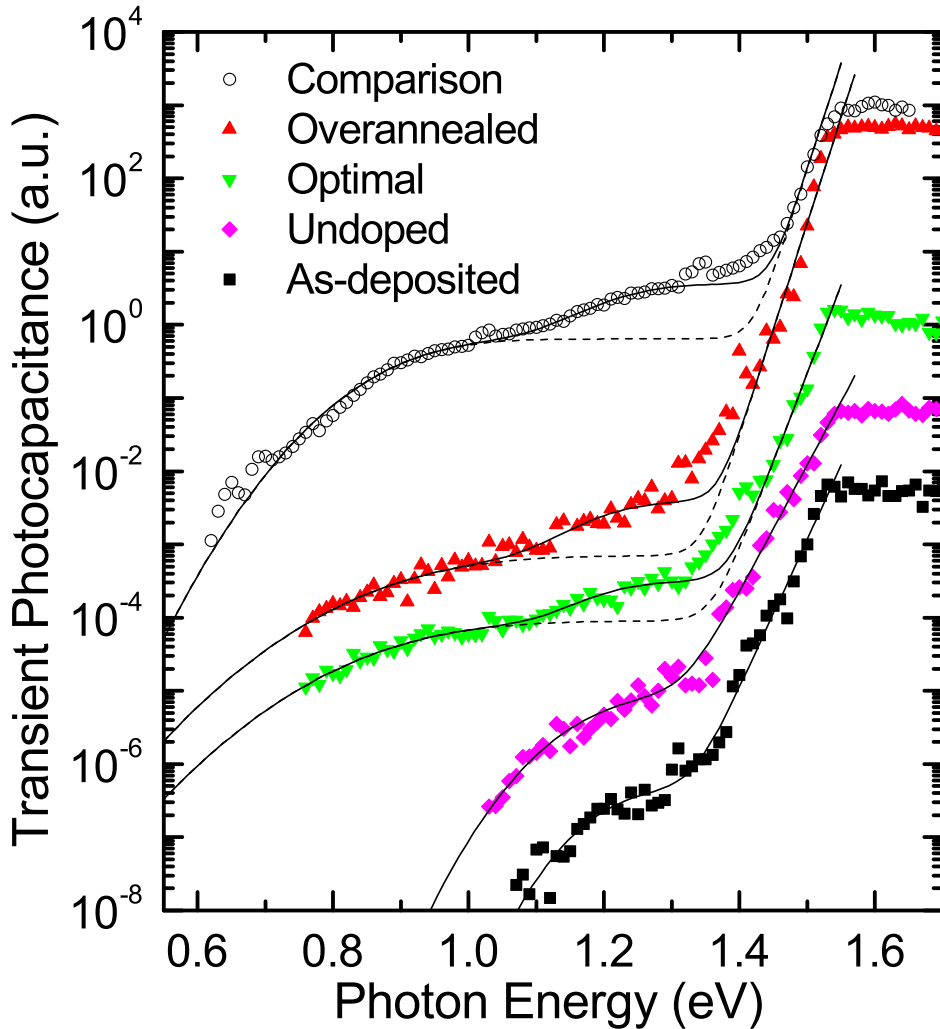
FIGURE 20. TPC spectra of the VTD devices. The spectra were collected at 160 K. Optimal (green downward triangles), overannealed (red upward triangles), and comparison (black open circles) devices have an intentionally copper-doped CdTe absorber layer, while the undoped (magenta diamonds) and as-deposited (blue squares) devices do not. Solid lines indicate the best fits to the spectra. The best fits include a Gaussian defect centered at 1.2 eV in all devices, and a 0.9 eV Gaussian defect in devices with cooper diffused into the absorber. Dashed lines are the fits with the 1.2 eV defect removed. Spectra have been offset vertically so that the individual spectra can be seen clearly.
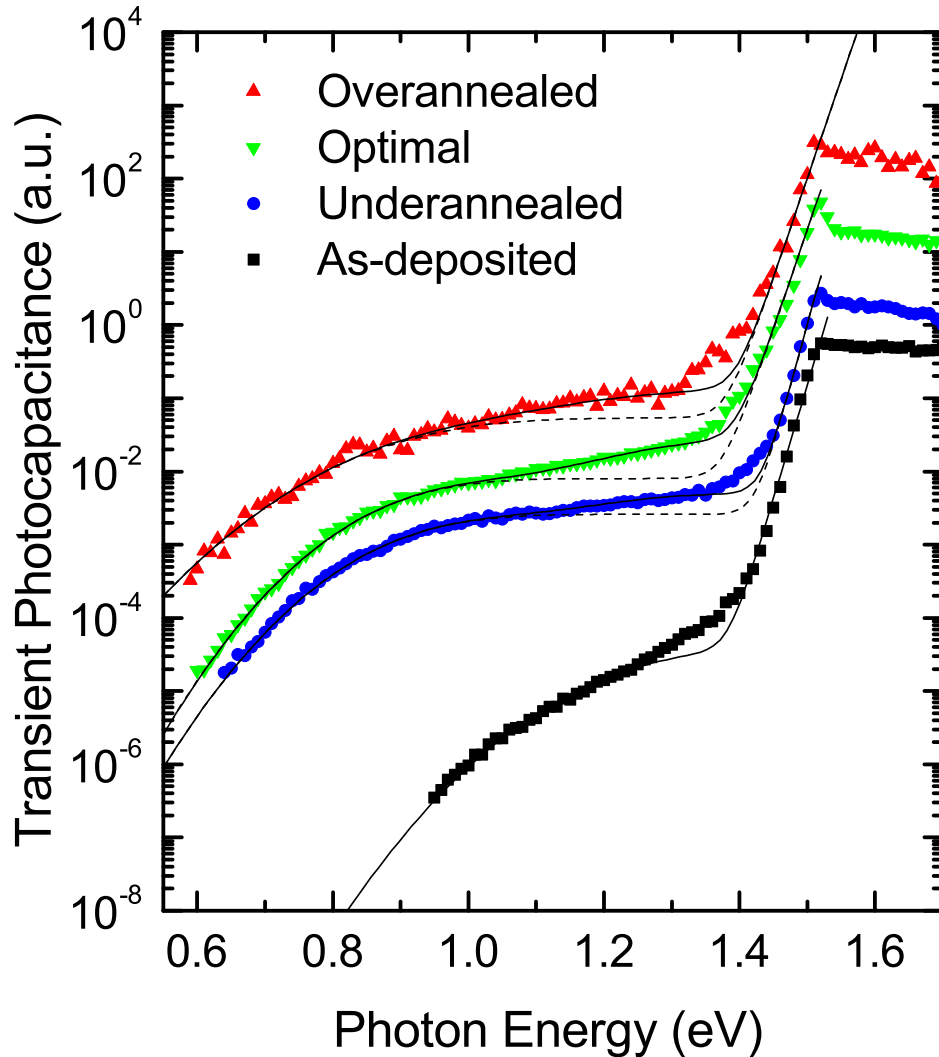
FIGURE 21. TPC spectra of the CSS devices. The spectra were collected at 200K. The optimal (green downward triangles), overannealed (red upward triangles), and underannealed (blue circles) devices have an intentionally copper-doped CdTe absorber layer, while the as-deposited device (black squares) does not. Solid lines indicate the best fits to the spectra. The best fits include a 1.2 eV defect in all devices, and a 0.9 eV defect in the devices with intentional copper diffusion into the CdTe layer. The dashed lines indicate the fits with the 1.2 eV defect removed. Spectra have been offset vertically so that the individual spectra can be seen clearly.

TABLE 2. Energetic position and full width at half maximum (FWHM) of the Gaussian defects used in the best fits to the TPC and TPI spectra (where available, fitting results for TPI spectra have been included in parentheses). The Urbach energy (E_U) of the bandtail region of the best fits are also included. The best fits were found numerically via the least squares fitting method. In all cases, fitting the spectra with a single defect was attempted before including a second defect in the scheme.

Sample	E_U (meV)	Defect 1 Energy(eV)	Defect 1 FWHM(eV)	Defect 2 Energy(eV)	Defect 2 FWHM(eV)
VTD Devices					
As-deposited	21	1.20	0.09	—	—
Undoped	25	1.18	0.11	—	—
Optimal	18	1.19	0.09	0.91	0.19
Overannealed	15	1.19	0.10	0.92	0.19
CSS Devices					
As-deposited	14(15)	1.24(1.23)	0.17(0.17)	—	—
Underannealed	13(14)	1.22(1.20)	0.13(0.12)	0.91(0.90)	0.15(0.13)
Optimal	16(16)	1.24(1.21)	0.15(0.13)	0.90(0.90)	0.15(0.19)
Overannealed	16(15)	1.19(1.23)	0.18(0.14)	0.91(0.88)	0.20(0.26)
Comparison	15	1.21	0.11	0.91	0.14
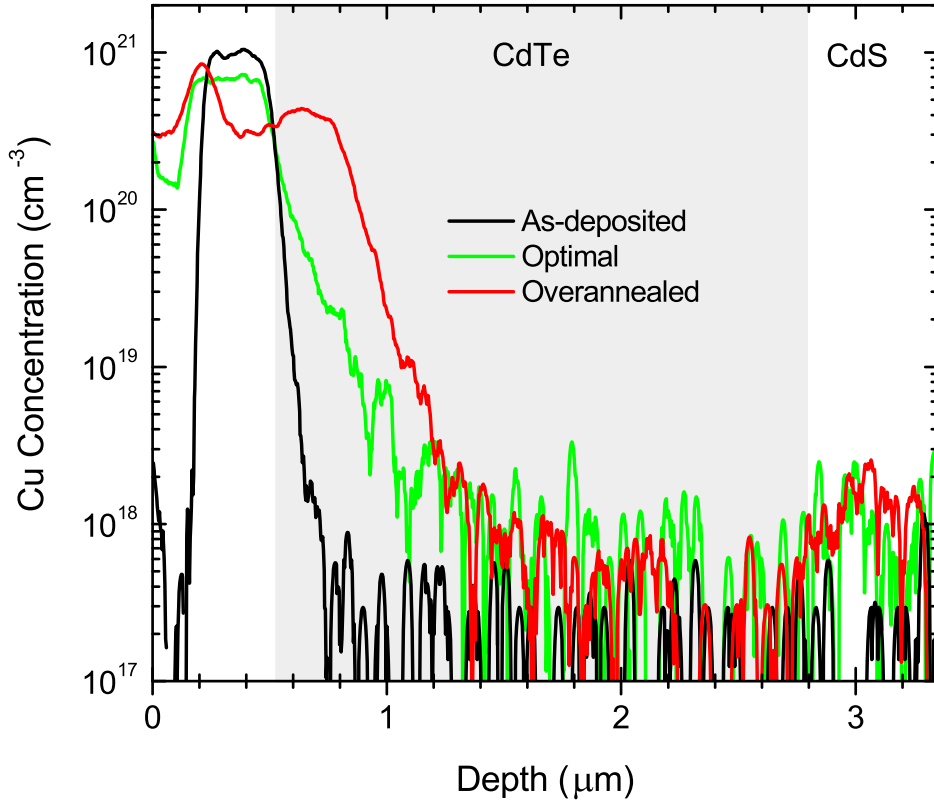
FIGURE 22. ToF-SIMS depth profiles of the VTD devices.

into the CdTe layer as the RTP treatment proceeds from underannealed, to optimal, to overannealed. This confirms that the RTP treatment is activating the copper diffusion as expected, and that the method enables the diffusion of copper into the absorber layer to be controlled.

Keeping the depth profiles in mind, consider the TPC spectra and the $0.9\,\text{eV}$ defect in particular. Note that the absence of the $0.9\,\text{eV}$ defect in the as-deposited device is not sufficient to associate the defect *exclusively* with copper. This is because other elements (e.g. zinc) are also diffusing from the ZnTe:Cu layer into the CdTe layer during the RTP treatment. Thus, it is the undoped device—compositionally identical
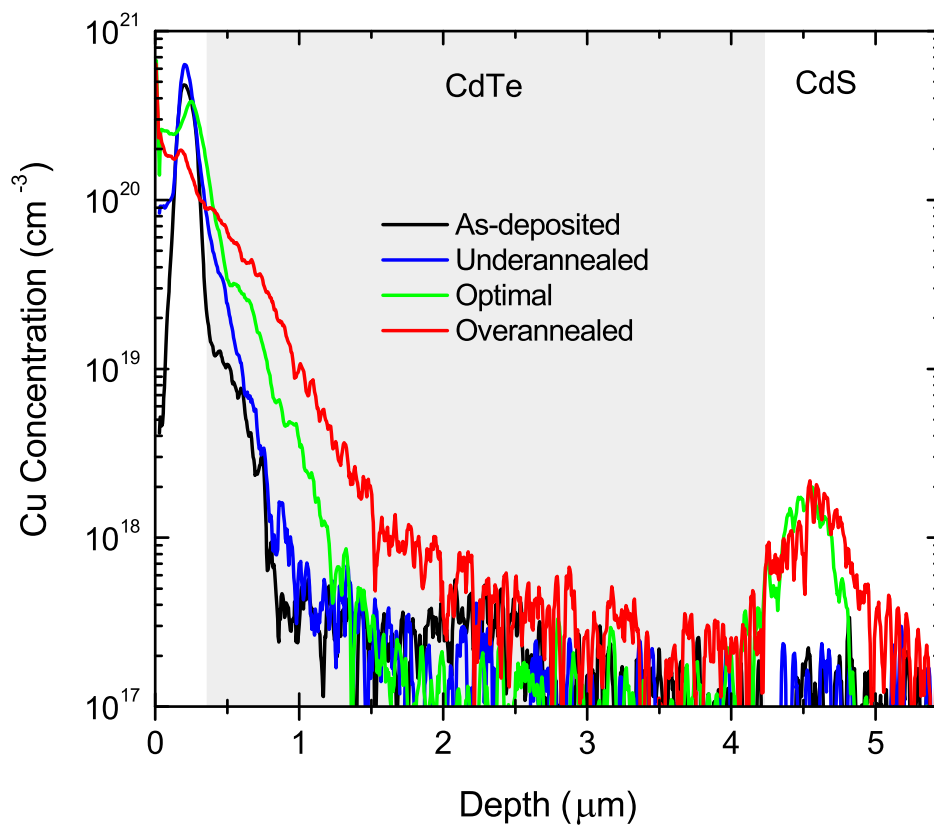
FIGURE 23. ToF-SIMS depth profiles of the CSS devices.

to the other devices except for the lack of copper doping in the ZnTe layer—that allows for copper to be exclusively associated with the presence of the $0.9\,\mathrm{eV}$ defect. Therefore, it is very important that the undoped device truly does not contain copper, i.e., that the undoped device is not *unintentionally* copper doped. Indeed, this is a reasonable concern because copper is a common impurity in tellurium feedstock [21].[1] Accordingly, to ensure that the undoped device was truly copper-free, ToF-SIMS depth profiling was performed on the undoped device. As seen in Figure 24, there is virtually no copper detected in the CdTe layer of the undoped device by ToF-SIMS, meaning that the copper concentration is several orders of magnitude smaller than in the devices with copper intentionally diffused into the CdTe layer. Thus, the exclusive association of the $0.9\,\mathrm{eV}$ defect with copper is robust.

At $0.9\,\mathrm{eV}$ above the valence band, the copper associated defect lies fairly close to mid-gap, and therefore could act as an efficient recombination center. If this were the case, one would expect the minority carrier lifetime to be reduced as the copper content of the CdTe layer increased. Indeed, the decrease in the time-resolved photoluminesence lifetime (which is essentially a measure of the minority carrier lifetime) with increasing copper content that is commonly observed in the literature [22–24] is also observed in the devices presented in this work (see J. Li et. al [66]). Thus, it is reasonable to suggest that the $0.9\,\mathrm{eV}$ defect discussed in this work is responsible for the reduction in minority carrier lifetime that has been associated with copper.

The chemical origin of the $1.2\,\mathrm{eV}$ defect could not be determined. However, it is evident that copper and zinc are not likely sources because the defect is present both before and after the RTP step. One possible candidate is the intrinsic $\mathrm{Te_{Cd}}$

---

[1]The main source of tellurium is copper anode slimes that precipitate during the electrolytic refining of copper.
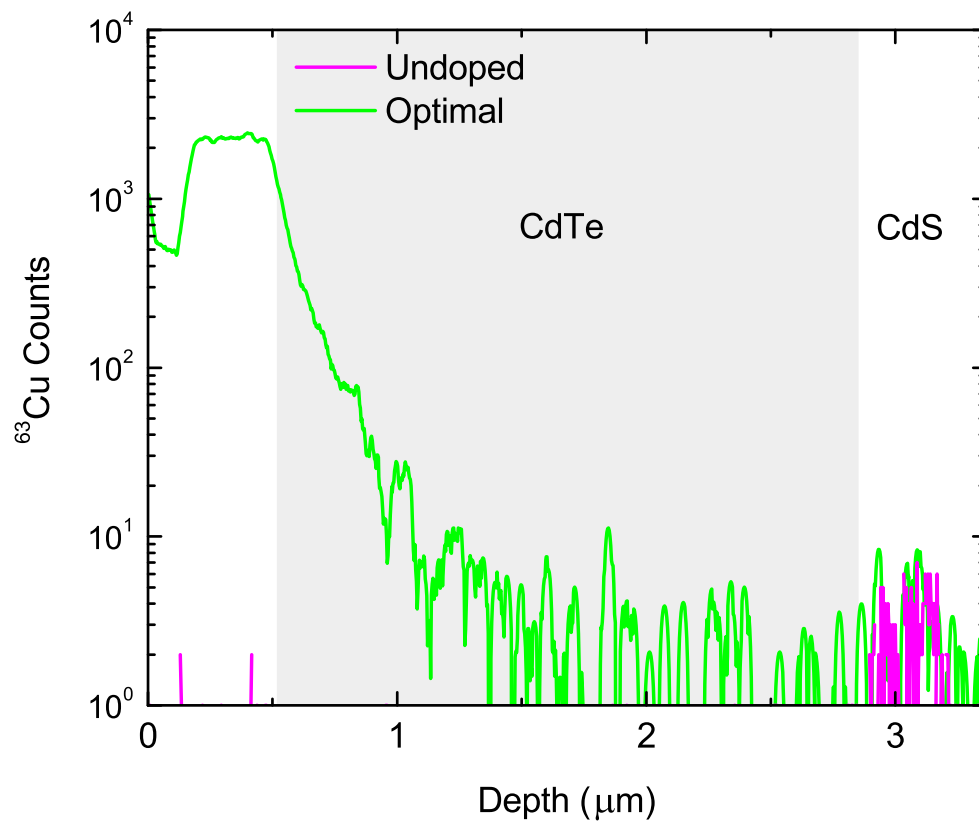
FIGURE 24. ToF-SIMS depth profile of ^{63}Cu for the undoped and optimal devices. The profile of the undoped device never registers more than one ^{63}Cu count in the CdTe layer, and exhibits as many as three orders of magnitude fewer ^{63}Cu counts when compared to the depth profile of the optimal device.

defect, which has been calculated to lie at a similar energetic position using density functional theory [14, 67].

Revisiting Figure 20, notice that the TPC spectra of the Cu_xTe contacted 'comparison' device is similar to the spectra of ZnTe:Cu contacted devices. Indeed, the TPC spectrum of the 'comparison' device is best fit with defects residing at 0.9 eV and 1.2 eV (see Table 2). This suggests that defects observed in the ZnTe:Cu contacted devices are not inherent to the back contact or RTP process itself.

Transient Photocurrent Spectroscopy

Up to this point, TPC has been used to study the presence or absence[2] of the 0.9 eV defect, as it allows for the most sensitive detection. Having established that the association of the 0.9 eV defect with copper, it is advantageous to exploit the ease with which TPI spectra can be aligned to study the dependence of the copper associated defect on copper content. As discussed in Chapter III, after the band-to-band signal in TPI is aligned, the relative magnitude of sub-bandgap TPI spectra from different samples corresponds to the relative magnitude of their actual defect densities.[3] This section will focus on the TPI spectra of only the CSS devices (shown in Figure 25). The reason for this is that the VTD devices had inferior dark current characteristics, which caused the dynamic range of the TPI measurement to be insufficient to observe the deep sub-bandgap response.

The most striking feature in Figure 25 is that the magnitude of the 1.2 eV defect response is dramatically higher in the as-deposited device. This suggests that the 1.2 eV defect is being annealed during the RTP step, although it is not clear if this

---

[2]TPC is unable to do better than this because there is no way to easily compare the magnitude of defects in spectra from different samples.

[3]Assuming that the defect cross section is not varying significantly between devices.
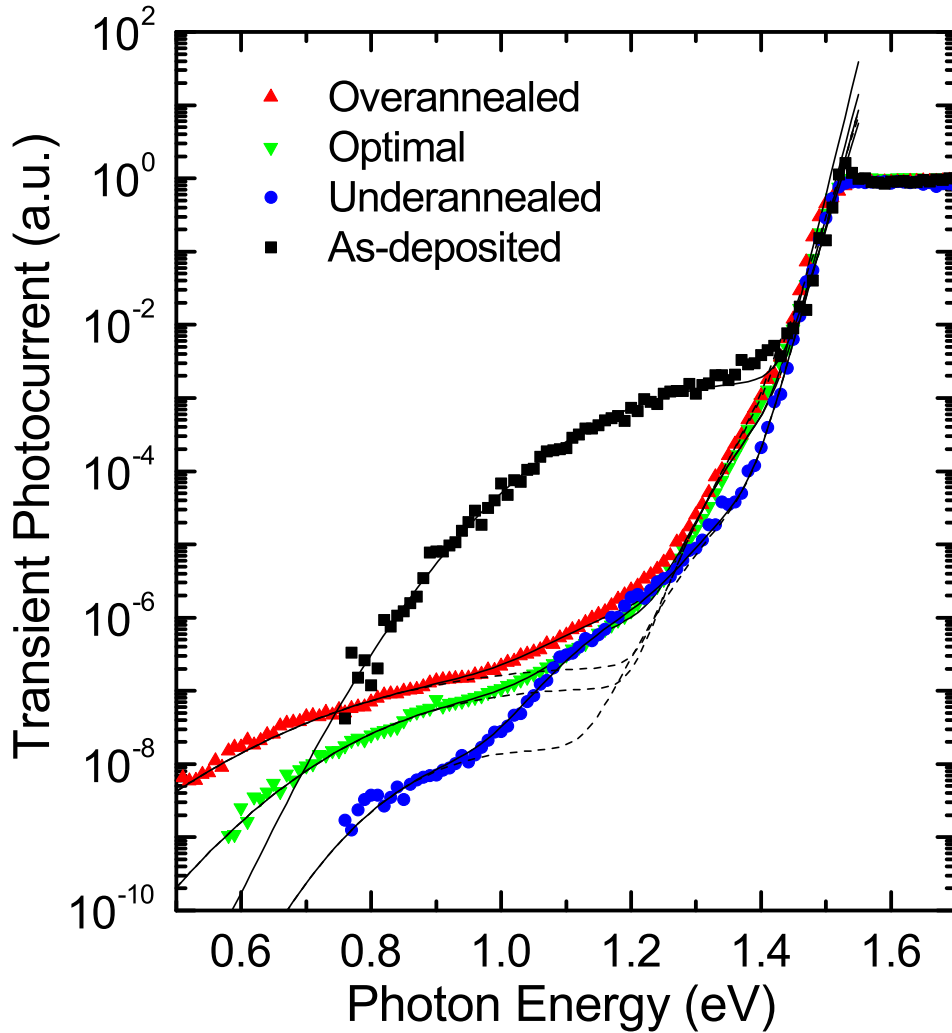
FIGURE 25. TPI spectra of the CSS devices. The spectra were collected at 200 K. Underannealed (blue circles), optimal (green downward triangles) and overannealed (red upward triangles), devices have increasing concentrations of copper in the CdTe layer, while the as-deposited device (black squares) has no copper diffused in the CdTe layer. Solid lines indicate the best fits to the spectra. The best fits include a Gaussian defect centered at 1.2 eV in all devices, and an additional Gaussian defect centered at 0.9 eV in the devices with copper in the CdTe layer. Dashed lines indicate the fits with 1.2 eV defect removed. Spectra have been vertically aligned so that the signal at the bandgap coincides.

process was independent of copper diffusing into the CdTe layer. However, as in TPC, the 1.2 eV defect is present in all the CSS devices, confirming that it is not directly associated with the presence of copper or zinc in the CdTe layer.

As in TPC, the 0.9 eV defect only appears in the TPI spectra of devices that have copper present in the CdTe layer. Furthermore, the increasing relative density of the 0.9 eV defect is concurrent with increasing amounts of copper in the CdTe layer. The correlation of the relative defect density with the quantity of copper in the CdTe layer is made more concrete by comparing the relative defect density observed in TPI with the quantity of copper in the CdTe layer observed via ToF-SIMS. The results of this comparison are shown in Figure 26. Here, the TPI defect density was calculated by integrating the Gaussian defect profile determined to be the best fit of the 0.9 eV response seen in Figure 25. The relative copper content of the CdTe layer was calculated by integrating the ToF-SIMS depth profile across the entire CdTe layer (as seen in Figure 23), which is appropriate for comparison to TPI because the depletion region extends across the CdTe layer. As shown in Figure 26, the TPI and ToF-SIMS data agree to within the uncertainty limits of the measurements. This agreement further reinforces the association of the 0.9 eV defect with the presence of Cu in the CdTe layer.

Differentiating the best fits to the TPI data gives the density of states underlying the fit. Therefore, it is possible to illustrate the density of states for each of the devices shown in Figure 25. This has been carried out in Figure 27. As can be seen, this illustrates how the 0.9 eV defect appears in the density of states of devices with copper in the CdTe layer, and that the density increases with copper content. Also illustrated is the dramatic decrease in the density of the 1.2 eV defect after the RTP treatment.
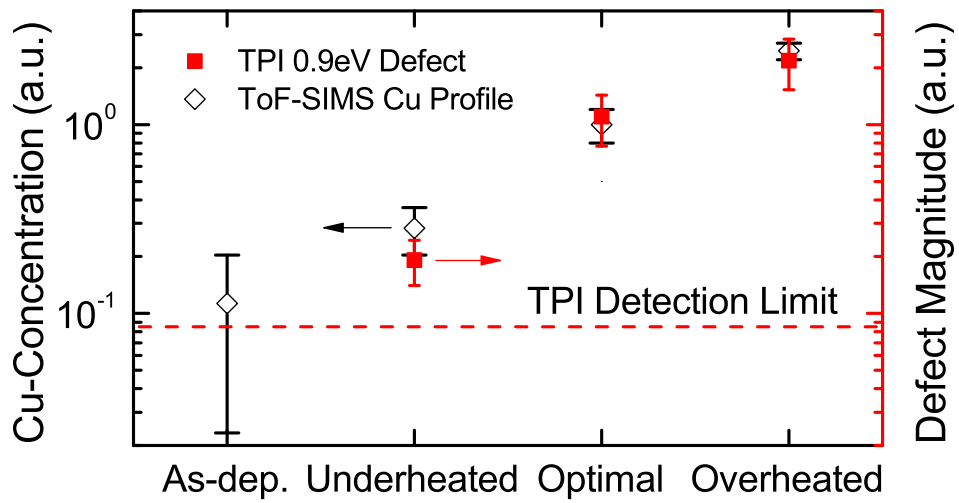
FIGURE 26. The relative variation of the quantity of copper in the CSS CdTe layers observed in ToF-SIMS compared to the relative variation of the density of the $0.9\,\text{eV}$ defect observed in TPI. There is no TPI data point for the as-deposited device, because the $0.9\,\text{eV}$ defect was not observed, in accordance with the observed TPI detection limit (dashed line) for that device.
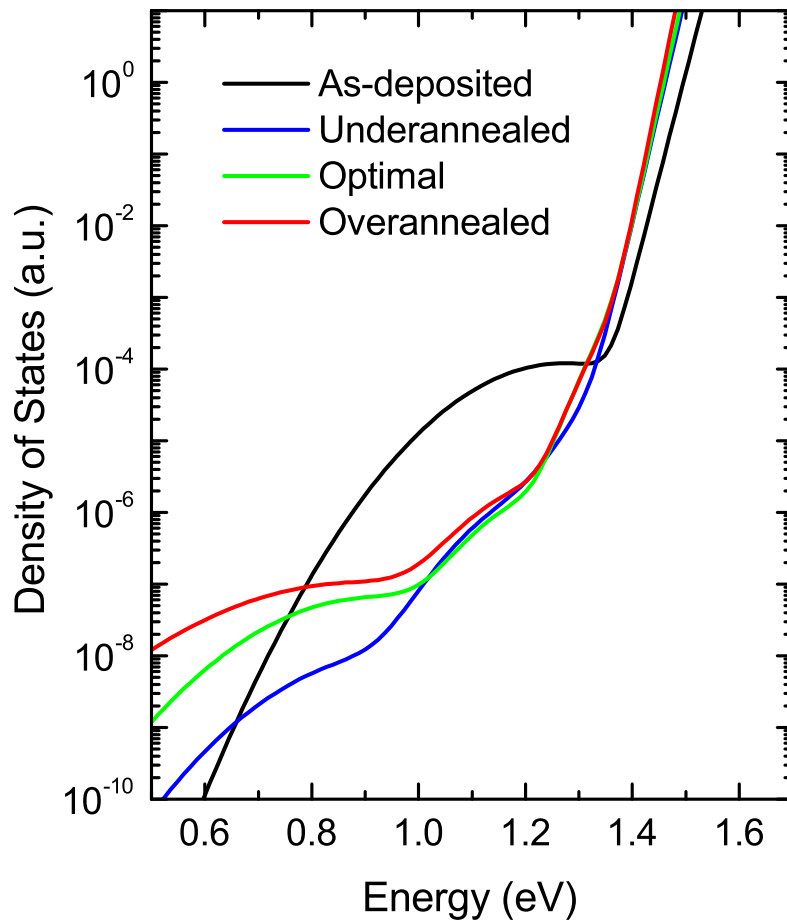
FIGURE 27. The density of states underlying the best fits to the TPI spectra of the devices fabricated by CSS. Integrating these curves gives the solid lines in Figure 25.

Numerical Modeling

The algorithm used to model the potential profile $\psi(x)$ (i.e. the band diagram) and the charge density distribution $\rho(x)$ of a one-sided $p-n$ junction is described in detail in Appendix D. An example implementation in the Python language is given in Appendix G. Fundamentally, the model allows one to calculate the potential profile and the charge density distribution from a given density of states $g(E, x)$ that is allowed to vary arbitrarily in both energy and position space (one-dimensional). The parameters required as input by the model are: the thickness and dielectric constant of lightly doped side of the junction, the density of states, the bandgap, the Fermi level, the built-in voltage, and the applied voltage.[4] For simplicity, the Fermi Dirac distribution is approximated by a step function (as in Eq. 2.12).

For a given $p-n$ junction that is being modeled, measurements can be simulated in order to calculate the characteristics of the junction. For example, the DC capacitance (the value of the capacitance measured in the low frequency limit) can be calculated by modeling the junction under two different voltage conditions (V and $V + \delta V$), and calculating the total charge ($Q = \int \rho(x)dx$) in each case. The change in total charge between the two voltage conditions (δQ) allows the DC capacitance ($C = \delta Q/\delta V$) to be calculated. More generally, the capacitance at a given temperature (T) and angular frequency (ω) can be calculated in the same way as the DC capacitance with the additional requirement that only states within a demarcation energy

$$E_e = k_B T \log \left[\frac{\omega}{\nu} \right] \tag{5.1}$$

---

[4]Where relevant, the temperature, measurement frequency, and thermal emission prefactor may also need to be specified.

of the relevant band are allowed to change their occupation in response to the change in voltage, δV. Here, ν is the thermal emission prefactor of the state, and k_B is Boltzmann's constant.

Simple measurements like capacitance can be applied to test more advanced concepts. For example, the spatial sensitivity of capacitance can be directly probed by modeling the conditions used to derive it in Chapter II. That is, one can introduce a small charge into the depletion region of a model $p - n$ junction, and calculate how the resultant change in capacitance depends on position at which the charge was placed. The result of such a procedure is plotted in Figure 28, showing excellent agreement between the spatial sensitivity of capacitance exhibited by the model and the theoretical prediction (Eq. 2.35).

More complicated measurements can be simulated as well. For TPC, this would generally involve calculating capacitance transients generated in response to voltage and illumination. At first glance, modeling such non-equilibrium processes would seem to demand very complex numerical techniques. However, for the purposes of modeling the CdTe devices appearing in this work, an assumption can be made that greatly simplifies the complexity of the modeling required. This assumption is that occupation of deep defects under illumination reaches steady-state quickly compared to the time scale of the TPC measurement (1 s). That is, the capacitance transient under illumination is identical to the dark transient except for an overall shift in capacitance ($C^{\text{light}}(t) = C^{\text{dark}}(t) + \text{constant}$). This assumption is justified because the model is intended to study the copper associated defect discussed in this work. At 0.9 eV above the valence band, this defect is so far above the Fermi level that the voltage pulse does not change the occupation of the defect (i.e. it never crosses the Fermi level). Thus, the change in occupation of the defect due to illumination is
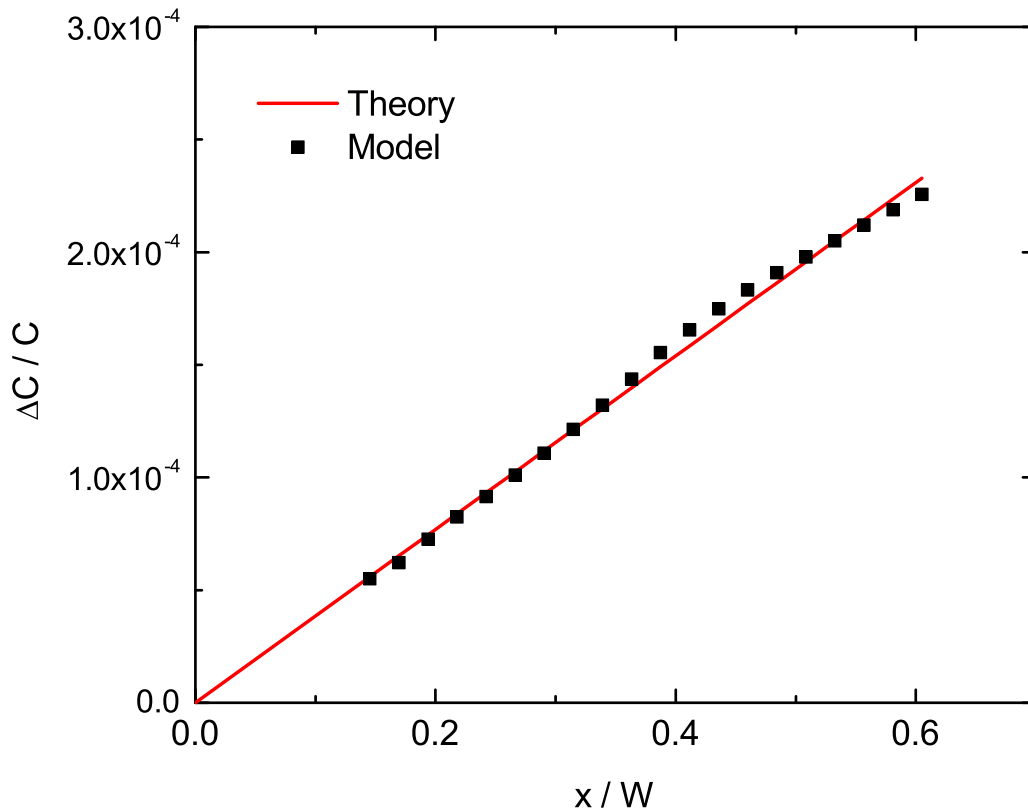
FIGURE 28. Spatial dependence of the relative change in capacitance due to charge added to the depletion region. A small charge was added to a numerically modeled $p - n$ junction at a position x/W ($x = 0$ at the junction interface, and W is the depletion width), and the resultant change in capacitance ($\Delta C/C$) was calculated (black squares). The results from the numerical model are in good agreement with the theoretical prediction (Eq. 2.35, red line). The small deviations from theory are due to the precision limitations imposed by using a discrete grid.

simply dictated by the balance of the thermal capture rate and the optical excitation rate—processes which occur on time scales much shorter than the time scale of the TPC measurement. This assumption has two important consequences. First, the capacitance under illumination can be calculated by the method described in Appendix D, except with the equation for the charge density (Eq. 2.12) modified such that

$$\rho(x) = \frac{q}{\epsilon} \int_{E_F^0 - \psi(x)}^{E_F^0} g(E, x) dE + \rho^{\text{light}}(x), \tag{5.2}$$

where $\rho^{\text{light}}(x)$ is the steady-state charge density introduced by changing the occupation of a defect due to illumination. Second, calculating the full transient behavior is not necessary, because the TPC signal can be calculated from the simple difference of the light and dark steady-state capacitance. Additionally, assuming that sub-bandgap light is uniformly absorbed throughout the depletion region, $\rho^{\text{light}}(x)$ at a given position will simply be proportional to the local density of the relevant defect.

The above simplifications also allow TPI to be easily calculated in much the same way. This is because the current (and thus the TPI signal) generated by sub-bandgap illumination is proportional to the difference between the charge generated by the illumination and the charge required to shift the depletion region (i.e. change the capacitance). Thus, one can use this simplified model to determine whether the copper concentration profiles observed in ToF-SIMS reproduce the relative variation in the defect signal that is observed in TPI. This is implicitly testing whether the TPI and ToF-SIMS data are consistent with the spatial distribution of the copper associated $0.9\,\text{eV}$ defect being the same as the spatial distribution of copper itself.

The model parameters used to calculate the TPI signal are shown in Table 3, the calculated charge density profile and band diagram are shown in Figure 29. In addition to defects at $0.9\,\text{eV}$ and $1.2\,\text{eV}$, the density of states contained an acceptor

TABLE 3. Parameters of the modeled CdTe thin film.

Parameter	Value	Reference
Thickness	$4.25\,\mu\mathrm{m}$	[17]
Dielectric Constant	10.0	[4, 68]
Bandgap	$1.5\,\mathrm{eV}$	[4]
Fermi Level	$0.3\,\mathrm{eV}$	[4, 69]
Built-in Voltage	$1.0\,\mathrm{V}$	[70]
Applied Voltage	$0.0\,\mathrm{V}$	—

level at $0.3\,\mathrm{eV}$, which yielded a doping density of $10^{14}\,\mathrm{cm}^{-3}$. The modeled TPI defect signal for the CSS devices—assuming the defect distribution is identical to the the distribution of copper seen in ToF-SIMS—is shown in Figure 30. As can be seen, assuming the distribution of the $0.9\,\mathrm{eV}$ defect is identical to the distribution of copper itself (observed via ToF-SIMS) does a reasonably good job of reproducing the relative variation of the observed TPI signal. This confirms that the association of the increased $0.9\,\mathrm{eV}$ defect density with increased copper in the CdTe layer, and suggests that the $0.9\,\mathrm{eV}$ defect has the same spatial distribution as copper itself.

It is worth noting that the observed variation in the magnitude of the $0.9\,\mathrm{eV}$ defect in TPI can be reproduced to an arbitrary precision with *any* spatial distribution provided that the overall defect density in each device is adjusted to the "correct" value. However, given that the $0.9\,\mathrm{eV}$ defect is associated with copper, it is natural to hypothesize that spatial distribution of the defect is the same as the spatial distribution of copper itself. Thus, what is being tested in Figure 30 is whether the variation in the magnitude of $0.9\,\mathrm{eV}$ seen in TPI is consistent with the known spatial distribution of copper in the devices (observed with ToF-SIMS).
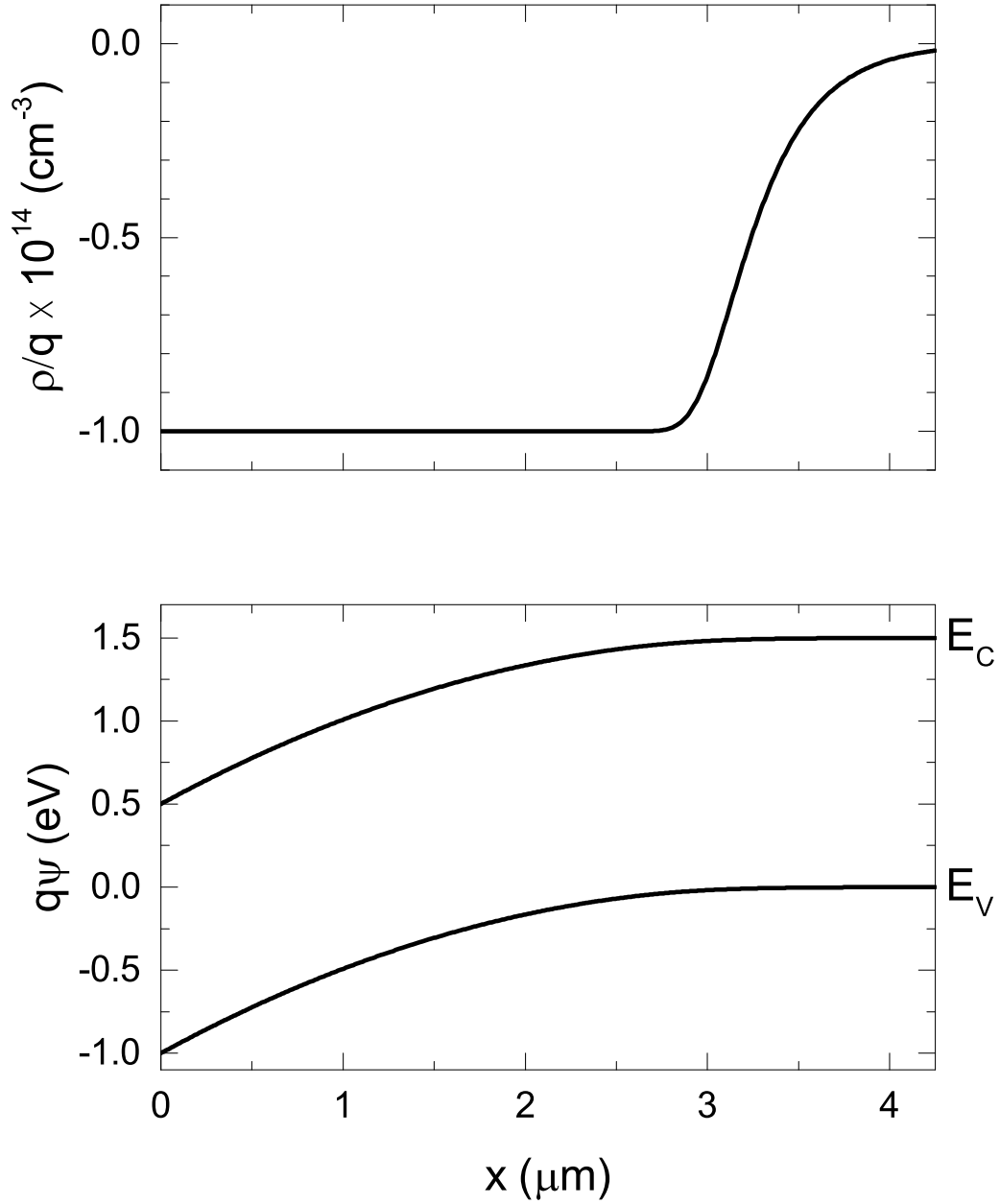
FIGURE 29. Simulated charge density (ρ/q) profile and band diagram ($q\psi$) for the parameters listed in Table 3.
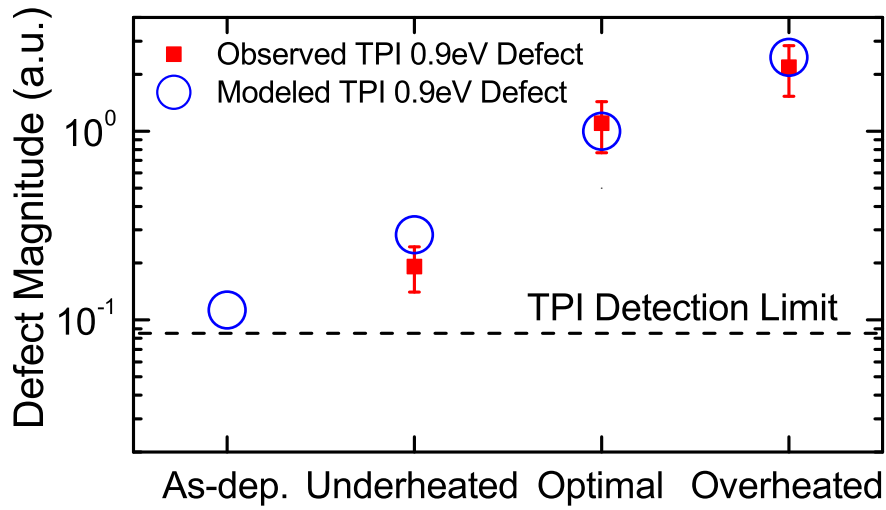
FIGURE 30. Comparison of the relative magnitude of the 0.9 eV defect observed in TPI (red squares) to the modeled relative magnitude assuming the 0.9 eV defect has the same spatial distribution as the copper observed via ToF-SIMS (blue circles).

CHAPTER VI

CONCLUSION

In this work, the TPC and TPI techniques have been used to provide a detailed picture of the defect structure in the upper-half of the bandgap of CdTe solar cells, with a focus on the effect of copper. Because they are sensitive optical measurements that can be performed on completed devices, TPC and TPI are well suited to this task [30]. Where relevant, ToF-SIMS and numerical models were used to strengthen the conclusions drawn from the TPC and TPI data.

Using TPC and TPI, two defects were identified in the CdTe devices at optical energies of $E_V+1.2\,\text{eV}$ and $E_V+0.9\,\text{eV}$. The 1.2 eV defect could not be associated with a particular element, although copper and zinc were ruled out as sources. Comparison with results from calculations using density functional theory suggest that the Te_{Cd} defect would have a similar energetic position, suggesting that this defect may be responsible for the 1.2 eV response. TPI was used to observe that the density of the 1.2 eV defect was dramatically reduced by the rapid thermal processing procedure, suggesting that the defect is annealed during the treatment. It is not clear whether or not copper plays a role in this process.

The set of samples examined used a rapid thermal processing treatment to carefully control the amount of copper that diffused into the CdTe layer from the Cu:ZnTe interfacial layer at the back of the device. By comparing devices with varying amounts of copper in the CdTe layer, the 0.9 eV defect seen in TPC was associated with the presence of copper in the absorber layer. TPI spectra confirmed the association of the 0.9 eV with copper, and showed that the magnitude of the 0.9 eV defect signal increased as more copper was diffused into the CdTe layer. A

proportional link between the density of the $0.9\,eV$ defect observed in TPI and the amount of cooper in the absorber layer observed via ToF-SIMS further established that copper is responsible for it's presence. Numerical modeling of the CdTe devices was then used to confirm that the spatial distribution of copper observed in ToF-SIMS is consistent with the relative variation of defect magnitudes observed in TPI. The fact that the copper-associated $0.9\,eV$ defect lies close to mid-gap suggests that it will act as an efficient recombination center in CdTe. Therefore, it is suggested that this work has detected the deep defect that is responsible for the decreased minority carrier lifetime that has been previously associated with the amount of copper in the CdTe layer [22–24].

Recalling that further improvements in CdTe device efficiency are limited by recombination [14], these results give credence to the suggestion that the path toward better devices will require that the density of copper in the CdTe layer be carefully controlled or that it be eliminated altogether. Eliminating copper altogether is problematic, because copper-free contacting schemes have yet to achieve the success of copper-based contacts [4]. Unfortunately, controlling where and how much copper is in the absorber is also difficult (or perhaps impossible) because copper atoms are very mobile [71], and even appear to migrate throughout the CdTe layer under the normal operating conditions of a solar cell [72]. It is unclear which avenue will prove to be successful, but this work will hopefully inform future progress.

APPENDIX A

OHM'S LAW

Following Sze [29], consider electrons inside a semiconductor at thermal equilibrium. By the equipartition theorem, the average kinetic energy of the electrons is related to the temperature such that

$$\frac{1}{2}m_n v_{th}^2 = \frac{3}{2}k_B T, \tag{A.1}$$

where m_n is the effective mass of the electrons, v_{th} is the thermal velocity of electrons, k_B is Boltzmann's constant, and T is the absolute temperature. Because thermal fluctuations are random, the thermal velocity of individual electrons will be randomly oriented, and the thermal velocity averaged over all the electrons will be zero. Since the electrons are inside a semiconductor, they will periodically collide with lattice atoms, which will randomize their thermal velocity. The average time between collisions τ_c is known as the mean free time.

If an electric field $\mathcal{E}$ is applied to the semiconductor, the electrons will experience a force $-q\mathcal{E}$, where q is the fundamental charge. During the time between collisions with the lattice atoms, the average change in the momentum of the electrons will be $-q\mathcal{E}\tau_c$. Since lattice collisions randomize the velocity of the electrons, any momentum gained by an electron due to the electric field is lost after each collision. Thus, on average, the change in momentum between collisions is exactly equal to the momentum imparted by the field

$$m_n v_n = -q\mathcal{E}\tau_c. \tag{A.2}$$

Here, v_n is the drift velocity of the electrons (the velocity due to the electric field). Reorganizing Eq. A.2 gives

$$v_n = -\frac{q\tau_c}{m_n}\mathcal{E} \equiv -\mu_n\mathcal{E}, \tag{A.3}$$

where $\mu_n \equiv q\tau_c/m_n$ is defined to be the electron mobility. Similarly for holes,

$$v_p = \frac{q\tau_c}{m_p}\mathcal{E} \equiv \mu_p\mathcal{E}. \tag{A.4}$$

If n is the density of free electrons in the semiconductor, then the electron current density J_n^{drift} due to the electric field (Ohms's law) is simply

$$J_n^{\text{drift}} = -qnv_n = qn\mu_n\mathcal{E}. \tag{A.5}$$

Likewise for holes with free carrier density p,

$$J_p^{\text{drift}} = qpv_p = qn\mu_p\mathcal{E}. \tag{A.6}$$

APPENDIX B

THE EINSTEIN RELATION

Following Sze [29], consider a semiconductor in which the density of electrons in the conduction band, $n(x)$, is non-uniform in the x-direction. Due to the finite temperature of the system, electrons will have a thermal velocity $\langle v_n \rangle$, and will travel one mean free path l between collisions with lattice atoms. In the semiconductor, the diffusion current through an arbitrary point $x = a$ during a time $\tau = l/\langle v_n \rangle$ (the mean free time) will originate from the interval $a \pm \langle v_n \rangle \tau = a \pm l$. That is, only carriers within a mean free path of the point $x = a$ will contribute to the diffusion current at that point. On average, half the electrons at $x = a \pm l$ will cross $x = a$, because they are equally likely to move in the positive or negative direction. Thus, the current originating from $x = a \pm l$ that passes through $x = a$ will be

$$J_n^{\pm} = \frac{1}{2} q \langle v_n \rangle n(a \pm l). \tag{B.1}$$

Taking into account the fact that current flow and electron flow are in opposite directions, the net diffusion current through $x = a$ will be

$$J_n^{\text{diffusion}} = J_n^+ - J_n^- = \frac{1}{2} q \langle v_n \rangle \left[n(a+l) - n(a-l) \right]. \tag{B.2}$$

To first order, this can be rewritten as

$$J_n^{\text{diffusion}} = \frac{1}{2} q \langle v_n \rangle \left[n(a) + l\frac{dn}{dx} - n(a) + l\frac{dn}{dx} \right] = q \langle v_n \rangle l \frac{dn}{dx}. \tag{B.3}$$

Defining the diffusivity as

$$D_n \equiv \langle v_n \rangle l, \tag{B.4}$$

We get that the diffusion current (Eq. B.3) becomes

$$J_n^{\text{diffusion}} = q D_n \frac{dn}{dx}. \tag{B.5}$$

A relation between the electron diffusivity and the electron mobility can be established by recognizing that the relation

$$l = \frac{\langle v_n \rangle}{\tau} \tag{B.6}$$

allows one to rewrite the mobility as

$$\mu_n \equiv \frac{q\tau}{m_n} = \frac{ql}{m_n \langle v_n \rangle}, \tag{B.7}$$

where m_n is the effective mass of electrons in the conduction band. This allows one to solve Eq. B.7 for l and substitute the result into Eq. B.4, yielding

$$D_n = \frac{m_n \mu_n \langle v_n \rangle^2}{q}. \tag{B.8}$$

Here, recall that the equipartition theorem in one dimension states that

$$\frac{1}{2} m_n \langle v_n \rangle^2 = \frac{1}{2} k_B T. \tag{B.9}$$

This allows one to solve Eq. B.9 for $\langle v_n \rangle^2$, giving

$$\langle v_n \rangle^2 = \frac{k_B T}{m_n}. \tag{B.10}$$

Substituting Eq. B.10 into Eq. B.8 gives

$$D_n = \frac{k_B T \mu_n}{q}. \tag{B.11}$$

This result (known as the Einstein relation [73]) is significant because it establishes a relation between the diffusivity and the mobility that does not depend on any other materials parameters.

APPENDIX C

THE DENSITY OF STATES IN A CRYSTAL

Following Sze [29], for free electrons the kinetic energy is

$$E = \frac{p^2}{2m}, \tag{C.1}$$

where p is the momentum and m is the mass of an electron. Conduction band electrons are approximately free, which allows their kinetic energy to be expressed in a fashion similar to Eq. C.1. Namely,

$$E = \frac{\bar{p}^2}{2m_n}, \tag{C.2}$$

where $\bar{p}$ is the crystal momentum, and m_n is the effective mass of an electron in the conduction band. To the extent that electrons in a crystal lattice can be described by a Bloch state (i.e. a plane wave multiplied by a periodic function), the crystal momentum is a well-defined quantity analogous to the momentum of a free particle. The main caveat here, is that for indirect semiconductors $E = 0$ does not necessarily require that $\bar{p} = 0$, as one would expect from the free particle analogy.

A finite semiconductor with dimensions L_x, L_y, L_z, imposes boundary conditions on the conduction band electrons indentical to those of a standard "particle-in-a-box" problem. Thus the wavefunction of the electrons must be described by standing waves such that

$$\frac{L_x}{\lambda} = n_x, \ n_x = 0, 1, 2, 3 \ldots, \tag{C.3}$$

where λ (the wavelength) is given by the de Broglie relation

$$\lambda = \frac{h}{\bar{p}_x}. \tag{C.4}$$

Combining the last two relations gives the condition

$$\bar{p}_x = \frac{hn_x}{L_x}, \tag{C.5}$$

for the x-direction. Similar relations hold for the y- and z-directions as well.

These relations allow for the calculation of the density of states in $\bar{p}$-space as follows. The volume of a spherical shell of thickness $d\bar{p}$ in $\bar{p}$-space is simply $4\pi\bar{p}^2 d\bar{p}$. From Eq. C.5, the $\bar{p}$-space volume occupied by each state is $h^3/L_x L_y L_z$. Thus, the number of states in the shell will be

$$\mathcal{N}(\bar{p})d\bar{p} = 2\frac{4\pi\bar{p}d\bar{p}}{h^3/L_x L_y L_z}, \tag{C.6}$$

where the factor of 2 is necessary to account for the Pauli exclusion principle. Using Eqs. C.2 and C.6 we can find the number of states ($\mathcal{N}$) in an energy range dE

$$\mathcal{N}(E)dE = \frac{4\pi L_x L_y L_z}{h^3}(2m_n)^{3/2}\sqrt{E}dE. \tag{C.7}$$

Dividing by the volume $L_x L_y L_z$ gives the *density* of states (N) as a function of energy

$$N(E) = \frac{4\pi}{h^3}(2m_n)^{3/2}\sqrt{E}. \tag{C.8}$$

Notice that in the perfect crystal under consideration, the density of states in the conduction has a $\sqrt{E}$ dependence, which means that

$$\frac{dN}{dE} \to \infty \ \text{ as } E \to 0, \tag{C.9}$$

i.e., the conduction band edge has an infinite slope. For amorphous materials typical of thin-film solar cells, the band edge has an exponential dependence.

Having calculated the density of states as a function of energy, it is now possible to determine the free carrier concentration in the semiconductor (i.e., the concentration of electrons in the conduction band, or holes in the valence band). The concentration of free electrons (n) is given by

$$n = \int_{E_C}^{E_{top}} N(E - E_C)F(E)dE. \tag{C.10}$$

Here, E_C is the energy of the bottom of the conduction band, E_{top} is the energy of the top of the conduction band, and $F(E)$ is the Fermi-Dirac distribution

$$F(E) = \frac{1}{1 + \exp\left[(E - E_F)/k_B T\right]}. \tag{C.11}$$

The Fermi-Dirac distribution is the probability that a state with energy E will be occupied by an electron, and the Fermi level E_F is the energy at which $F(E) = 1/2$. Note that

$$F(E) \to \exp\left[-(E - E_F)/k_B T\right] \ \text{ when } (E - E_F) \gtrsim 3k_B T. \tag{C.12}$$

Assuming $(E_C - E_F) \gtrsim 3k_BT$, substituting Eqs. C.8 and C.12 into Eq. C.10, and taking $E_{top} \to \infty$ due to the exponential suppression of $F(E)$ gives

$$n = 4\pi \left(\frac{2m_n}{h^2}\right)^{3/2} \int_{E_C}^{\infty} \sqrt{E - E_C} \exp\left[-(E - E_F)/k_BT\right] dE. \tag{C.13}$$

Defining $x \equiv (E - E_C)/k_BT$ this becomes

$$n = 4\pi \left(\frac{2m_n k_BT}{h^2}\right)^{3/2} \exp\left[-\frac{(E_C - E_F)}{k_BT}\right] \int_0^{\infty} \sqrt{x} \exp\left[-x\right] dx, \tag{C.14}$$

or

$$n = N_C \exp\left[-\frac{(E_C - E_F)}{k_BT}\right], \tag{C.15}$$

with

$$N_C \equiv 2 \left(\frac{2\pi m_n k_BT}{h^2}\right)^{3/2}. \tag{C.16}$$

Likewise, for holes

$$p = N_V \exp\left[-\frac{(E_F - E_V)}{k_BT}\right], \tag{C.17}$$

with

$$N_V \equiv 2 \left(\frac{2\pi m_p k_BT}{h^2}\right)^{3/2}. \tag{C.18}$$

In the case of intrinsic semiconductors, i.e., semiconductors in which the free carrier concentration is dominated by the thermal excitation of carriers across the bandgap[1],

$$n = p \equiv n_i. \tag{C.19}$$

---

[1]Each thermal excitation across the bandgap produces exactly one free electron and one free hole.

Combining Eq. C.19 with Eqs. C.15 and C.17 allows one to find the intrinsic fermi level

$$E_F^{\text{intrinsic}} \equiv E_i = \frac{E_g}{2} + \frac{k_B T}{2} \ln\left(\frac{N_V}{N_C}\right), \tag{C.20}$$

where $E_g = E_C - E_V$ is the bandgap. For a typical semiconductor at $300\,\text{K}$,

$$E_g/2 \gg k_B T \approx 25.85\,\text{meV},$$

thus, the rightmost term in Eq. C.20 is small, and the intrinsic Fermi level is typically very close to mid-gap.

Note that multiplying Eqs. C.15 and C.17 gives the mass action law

$$np = n_i^2 = N_C N_V \exp\left[-\frac{E_g}{k_B T}\right], \tag{C.21}$$

which evidently depends only on fundamental materials properties. This is extremely useful because it applies to both intrinsic *and* extrinsic semiconductors at thermal equilibrium.

Also worth noting is that the kinetic energy E of free electrons at the botton of the conduction band is zero. A consequence of this is that the bottom of the conduction band corresponds to the potential energy of the free electrons. Therefore, the gradient of the conduction band (or any band parallel to it) is proportional to the electric field, i.e.,

$$\mathcal{E} = \frac{1}{q}\frac{dE_C}{dx} = \frac{1}{q}\frac{dE_V}{dx} \dots \tag{C.22}$$

Notice that the derivatives lack the usual minus sign because E_C and E_V correspond to the *electron* potential energy. One consequence of this is that the force on an electron is "downhill" in band diagrams as they are typically drawn.

APPENDIX D

SOLVING POISSON'S EQUATION NUMERICALLY

Following Cohen and Lang [31], consider solving a differential eqaution of the form

$$P'' = Q \tag{D.1}$$

on a discrete grid x_n, with a regular grid spacing h. The discrete Taylor expansion of Eq. D.1 allows one to relate the value of P at x_{n+1} (denoted as P_{n+1}) to the value at a neighboring point, P_n,

$$P_{n+1} = P_n + hP'_n + \frac{h^2}{2!}P''_n + \frac{h^3}{3!}P'''_n + \frac{h^4}{4!}P''''_n + \frac{h^5}{5!}P'''''_n + \mathcal{O}(h^6). \tag{D.2}$$

Likewise, for P_{n-1}

$$P_{n-1} = P_n - hP'_n + \frac{h^2}{2!}P''_n - \frac{h^3}{3!}P'''_n + \frac{h^4}{4!}P''''_n - \frac{h^5}{5!}P'''''_n + \mathcal{O}(h^6). \tag{D.3}$$

Adding Eqs. D.2 and D.3 eliminates terms with odd numbered derivatives, yielding

$$P_{n+1} = 2P_n - P_{n-1} + h^2 P''_n + \frac{h^4}{12}P''''_n + \mathcal{O}(h^6). \tag{D.4}$$

Note that from Eq. D.1 and the finite difference approximation of the second derivative one gets that

$$P''''_n = Q''_n = \frac{Q_{n+1} - 2Q_n + Q_{n-1}}{h^2}. \tag{D.5}$$

Using Eq. D.5 and Eq. D.1, one can rewrite Eq. D.4 as

$$P_{n+1} = 2P_n - P_{n-1} + h^2 Q_n + \frac{h^2}{12}(Q_{n+1} - 2Q_n + Q_{n-1}) + \mathcal{O}(h^6). \tag{D.6}$$

The above relation allows one to calculate P_{n+1} from previous values of P (i.e., from the boundary conditions), assuming that Q is known.

For Poisson's equation in a semiconductor $P = \psi(x)$ and $Q = \rho(x)/\epsilon$. Here, $\rho(x)$ is the charge density, and $\psi(x)$ is the *electron* potential (which is why $Q \neq -\rho(x)/\epsilon$). Thus, from Eq. 2.12

$$Q = \frac{q}{\epsilon} \int_{E_F^0 - P}^{E_F^0} g(E, x) dE, \tag{D.7}$$

which is problematic because Q depends on P, and P is unknown. This can be circumvented by noticing that Eq. D.4 gives an approximation of P_{n+1} (denoted P_{n+1}^*) that does not depend on Q_{n+1}

$$P_{n+1}^* = 2P_n - P_{n-1} + h^2 Q_n + \mathcal{O}(h^4), \tag{D.8}$$

which allows one to define

$$Q_{n+1}^* = \frac{q}{\epsilon} \int_{E_F^0 - P_{n+1}^*}^{E_F^0} g(E, x) dE + \mathcal{O}(h^4). \tag{D.9}$$

Notice that Eqs. D.8 and D.9 are only accurate to fourth-order in h, whereas the original relation (Eq. D.6) was accurate to sixth-order in h. However, substituting Eq. D.9 into Eq. D.6 yields

$$P_{n+1} = 2P_n - P_{n-1} + h^2 Q_n + \frac{h^2}{12}(Q_{n+1}^* - 2Q_n + Q_{n-1}) + \mathcal{O}(h^6), \tag{D.10}$$

which recovers the sixth-order accuracy in h. This is due to the $\mathcal{O}(h^4)$ term from Eq. D.9 picking up the h^2 coefficient from Eq. D.6. Thus, Eq. D.10 provides a means to calculate P_{n+1} from P_n, P_{n-1}, Q_n, and Q_{n-1} that is accurate to sixth-order in h. Of course, one still needs P_1 and P_0 to find the solution to Poisson's equation. However, this can be dealt with by simply guessing the initial values, solving Poisson's equation, and iterating until it gives the correct potential at the interface (i.e., the shooting method [74]). Typically, a good initalialization for the potential is the case in which $g(E, x) = g = \text{constant}$, which one can solve analytically to find

$$\psi(x) = V \exp\left[-\frac{x}{x_0}\right] \tag{D.11}$$

with

$$x_0 = \left(\frac{\epsilon}{qg}\right)^{\frac{1}{2}}. \tag{D.12}$$

Here, V is the potential at the interface $(x = 0)$ with the boundary conditions

$$\psi(\infty) = \left.\frac{d\psi}{dx}\right|_\infty = \rho(\infty) = 0 \tag{D.13}$$

deep in the bulk.

APPENDIX E

CURRENT IN A $P-N$ JUNCTION

As noted at the end of Appendix C, the valance and conduction bands in a $p-n$ junction correspond to the potential. Therefore, the potential difference across a uniform $p-n$ junction (known as the built-in potential, V_{bi}) can be formulated as

$$V_{bi} = \frac{1}{q} \left. (E_F - E_V) \right|_{n-\text{side}} - \frac{1}{q} \left. (E_F - E_V) \right|_{p-\text{side}}, \tag{E.1}$$

where the quantity $E_F - E_V$ is being evaluated on both the n-side and p-side of the junction (see Figure 4) at the relevant edge of the depletion region (or, equivalently, in the neutral bulk).

On the p-side (using Eq. C.17, with p_p being the free hole density at the edge of the depletion region on the p-side),

$$\left. (E_F - E_V) \right|_{p-\text{side}} = -k_B T \ln \left[\frac{p_p}{N_V} \right]. \tag{E.2}$$

Likewise, on the n-side (using Eq. C.15, with n_n being the free electron density at the edge of the depletion region on the n-side),

$$\left. (E_C - E_F) \right|_{n-\text{side}} = -k_B T \ln \left[\frac{n_n}{N_C} \right]. \tag{E.3}$$

Notice that

$$\begin{aligned}
\left. (E_C - E_F) \right|_{n-\text{side}} &= \left. (E_C - E_V + E_V - E_F) \right|_{n-\text{side}} \\
&= E_g + \left. (E_V - E_F) \right|_{n-\text{side}},
\end{aligned} \tag{E.4}$$

where E_g is the bandgap. Thus,

$$(E_F - E_V)|_{n-\text{side}} = -(E_C - E_F)|_{n-\text{side}} + E_g$$

$$= k_B T \ln \left[\frac{n_n}{N_C}\right] + E_g, \tag{E.5}$$

and, using Eq. E.1,

$$V_{bi} = \frac{1}{q} \left(k_B T \ln \left[\frac{n_n}{N_C}\right] + E_g + k_B T \ln \left[\frac{p_p}{N_V}\right] \right). \tag{E.6}$$

From Eq. C.21,

$$E_g = -k_B T \ln \left[\frac{n_i^2}{N_C N_V}\right], \tag{E.7}$$

which allows one to simplify Eq. E.6 to give

$$V_{bi} = \frac{k_B T}{q} \ln \left[\frac{n_n p_p}{n_i^2}\right]$$

$$= \frac{k_B T}{q} \ln \left[\frac{n_n}{n_p}\right] \tag{E.8}$$

$$= \frac{k_B T}{q} \ln \left[\frac{p_p}{p_n}\right].$$

The last two equalities have used the mass action law $n_n p_n = n_p p_p = n_i^2$ (Eq. C.21), where p_n is the free hole density on the n-side, and n_p is the free electron density on the p-side. Keep in mind that p_p, p_n, n_n, and n_p are the free densities at the relevant edge of the depletion region (or, equivalently, in the neutral bulk).

From Eq. E.8, we have that

$$n_n^{eq} = n_p^{eq} \exp \left[\frac{q V_{bi}}{k_B T}\right], \tag{E.9}$$

87

and

$$p_p^{eq} = p_n^{eq} \exp\left[\frac{qV_{bi}}{k_B T}\right], \tag{E.10}$$

where the *eq* notation has been added to denote equilibrium densities (all the densities consider so far in this section have been equilibrium values, it is just convenient to *explicitly* denote this now). If potential V (with $V > 0$ for forward bias) is applied to the $p - n$ junction these become

$$\tilde{n}_n = \tilde{n}_p \exp\left[\frac{q\left(V_{bi} - V\right)}{k_B T}\right], \tag{E.11}$$

and

$$\tilde{p}_p = \tilde{p}_n \exp\left[\frac{q\left(V_{bi} - V\right)}{k_B T}\right], \tag{E.12}$$

where tildes denote non-equilibrium electron and hole densities (at the edge of the relevant depletion region) because a current is driven when $V \neq 0$. Assuming that $n_n^{eq} \gg \tilde{p}_n$ (known as low-injection, i.e. the density of minority carriers driven into the junction by the voltage is much less than the equilibrium density of majority carriers) one can make the approximation that $\tilde{n}_n \approx n_n^{eq}$. This allows one to combine Eqs. E.9 and E.11, yielding

$$\tilde{n}_p = n_p^{eq} \exp\left[\frac{qV}{k_B T}\right], \tag{E.13}$$

or

$$\tilde{n}_p - n_p^{eq} = n_p^{eq}\left(\exp\left[\frac{qV}{k_B T}\right] - 1\right). \tag{E.14}$$

Likewise, for holes,

$$\tilde{p}_n - p_n^{eq} = p_n^{eq}\left(\exp\left[\frac{qV}{k_B T}\right] - 1\right). \tag{E.15}$$

At the edge of the depletion region, $\mathcal{E} = 0$. Thus, at the steady-state and low injection, the continuity equation for electrons in the p-type layer (Eq. F.16) becomes

$$0 = D_n \frac{\partial^2 \tilde{n}(x)_p}{\partial x^2} - \frac{\tilde{n}(x)_p - n_p^{eq}}{\tau_n}, \tag{E.16}$$

with $G_L = 0$ (no illumination). Using Eq. E.14, the solution to Eq. E.16 is (assuming the edge of the depletion region in the p-type layer is x_p, and that $\tilde{n}_p(x=\infty) = n_p^{eq}$)

$$\tilde{n}(x)_p - n_p^{eq} = n_p^{eq} \left(\exp \left[\frac{qV}{k_B T} \right] - 1 \right) \exp \left[-\frac{x - x_p}{\sqrt{D_n \tau_n}} \right]. \tag{E.17}$$

Using Eq. B.5, the current at x_p is

$$J_n(x_p) = qD_n \left. \frac{d\tilde{n}_p}{dx} \right|_{x=x_p} = \frac{qD_n n_p^{eq}}{\sqrt{D_n \tau_n}} \left(\exp \left[\frac{qV}{k_B T} \right] - 1 \right). \tag{E.18}$$

Likewise, at the depletion edge in the n-type layer $(x = -x_n)$,

$$J_p(-x_n) = -qD_p \left. \frac{d\tilde{p}_n}{dx} \right|_{x=-x_n} = \frac{qD_p p_n^{eq}}{\sqrt{D_p \tau_p}} \left(\exp \left[\frac{qV}{k_B T} \right] - 1 \right). \tag{E.19}$$

If one assumes the generation and recombination inside the depletion region is negligible, the electron and hole currents will be constant throughout the depletion region. Therefore, $J_n(x_p) = J_n(-x_n)$ and $J_p(x_p) = J_p(-x_n)$, which allows one to calculate the total current in the device by adding Eqs. E.18 and E.19 (in steady-state the total current is constant throughout the device), yielding the ideal diode equation

$$J(V) = J_p(-x_n) + J_n(-x_n) = J_p(x_p) + J_n(x_p) \equiv J_s \left(\exp \left[\frac{qV}{k_B T} \right] - 1 \right). \tag{E.20}$$

Here,

$$J_s \equiv \frac{qD_p p_n^{eq}}{\sqrt{D_p \tau_p}} + \frac{qD_n n_p^{eq}}{\sqrt{D_n \tau_n}}, \qquad (\text{E.21})$$

is the saturation current.

Following Sze [29], consider a slab of semiconductor shown in Figure 31. In a slice located at x with an infinitesimal width dx, and cross sectional area A, the total number of free electrons $N(x,t)$ will be

$$N(x,t) = n(x,t)Adx, \tag{F.1}$$

where $n(x,t)$ is the free electron density. If there is a current flowing in the semiconductor, the rate of change of the total number of free electrons in the slice will be proportional the difference between the current entering and leaving the slice

$$\frac{\partial N(x,t)}{\partial t} = \frac{\partial n(x,t)}{\partial t}Adx = -\frac{A}{q}\left[J_n(x,t) - J_n(x+dx,t)\right], \tag{F.2}$$

where J_n is the current density of electrons, and the factor of $-1/q$ converts the *charge* current ($J_n A$) to a *number* current. In general, electrons can also be generated in the slice at a rate $G_n(x,t)$ (e.g. by optical creation of electron-hole pairs) and can recombine with holes in the slice at a rate $R_n(x,t)$. Thus, the full version of Eq. F.2 will be

$$\frac{\partial n(x,t)}{\partial t}Adx = -\frac{A}{q}\left[J_n(x,t) - J_n(x+dx,t)\right] + \left(G_n(x,t) - R_n(x,t)\right)Adx. \tag{F.3}$$

Taylor expansion gives that

$$J_n(x+dx,t) = J_n(x,t) + \frac{\partial J_n(x,t)}{\partial x}dx + \dots, \tag{F.4}$$
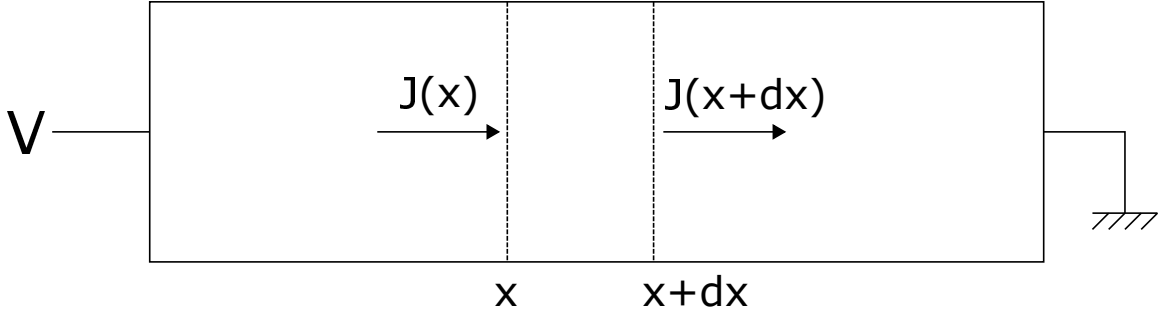
FIGURE 31. A slab of semiconductor with current flowing through a slice located at x.

which allows one to simplify Eq. F.3 to get the continuity equation

$$\frac{\partial n(x,t)}{\partial t} = \frac{1}{q}\frac{\partial J_n(x,t)}{\partial x} + G_n(x,t) - R_n(x,t). \tag{F.5}$$

Similarly for holes,

$$\frac{\partial p(x,t)}{\partial t} = -\frac{1}{q}\frac{\partial J_p(x,t)}{\partial x} + G_p(x,t) - R_p(x,t). \tag{F.6}$$

Using the equations for drift and diffusion currents (Eqs. 2.2 and 2.3) and the product rule, these equations become

$$\frac{\partial n(x,t)}{\partial t} = n(x,t)\mu_n\frac{\partial \mathcal{E}(x,t)}{\partial x} + \mu_n\mathcal{E}(x,t)\frac{\partial n(x,t)}{\partial x}$$
$$+ D_n\frac{\partial^2 n(x,t)}{\partial x^2} + G_n(x,t) - R_n(x,t), \tag{F.7}$$

and

$$\frac{\partial p(x,t)}{\partial t} = -p(x,t)\mu_p\frac{\partial \mathcal{E}(x,t)}{\partial x} - \mu_p\mathcal{E}(x,t)\frac{\partial p(x,t)}{\partial x}$$
$$+ D_p\frac{\partial^2 p(x,t)}{\partial x^2} + G_p(x,t) - R_p(x,t), \tag{F.8}$$

where μ is the mobility, $\mathcal{E}$ is the electric field, and D is the diffusivity.

92

In general, carriers are generated by optical excitation at a rate G_L and by thermal excitation G_{th}. The recombination rate, R, will be proportional to the number of free electrons and holes available to recombine. Thus,

$$R(x,t) = \beta n(x,t)p(x,t), \tag{F.9}$$

where β is a proportionality constant. At thermal equilibrium, thermal generation and recombination exactly balance, therefore

$$G_{th} = R_{th} = \beta n^{eq}p^{eq}, \tag{F.10}$$

where n^{eq} and p^{eq} are the equilibrium densities. It is convenient to define the net recombination rate

$$
\begin{aligned}
U(x,t) \equiv R(x,t) - G_{th} &= \beta n(x,t)p(x,t) - \beta n^{eq}p^{eq} \\
&= \beta\left[(n^{eq} + \Delta n(x,t))(p^{eq} + \Delta p(x,t))\right] - \beta n^{eq}p^{eq} \qquad \text{(F.11)} \\
&\approx \beta\left[n^{eq}\Delta p(x,t) + p^{eq}\Delta n(x,t)\right],
\end{aligned}
$$

where the approximate equality has assumed $\Delta p(x,t) = p_n(x,t) - p_n^{eq}$ and $\Delta n(x,t) = n_p(x,t) - n_p^{eq}$ are small compared to the equilibrium values (low injection). In an n-type semiconductor, $p_n^{eq} \ll n_n^{eq}$ and U becomes

$$
\begin{aligned}
U_n(x,t) &\approx \beta n_n^{eq}\Delta p_n(x,t) \\
&= \beta n_n^{eq}\left[p_n(x,t) - p_n^{eq}\right] \qquad\qquad \text{(F.12)} \\
&\equiv \frac{p_n(x,t) - p_n^{eq}}{\tau_p},
\end{aligned}
$$

where $\tau_p \equiv 1/\beta n_n^{eq}$ is referred to as the lifetime of minority carriers. Likewise for a p-type semiconductor,

$$U_p(x,t) = \frac{n_p(x,t) - n_p^{eq}}{\tau_n}. \tag{F.13}$$

Notice that the net recombination rate is determined by the excess *minority* carrier concentration. This makes sense because the minority carriers will always be less prevalent, and therefore serve to limit the net recombination rate.

Often the continuity equations will be rewritten in terms of U, e.g.,

$$
\begin{aligned}
\frac{\partial n(x,t)}{\partial t} = {}& n(x,t)\mu_n \frac{\partial \mathcal{E}(x,t)}{\partial x} + \mu_n \mathcal{E}(x,t)\frac{\partial n(x,t)}{\partial x} \\
& + D_n \frac{\partial^2 n(x,t)}{\partial x^2} + G_L(x,t) - U(x,t),
\end{aligned} \tag{F.14}
$$

and

$$
\begin{aligned}
\frac{\partial p(x,t)}{\partial t} = {}& -p(x,t)\mu_p \frac{\partial \mathcal{E}(x,t)}{\partial x} - \mu_p \mathcal{E}(x,t)\frac{\partial p(x,t)}{\partial x} \\
& + D_p \frac{\partial^2 p(x,t)}{\partial x^2} + G_L(x,t) - U(x,t).
\end{aligned} \tag{F.15}
$$

Or, for minority carriers under low injection conditions,

$$
\begin{aligned}
\frac{\partial n_p(x,t)}{\partial t} = {}& n_p(x,t)\mu_n \frac{\partial \mathcal{E}(x,t)}{\partial x} + \mu_n \mathcal{E}(x,t)\frac{\partial n_p(x,t)}{\partial x} \\
& + D_n \frac{\partial^2 n_p(x,t)}{\partial x^2} + G_L(x,t) - \frac{n_p(x,t) - n_p^{eq}}{\tau_n},
\end{aligned} \tag{F.16}
$$

and

$$
\begin{aligned}
\frac{\partial p_n(x,t)}{\partial t} = {}& -p_n(x,t)\mu_p \frac{\partial \mathcal{E}(x,t)}{\partial x} - \mu_p \mathcal{E}(x,t)\frac{\partial p_n(x,t)}{\partial x} \\
& + D_p \frac{\partial^2 p_n(x,t)}{\partial x^2} + G_L(x,t) - \frac{p_n(x,t) - p_n^{eq}}{\tau_p}.
\end{aligned} \tag{F.17}
$$

EXAMPLE PROGRAM

```python
##This is dcsolver.py
##Written by Charles Warren


##Import packages
import numpy as np
import matplotlib.pyplot as plt


##─────────────────────────────────────────────
##NOTE:
##Throughout, I'll refer to "the Cohen paper" that this code
##is based on. This refers to: J. D. Cohen and D. V. Lang,
##Phys. Rev. B 8, 5321 (1982). Read the Cohen paper if you
##want to understand what I've done.
##─────────────────────────────────────────────


##BEGINNING OF FUNCTIONS


##─────────────────────────────────────────────
##Calculates the next potential value using the modified
##noumerov method described in the Cohen paper.
##Everything is in SI units except for g, which is in m^−3
##eV^−1. All this does is make it so the integral to
```

```python
##calculate rho from g doesn't have the normal factor of q.
def noumerovstep(curP,prevP,nextQ,curQ,prevQ,stepsize):

    nextP = 2.0 * curP - prevP + stepsize**2.0 *\
            curQ + ( stepsize**2.0 / 12.0 ) *\
            ( nextQ + prevQ - 2.0 * curQ )


    return nextP
##----------------------------------------------------------------


##----------------------------------------------------------------
##Calculates the entire potenial and charge profile using
##the noumerov method described in the Cohen paper. Note
##that when I use rho in this section of the code, I always
##include a factor of q/eps. This is because the Poisson's
##equation is P'' = Q = q*rho/eps. You need to include the q
##because P is an energy not a voltage.
def noumerovsolve(phi,rho):

    global N, x, dx, E, Eg, Ef0, rhotable

    ##Start with a flat fermi level
    Ef = Ef0 * np.ones([N])

    for i in range(1,N-1):
```

```python
        ##Calculate the next phi approximately
        phi[i+1] = 2.0 * phi[i] - phi[i-1] +\
                   dx**2.0 * q * rho[i] / eps


        ##Enforce the deep depletion fermi level
        if ( phi[i+1] - Ef[i+1] > Eg/2 ):
            Ef[i+1] = phi[i+1] - Eg/2


        ##calculate the next rho based on the approx. phi
        rho[i+1] = calcrho(Ef[i+1]-phi[i+1],
                           i+1,Etable,rhotable)


        ##calculate the next phi based on the approx. rho
        ##note that the we need to pass rho/eps here b/c the
        ##differential equation is P'' = Q = rho/eps
        phi[i+1] = noumerovstep(phi[i],phi[i-1],
                                q*rho[i+1]/eps,q*rho[i]/eps,
                                q*rho[i-1]/eps,dx)


    ##need to return Ef becuase it could change due to the
    ##deep depletion condition
    return phi, rho, Ef
##————————————————————————————————————————————————————————————
```

97

```python
##------------------------------------------------------------
##This function is the same as noumerovsolve, except it
##accounts for AC by including a demarcation position, xe.
##Assumes that phi is the DC solution.
def noumerovsolve_ac(phi,rho):

    global N, x, dx, Ee, E, Eg, Ef0, rhotable, rhodc

    Ef = Ef0 * np.ones([N]) ##Start with a flat fermi level

    for i in range(1,N-1):

        ##Calculate the next phi approximately
        phi[i+1] = 2.0 * phi[i] - phi[i-1] +\
                   dx**2.0 * q * rho[i] / eps

        ##Enforce the deep depletion fermi level
        if ( phi[i+1] - Ef[i+1] > Eg/2 ):
            Ef[i+1] = phi[i+1] - Eg/2

        ##calculate the next rho based on the approximate
        ##phi region where everything can respond
        if ( phi[i+1] < Ef[i+1] + Ee ):
            rho[i+1] = calcrho(Ef[i+1]-phi[i+1],i+1,
                               Etable,rhotable)
```

```python
        ##emission limited region
        elif ( phidc[i+1] < Ef[i+1] + Ee ):
            rho[i+1] = calcrho(-Ee,i+1,Etable,rhotable)
        ##region where nothing can respond
        else:
            rho[i+1] = rhodc[i+1]


        ##calculate the next phi based on the approximate
        ##rho note that the we need to pass rho/eps here b/c
        ##the differential equation is P'' = Q = rho/eps
        phi[i+1] = noumerovstep(phi[i],phi[i-1],
                                q*rho[i+1]/eps,q*rho[i]/eps,
                                q*rho[i-1]/eps,dx)


    ##need to return Ef becuase it change due to the deep
    ##depletion condition
    return phi, rho, Ef
##————————————————————————————————————————————————————————————


##————————————————————————————————————————————————————————————
##When we are solving poisson's equation, we are constantly
##integrating over the density of states. This function
##precalcuates those integrals efficiently, and stores them
##in a table so they can be accessed as needed.
def rhotable():
```

```python
global q, Eg, Ef0
global g, N, M, E

##Define the range of energies over which the integrals
##will be done.
Etable = np.linspace(Ef0,-Eg/2,M)

##Define the energy step size
dEtable = Etable[0] - Etable[1]

##initialize the integral table
rhotable = np.zeros([N,M])

##calculate all the integrals
##this can be done efficiently by taking advantage of
##the fact that integral of f(F) from
##E1 to E2+dE = integral of f(E) from E1 to
##E2 + f(E2+dE) * dE j loops over the position in x,
##i loops over the position in E
for j in range(N):

    for i in range(1,M):

        rhotable[j][i] = rhotable[j][i-1] +\
```

```python
                              np.interp(Etable[i],E,g[j]) *\
                              dEtable


    ##reverse the table multiply by the fundamental charge
    ##the only reason to reverse it is so we can use
    ##np.interp later rhotable = q*np.fliplr(rhotable)
    rhotable = np.fliplr(rhotable)


    return Etable[::-1], rhotable
##——————————————————————————————————————————————————————


##——————————————————————————————————————————————————————
##calculate the rho integral from the precalculated rhotable
##the i index refers to the position as in x[i]
def calcrho(phi,i,Etable,rhotable):

    ##extracharge from, e.g., illumination
    global extracharge

    ##linear interpolate on the array of precalculated
    ##integrals, add any extra charge
    return np.interp(phi,Etable,rhotable[i])+extracharge[i]
##——————————————————————————————————————————————————————


##——————————————————————————————————————————————————————
```

```python
##Define the density of states, g
def calcg():

    global N, M, Ef0, q, x, thickness

    g = np.zeros([N,M]) ##initialize g
    ##add defects
    Ed1 = -Ef0
    defect1 = 3.25e1 * gaussian(E,-Ed1,30e-3*q/2.3548)

    ##Fill the defect array, adding spatial variations
    ##if desired
    for i in range(N):
        g[i] += defect1 ##* ( 2.0 - x[i] / thickness )

    return g
##————————————————————————————————————————————————————


##————————————————————————————————————————————————————
##Generates a gaussian array (useful for defining Gaussian
##defect profiles
def gaussian(x,mu,sigma):

    return np.exp(-( x - mu )**2.0 / ( 2.0 * sigma**2.0 ))/\
            ( np.sqrt(2.0*np.pi) * sigma )
```

```python
##———————————————————————————————————————————

##———————————————————————————————————————————
##Brackets the target voltage of the solution so that it can
##be found using the bisection method.
def bracket(phi,rho,Ef,V,verbose=False,ac=False):

    global Etable, rhotable
    global dx,q,thickness,E,Eg,Ef0,g

    if(verbose): print 'Bracketing solution...'

    ##start off by guessing exponential bands
    x0 = calcx0()
    phi[0] = q * V * np.exp( - thickness / x0 )
    phi[1] = phi[0] * np.exp( dx / x0 )
    rho[0] = calcrho(Ef[0]-phi[0],0,Etable,rhotable)
    rho[1] = calcrho(Ef[1]-phi[1],1,Etable,rhotable)
    if (ac): phi, rho, Ef = noumerovsolve_ac(phi,rho)
    else: phi, rho, Ef = noumerovsolve(phi,rho)

    if ( phi[-1]/q < V ):
        ##If we are starting low, we will bump up lo
        ##until we exceed that target voltage (and thus
        ##bracket it).
```

```python
        while ( phi[-1]/q < V ):
            lo = phi[0]
            ##double the initial phi
            phi[0] = 2 * phi[0]
            ##calculate the next phi based on exponential
            ##bands
            phi[1] = phi[0] * np.exp( dx / x0 )
            ##calculate the initial rhos based on the phis
            rho[0] = calcrho(Ef[0]-phi[0],0,Etable,rhotable)
            rho[1] = calcrho(Ef[1]-phi[1],1,Etable,rhotable)
            ##solve poisson's equation based on the
            ##initialzation
            if (ac): phi,rho,Ef = noumerovsolve_ac(phi,rho)
            else: phi, rho, Ef = noumerovsolve(phi,rho)
            if (verbose): print lo/q,phi[0]/q,phi[-1]/q,V
        hi = 2*phi[0]
    else:
        while ( phi[-1]/q > V ):
            hi = phi[0]
            ##halve the initial phi
            phi[0] = 0.5 * phi[0]
            ##calculate the next phi based on exponential
            ##bands
            phi[1] = phi[0] * np.exp( dx / x0 )
            ##calculate the initial rhos based on the phis
```

```python
            rho[0] = calcrho(Ef[0]-phi[0],0,Etable,rhotable)

            rho[1] = calcrho(Ef[1]-phi[1],1,Etable,rhotable)

            ##solve poisson's equation based on the

            ##initialzation

            if (ac): phi,rho,Ef = noumerovsolve_ac(phi,rho)

            else: phi, rho, Ef = noumerovsolve(phi,rho)

            print hi/q,phi[0]/q,phi[-1]/q,V

        lo = phi[0]


    if(verbose): print 'Done.'


    ##If the device is too thick, phi[0] will be so small
    ##that double precision won't be good enough. Making the
    ##device thinner solves this problem.
    if(phi[0]<2e-36): print'Warning: Device is too thick.'+\
        ' This could affect the convergence of the model.'


    return phi, rho, Ef, hi, lo
##--------------------------------------------------------------


##--------------------------------------------------------------
##Solve for the correct phi, rho given that the correct
##initial value of phi is bracketed by hi,lo.
##Uses the bisection method.
def solve(phi,rho,Ef,hi,lo,V,verbose=False,ac=False):
```

```python
global Etable, rhotable
global eps, q, dx, Ef0, g


x0 = calcx0()


k=1
tol = 1e-6
if(verbose):
    print 'Finding solution...'
    print ' i      V      Error   Tolerance'
    print '—————————————————————————————————————————————'
##loop until tolerance condition is met
while ( abs( phi[-1]/q - V ) > tol ):
    ##try a phi[0] in the middle of hi,lo
    phi[0] = ( hi + lo ) / 2.0
    ##calculate the rest of the initial conditions
    phi[1] = phi[0] * np.exp( dx / x0 )
    rho[0] = calcrho(Ef[0]-phi[0],0,Etable,rhotable)
    rho[1] = calcrho(Ef[1]-phi[1],1,Etable,rhotable)
    ##solve poisson's equation
    if (ac): phi, rho, Ef = noumerovsolve_ac(phi,rho)
    else: phi, rho, Ef = noumerovsolve(phi,rho)
    if(verbose): print '%2d %1.6f %1.6f %1.6f' %\
                (k, phi[-1]/q,
```

```python
                            abs( phi[-1]/q - V ), tol)
        ##stop trying to solve if hi and lo are the same
        if ( str(hi) == str(lo) ): break
        ##redefine hi,lo based on whether the result was
        ##too high or too low
        if ( phi[-1]/q > V ):
            hi = phi[0]
        else:
            lo = phi[0]
        k += 1
    if(verbose): print 'Done.'


    return phi, rho, Ef
##----------------------------------------------------------------


##----------------------------------------------------------------
def calcx0():

    global eps, q, Ef0, E, g

    return np.sqrt( eps / ( q * np.interp(Ef0,E,g[0]) ) )
##----------------------------------------------------------------


##END OF FUNCTIONS
```

```python
##Define parameters of the model
##number of points in position space
N = 500
##number of points in energy space
M = 1000
##everything is in SI units
q = 1.602176487e-19
kB = 1.3806488e-23
eps0 = 8.854187817e-12
eps = 10.0 * eps0
thickness = 4.25e-6
Eg = 1.5 * q
Ef0 = -300e-3 * q
Vbi = 1.0
Vapp = 0.0


T = 200. ## K
freq = 1e3 ## Hz
nu0 = 1e12 ## Hz
dV = -0.01 ## V


##leave extracharge as zero for now
extracharge = np.zeros([N])


##calculate some extra parameters
```

```python
V = Vbi - Vapp

x = np.linspace(0,thickness,N)

dx = x[1] - x[0]

E = np.linspace(-2,0,M) * q

g = calcg()


print 'Precalculating integrals over the'+\
        ' density of states...'


## rhoxtable() precalculates the integral over the density
## of states as a function of phi (Etable) and x. The
## integral is eq. 3 from the Cohen paper, with g allowed to
## vary with x. Having this integral precalculated saves
## time that would be wasted calculating the same integral
## over and over a again. It also saves time in that it
## efficiently calculates all of the integrals over energy
## (for a given position) in one loop.

## Etable and rhoxtable are global variables that can be
## used in all the functions.
Etable, rhotable = rhotable()


print 'Done.'


## Initialize our arrays
```

```python
phi = np.zeros([N])
rho = np.zeros([N])
Ef = Ef0 * np.ones([N])


## Calculate the DC band bending, charge profile, and
## electric field
phi, rho, Ef, hi, lo = bracket(phi,rho,Ef,V,verbose=True)
phi, rho, Ef = solve(phi,rho,Ef,hi,lo,V,verbose=True)
F = np.gradient(phi) / np.gradient(x) / q


##make some plots
plt.figure(1)
plt.plot(x*1e6,phi/q)
plt.plot(x*1e6,phi/q-Eg/q)
plt.plot(x*1e6,Ef/q)
plt.xlabel( r'$x\,(\mathrm{\mu_m})$' )
plt.ylabel( r'$E\,(\mathrm{eV})$' )


plt.figure(2)
plt.plot(x*1e6,rho/q*1e-6)
plt.xlabel( r'$x\,(\mathrm{\mu_m})$' )
plt.ylabel( r'$\rho\,/q\,(\mathrm{cm^{-3}})$' )


##show the plots
plt.show()
```

REFERENCES CITED

[1] J. Nelson, *The Physics of Solar Cells*, vol. 1. London, UK: Imperial College Press, 2003.

[2] D. M. Chapin, C. S. Fuller, and G. L. Pearson, "A new silicon p-n junction photocell for converting solar radiation into electrical power," *J. Appl. Phys.*, vol. 25, no. 5, pp. 676–677, 1954.

[3] "Fraunhofer ise: Photovoltaics report, updated: 20 october 2015," 2015. https://www.ise.fraunhofer.de/en/downloads-englisch/pdf-files-englisch/photovoltaics-report-slides.pdf.

[4] B. E. McCandless and J. R. Sites, "Cadmium telluride solar cells," in *Handbook of Photovoltaic Science and Engineering* (A. Luque and S. Hegedus, eds.), pp. 600–641, New York: Wiley, 2nd ed., 2011.

[5] R. S. Muller and R. Zuleeg, "Vapor-deposited, thin-film heterojunction diodes," *J. Appl. Phys.*, vol. 35, no. 5, pp. 1550–1556, 1964.

[6] R. Dutton and R. Muller, "Thin film CdS-CdTe heterojunction diodes," *Solid State Electron.*, vol. 11, no. 8, pp. 749 – 756, 1968.

[7] E. I. Adirovich, Y. M. Yuabov, and G. R. Yagudaev, "Investigation of n-CdS/p-CdTe thin film heterojunctions," *Phys. Status Solidi A*, vol. 6, no. 1, pp. 311–322, 1971.

[8] D. Bonnet and H. Rabenhorst, "New results on the development of a thin-film p-CdTe-n-CdS heterojunction solar cell," in *Photovoltaic Specialists Conference, 9th, Silver Spring, Md*, pp. 129–132, 1972.

[9] A. L. Fahrenbruch, V. Vasilchenko, F. Buch, K. Mitchell, and R. H. Bube, "II-VI photovoltaic heterojunctions for solar energy conversion," *Appl. Phys. Lett.*, vol. 25, no. 10, pp. 605–608, 1974.

[10] K. Yamaguchi, N. Nakayama, H. Matsumoto, Y. Hioki, and S. Ikegami, "Photovoltaic effect in CdS-CdTe junctions," *Jpn. J. Appl. Phys.*, vol. 14, no. 9, p. 1397, 1975.

[11] J. Britt and C. Ferekides, "Thinfilm CdS/CdTe solar cell with 15.8% efficiency," *Appl. Phys. Lett.*, vol. 62, no. 22, pp. 2851–2852, 1993.

[12] "First solar achieves efficiency, durability milestones [press release]," 2015. Retrieved from http://investor.firstsolar.com/releasedetail.cfm?ReleaseID=895118.

[13] "First solar achieves world record 18.6 efficiency [press release]," 2015. Retrieved from http://investor.firstsolar.com/releasedetail.cfm?ReleaseID=917926.

[14] T. Gessert, S.-H. Wei, J. Ma, D. Albin, R. Dhere, J. Duenow, D. Kuciauskas, A. Kanevce, T. Barnes, J. Burst, W. Rance, M. Reese, and H. Moutinho, "Research strategies toward improving thin-film CdTe photovoltaic devices beyond 20% conversion efficiency," *Sol. Energ. Mat. Sol. C.*, vol. 119, pp. 149 – 155, 2013.

[15] A. Romeo, M. Terheggen, D. Abou-Ras, D. L. Btzner, F.-J. Haug, M. Klin, D. Rudmann, and A. N. Tiwari, "Development of thin-film Cu(In,Ga)Se2 and CdTe solar cells," *Prog. Photovoltaics Res. Appl.*, vol. 12, no. 2-3, pp. 93–111, 2004.

[16] H. B. Michaelson, "The work function of the elements and its periodicity," *J. Appl. Phys.*, vol. 48, no. 11, pp. 4729–4733, 1977.

[17] J. Li, J. Beach, and C. Wolden, "Rapid thermal processing of ZnTe:Cu contacted CdTe solar cells," in *Photovoltaic Specialist Conference (PVSC), 2014 IEEE 40th*, pp. 2360–2365, 2014.

[18] A. Mondal, B. E. McCandless, and R. W. Birkmire, "Electrochemical deposition of thin ZnTe films as a contact for CdTe solar cells," *Sol. Energ. Mat. Sol. C.*, vol. 26, no. 3, pp. 181 – 187, 1992.

[19] T. A. Gessert, A. R. Mason, P. Sheldon, A. B. Swartzlander, D. Niles, and T. J. Coutts, "Development of Cudoped ZnTe as a backcontact interface layer for thinfilm CdS/CdTe solar cells," *J. Vac. Sci. Technol. A*, vol. 14, no. 3, pp. 806–812, 1996.

[20] N. Romeo, A. Bosio, R. Tedeschi, A. Romeo, and V. Canevari, "A highly efficient and stable CdTe/CdS thin film solar cell," *Sol. Energ. Mat. Sol. C.*, vol. 58, no. 2, pp. 209 – 218, 1999.

[21] M. A. Green, "Improved estimates for te and se availability from Cu anode slimes and recent price trends," *Pro. Photovoltaics Res. Appl.*, vol. 14, no. 8, pp. 743–751, 2006.

[22] X. Wu, J. Zhou, A. Duda, Y. Yan, G. Teeter, S. Asher, W. Metzger, S. Demtsu, S.-H. Wei, and R. Noufi, "Phase control of CuxTe film and its effects on CdS/CdTe solar cell," *Thin Solid Films*, vol. 515, no. 15, pp. 5798 – 5803, 2007.

[23] S. Demtsu, D. Albin, J. Sites, W. Metzger, and A. Duda, "Cu-related recombination in CdS/CdTe solar cells," *Thin Solid Films*, vol. 516, no. 8, pp. 2251 – 2254, 2008.

[24] T. Gessert, W. Metzger, P. Dippo, S. Asher, R. Dhere, and M. Young, "Dependence of carrier lifetime on Cu-contacting temperature and ZnTe:Cu thickness in CdS/CdTe thin film solar cells," *Thin Solid Films*, vol. 517, no. 7, pp. 2370 – 2373, 2009.

[25] A. Castaldini, A. Cavallini, B. Fraboni, P. Fernandez, and J. Piqueras, "Deep energy levels in CdTe and CdZnTe," *J. Appl. Phys.*, vol. 83, no. 4, p. 2121, 1998.

[26] A. Balcioglu, R. K. Ahrenkiel, and F. Hasoon, "Deep-level impurities in CdTe/CdS thin-film solar cells," *J. Appl. Phys.*, vol. 88, no. 12, p. 7175, 2000.

[27] X. Mathew, "Photo-induced current transient spectroscopic study of the traps in CdTe," *Sol. Energ. Mat. Sol. C.*, vol. 76, no. 3, p. 225, 2003.

[28] J. Li, J. Duenow, D. Kuciauskas, A. Kanevce, R. Dhere, M. Young, and D. Levi, "Electrical characterization of Cu composition effects in CdS/CdTe thin-film solar cells with a ZnTe:Cu back contact," *IEEE J. Photovolt.*, vol. 3, no. 3, pp. 1095–1099, 2013.

[29] S. M. Sze, *Semiconductors Devices, Physics and Technology*. New York: Wiley, 2nd ed., 1985.

[30] J. D. Cohen and A. V. Gelatos, "Transient photocapacitance studies of deep defect transitions in hydrogenated amorphous silicon," in *Amorphous Silicon and Related Materials* (H. Fritzsche, ed.), pp. 475–512, Singapore: World Scientific, 1988.

[31] J. D. Cohen and D. V. Lang, "Calculation of the dynamic response of Schottky barriers with a continuous distribution of gap states," *Phys. Rev. B*, vol. 25, pp. 5321 – 5350, 1982.

[32] P. Blood and J. Orton, *The electrical characterization of semiconductors: majority carriers and electron states*. Techniques of physics, Academic Press, 1992.

[33] D. V. Lang, "Space-charge spectroscopy in semiconductors," in *Thermally Stimulated Relaxation in Solids* (P. Bräunlich, ed.), pp. 93–132, Berlin, Germany: Springer, 1979.

[34] A. V. Gelatos, J. D. Cohen, and J. P. Harbison, "Correlation of optical and thermal emission processes for boundtofree transitions from mobility gap states in doped hydrogenated amorphous silicon," *AIP Conference Proceedings*, vol. 120, no. 1, pp. 16–23, 1984.

[35] A. V. Gelatos, J. D. Cohen, and J. P. Harbison, "Assessment of lattice relaxation effects in transitions from mobility gap states in hydrogenated amorphous silicon using transient photocapacitance techniques," *Appl. Phys. Lett.*, vol. 49, no. 12, pp. 722–724, 1986.

[36] C. E. Michelson, A. V. Gelatos, J. D. Cohen, and J. P. Harbison, "Observtion of an oxygen-related mobility-gap defect in ion-implanted hydrogenated amorphous silicon films," *Phys. Rev. B*, vol. 35, pp. 4141–4144, Mar 1987.

[37] A. V. Gelatos, K. K. Mahavadi, J. D. Cohen, and J. P. Harbison, "Transient photocapacitance and photocurrent studies of undoped hydrogenated amorphous silicon," *Appl. Phys. Lett.*, vol. 53, no. 5, pp. 403–405, 1988.

[38] T. M. Leen and J. D. Cohen, "Observation of configuration switching of the D center in a-Si:H," *J. Non-Cryst. Solids*, vol. 137-138, Part 1, pp. 319 – 322, 1991. Proceedings of the Fourteenth International Conference on Amorphous Semiconductors-Science and Technology.

[39] J. D. Cohen, T. Unold, A. V. Gelatos, and C. M. Fortmann, "Deep defect structure and carrier dynamics in amorphous silicon and silicon-germanium alloys determined by transient photocapacitance methods," *J. Non-Cryst. Solids*, vol. 141, pp. 142 – 154, 1992.

[40] T. Unold, J. D. Cohen, and C. M. Fortmann, "Electronic mobility gap structure and deep defects in amorphous silicongermanium alloys," *Appl. Phys. Lett.*, vol. 64, no. 13, pp. 1714–1716, 1994.

[41] T. Unold, J. Hautala, and J. D. Cohen, "Effect of carbon impurities on the density of states and the stability of hydrogenated amorphous silicon," *Phys. Rev. B*, vol. 50, pp. 16985–16994, Dec 1994.

[42] S. Guha, J. Yang, D. L. Williamson, Y. Lubianiker, J. D. Cohen, and A. H. Mahan, "Structural, defect, and device behavior of hydrogenated amorphous Si near and above the onset of microcrystallinity," *Appl. Phys. Lett.*, vol. 74, no. 13, pp. 1860–1862, 1999.

[43] Y. Lubianiker, J. D. Cohen, H.-C. Jin, and J. R. Abelson, "Effect of embedded microcrystallites on the light-induced degradation of hydrogenated amorphous silicon," *Phys. Rev. B*, vol. 60, pp. 4434–4437, Aug 1999.

[44] Y. Lubianiker, Y. Tan, J. Cohen, and G. Ganguly, "Amorphous silicon deposited at high growth rates near the onset of microcrystallinity," *J. Non-Cryst. Solids*, vol. 266-269, Part 1, pp. 450 – 454, 2000.

[45] N. M. Johnson and D. K. Biegelsen, "Identification of deep-gap states in a-Si:H by photo- depopulation-induced electron-spin resonance," *Phys. Rev. B*, vol. 31, pp. 4066–4069, Mar 1985.

114

[46] P. Wickboldt, D. Pang, W. Paul, J. H. Chen, F. Zhong, C.-C. Chen, J. D. Cohen, and D. L. Williamson, "High performance glow discharge a-Si1xGex:H of large x," *J. Appl. Phys.*, vol. 81, no. 9, pp. 6252–6267, 1997.

[47] C.-C. Chen, F. Zhong, J. D. Cohen, J. C. Yang, and S. Guha, "Evidence for charged defects in intrinsic glow-discharge hydrogenated amorphous-silicon–germanium alloys," *Phys. Rev. B*, vol. 57, pp. R4210–R4213, Feb 1998.

[48] J. D. Cohen, "Light-induced defects in hydrogenated amorphous silicon germanium alloys," *Sol. Energ. Mat. Sol. C.*, vol. 78, no. 1-4, pp. 399 – 424, 2003.

[49] S. Datta, Y. Xu, A. Mahan, H. M. Branz, and J. D. Cohen, "Superior structural and electronic properties for amorphous silicon-germanium alloys deposited by a low temperature hot wire chemical vapor deposition process," *J. Non-Cryst. Solids*, vol. 352, no. 9-20, pp. 1250 – 1254, 2006.

[50] J. T. Heath, J. D. Cohen, W. N. Shafarman, D. X. Liao, and A. A. Rockett, "Effect of Ga content on defect states in CuIn1-xGaxSe2 photovoltaic devices," *Appl. Phys. Lett.*, vol. 80, no. 24, pp. 4540–4542, 2002.

[51] J. D. Cohen, J. T. Heath, and W. N. Shafarman, "Photocapacitance spectroscopy in copper indium diselenide alloys," in *Wide-Gap Chalcopyrites* (S. Siebentritt and U. Rau, eds.), pp. 69–87, Berlin, Germany: Springer, 2006.

[52] P. T. Erslev, J. W. Lee, W. N. Shafarman, and J. D. Cohen, "The influence of Na on metastable defect kinetics in CIGS materials," *Thin Solid Films*, vol. 517, no. 7, pp. 2277 – 2281, 2009.

[53] P. T. Erslev, J. Lee, G. M. Hanket, W. N. Shafarman, and J. D. Cohen, "The electronic structure of Cu(In1-xGax)Se2 alloyed with silver," *Thin Solid Films*, vol. 519, no. 21, pp. 7296 – 7299, 2011. Proceedings of the EMRS 2010 Spring Meeting Symposium M: Thin Film Chalcogenide Photovoltaic Materials.

[54] P. T. Erslev, H. Q. Chiang, D. Hong, J. F. Wager, and J. D. Cohen, "Electronic properties of amorphous zinc tin oxide films by junction capacitance methods," *J. Non-Cryst. Solids*, vol. 354, no. 19-25, pp. 2801 – 2804, 2008.

[55] A. F. Halverson, J. J. Gutierrez, J. D. Cohen, B. Yan, J. Yang, and S. Guha, "Electronic characterization and effects of light-induced degradation on hydrogenated nanocrystalline silicon," *Appl. Phys. Lett.*, vol. 88, no. 7, p. 071920, 2006.

[56] P. Hugger, J. Cohen, B. Yan, J. Yang, and S. Guha, "Properties of light-induced degradation and the electronic properties of nanocrystalline silicon solar cells grown under functionally graded hydrogen dilutions," *J. Non-Cryst. Solids*, vol. 354, no. 19-25, pp. 2460 – 2463, 2008.

[57] D. W. Miller, C. W. Warren, O. Gunawan, T. Gokmen, D. B. Mitzi, and J. D. Cohen, "Electronically active defects in the Cu2ZnSn(Se,S)4 alloys as revealed by transient photocapacitance spectroscopy," *Appl. Phys. Lett.*, vol. 101, no. 14, p. 142106, 2012.

[58] J. Boucher, D. Miller, C. Warren, J. Cohen, B. McCandless, J. Heath, M. Lonergan, and S. Boettcher, "Optical response of deep defects as revealed by transient photocapacitance and photocurrent spectroscopy in CdTe/CdS solar cells," *Sol. Energ. Mat. Sol. C.*, vol. 129, pp. 57 – 63, 2014.

[59] C. W. Warren, J. Li, C. A. Wolden, D. M. Meysing, T. M. Barnes, D. W. Miller, J. T. Heath, and M. C. Lonergan, "The effect of copper on the sub-bandgap density of states of CdTe solar cells," *Appl. Phys. Lett.*, vol. 106, no. 20, p. 203903, 2015.

[60] W. B. Jackson, S. M. Kelso, C. C. Tsai, J. W. Allen, and S.-J. Oh, "Energy dependence of the optical matrix element in hydrogenated amorphous and crystalline silicon," *Phys. Rev. B*, vol. 31, pp. 5187–5198, Apr 1985.

[61] J. Chelikowsky, D. J. Chadi, and M. L. Cohen, "Calculated valence-band densities of states and photoemission spectra of diamond and zinc-blende semiconductors," *Phys. Rev. B*, vol. 8, pp. 2786–2794, Sep 1973.

[62] G. D. Cody, T. Tiedje, B. Abeles, B. Brooks, and Y. Goldstein, "Disorder and the optical-absorption edge of hydrogenated amorphous silicon," *Phys. Rev. Lett.*, vol. 47, pp. 1480–1483, Nov 1981.

[63] F. Urbach, "The long-wavelength edge of photographic sensitivity and of the electronic absorption of solids," *Phys. Rev.*, vol. 92, pp. 1324–1324, Dec 1953.

[64] J. C. Vickerman and A. J. Swift, "Secondary ion mass spectrometry—the surafce mass spectrometry," in *Surface Analysis—The Principal Techniques* (J. C. Vickerman, ed.), pp. 135–214, New York: Wiley, 1997.

[65] D. M. Meysing, C. A. Wolden, M. M. Griffith, H. Mahabaduge, J. Pankow, M. O. Reese, J. M. Burst, W. L. Rance, and T. M. Barnes, "Properties of reactively sputtered oxygenated cadmium sulfide (CdS:O) and their impact on CdTe solar cell performance," *J. Vac. Sci. Technol. A*, vol. 33, no. 2, p. 021203, 2015.

[66] J. Li, D. R. Diercks, T. R. Ohno, C. W. Warren, M. C. Lonergan, J. D. Beach, and C. A. Wolden, "Controlled activation of ZnTe:Cu contacted CdTe solar cells using rapid thermal processing," *Sol. Energ. Mat. Sol. C.*, vol. 133, no. 0, pp. 208 – 215, 2015.

[67] J. Ma, D. Kuciauskas, D. Albin, R. Bhattacharya, M. Reese, T. Barnes, J. V. Li, T. Gessert, and S.-H. Wei, "Dependence of the minority-carrier lifetime on the stoichiometry of CdTe using time-resolved photoluminescence and first-principles calculations," *Phys. Rev. Lett.*, vol. 111, p. 067402, 2013.

[68] I. Strzalkowski, S. Joshi, and C. R. Crowell, "Dielectric constant and its temperature dependence for GaAs, CdTe, and ZnSe," *Appl. Phys. Lett.*, vol. 28, no. 6, pp. 350–352, 1976.

[69] S. H. Demtsu, *Impact of Back-Contact Materials on Performance and Stability of CdS/CdTe Solar Cells*. PhD thesis, Colorado State Univ., Fort Collins, CO, 2006.

[70] A. Morales-Acevedo, "Thin film CdS/CdTe solar cells: Research perspectives," *Sol. Energy*, vol. 80, no. 6, pp. 675 – 681, 2006.

[71] K. D. Dobson, I. Visoly-Fisher, G. Hodes, and D. Cahen, "Stability of CdTe/CdS thin-film solar cells," *Sol. Energ. Mat. Sol. C.*, vol. 62, no. 3, pp. 295 – 325, 2000.

[72] D. Grecu and A. D. Compaan, "Photoluminescence study of Cu diffusion and electromigration in CdTe," *Appl. Phys. Lett.*, vol. 75, no. 3, pp. 361–363, 1999.

[73] A. Einstein, "Über die von der molekularkinetischen theorie der wärme geforderte bewegung von in ruhenden flüssigkeiten suspendierten teilchen," *Annalen der Physik*, vol. 322, no. 8, pp. 549–560, 1905.

[74] W. H. Press, S. A. Teukolsky, W. T. Vetterling, and B. P. Flannery, *Numerical Recipes: The Art of Scientific Computing*. New York: Cambridge University Press, 3rd ed., 2007.